



UIT

**THE ARCTIC
UNIVERSITY
OF NORWAY**

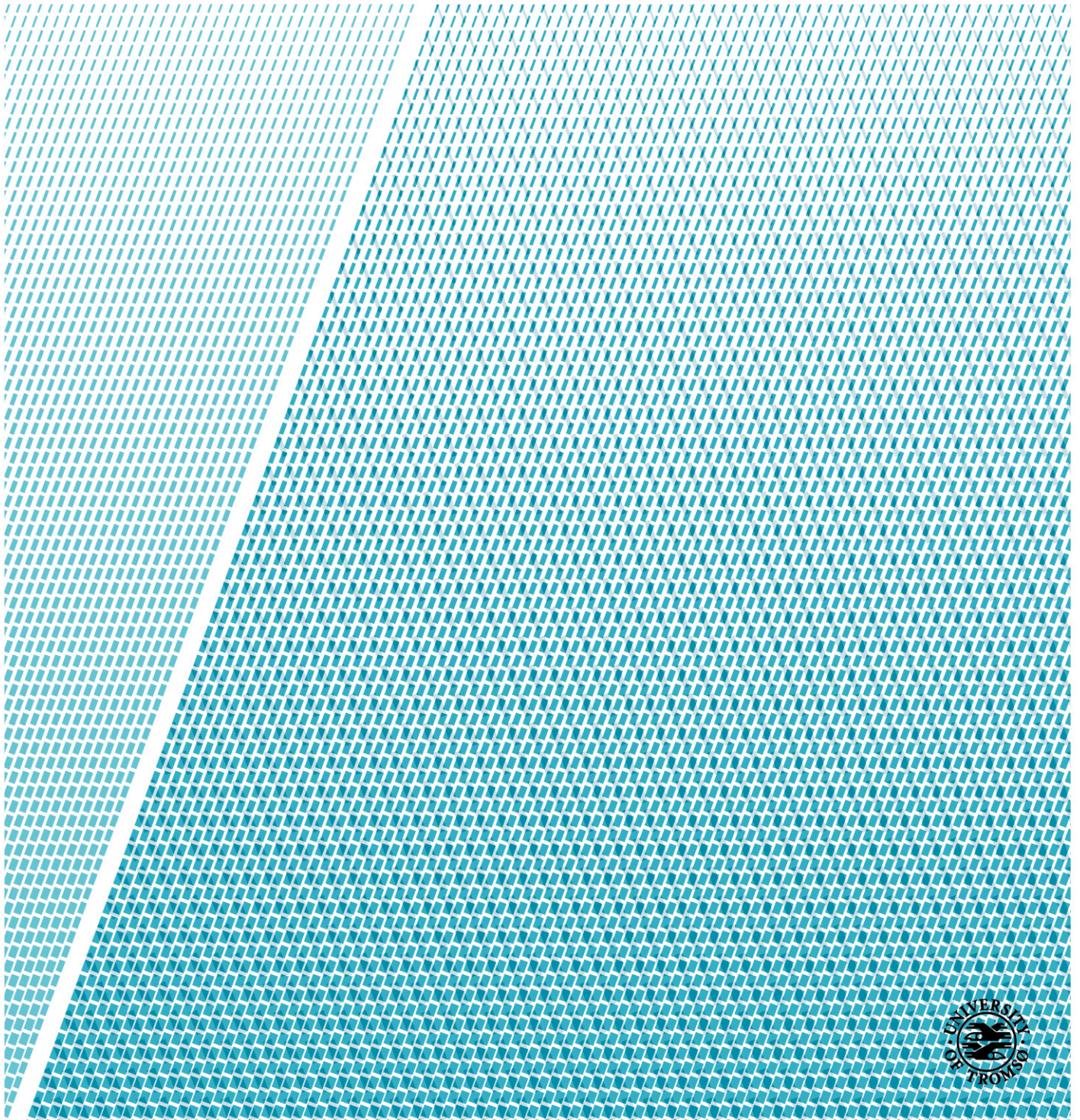
Faculty of Science and Technology

Department of Geology

Rockfall hazard assessment based on semi-automatic point cloud analysis from UAV data

Karin Bergbjørn

Master's thesis in geology GEO-3900 - December 2018



Abstract

Slettind in Flaktstad municipality, Lofoten in Nordland, has numerous rockfalls throughout the year, hitting Fv 805 on a weekly basis, and is estimated the most dangerous road in Nordland county. A rock avalanche hit the road winter 2017 closing it for 2 weeks, and isolating the small village Myrland. Statens Vegvesen consider to build a tunnel to protect the road but the failure mechanisms has been little understood, as it is deemed too dangerous for traditional fieldwork to access the mountain in a safe manner. Traditional fieldwork involves shear strength testing of joint sets and infill, as well as mapping of joint orientations, roughness, and volumes of blocks, using Barthons Q method, Rock Mass Index or GSI. However as it has not been feasible to attend the wall for such mapping, due to the steepness, height and risk for rockfall, new techniques for rockfall hazard assessment have been put in use.

The purpose of this master thesis has been to use photogrammetry from UAV images, and Structure-for-Motion to create a 3D model and identify joint surfaces, orientations and evaluate the failure mechanisms. The workflow has been compared and evaluated against traditional mapping methods. Photogrammetry from drone images has proven valuable for understanding the structures and driving forces in a rock mass, and is a more flexible and cheaper option than LiDAR or similar, to build point clouds. As such, a validated semi-automated workflow is a resource for evaluating steep, inaccessible mountainsides.

Acknowledgements

This year have been a roller coaster in so many ways.

It has been an honour to work with my supervisors Anne Hormes, Louise M. Vick and Hallvard Nordbrøden Haugen (SVV). You guys rock!

Steffen Bergh, Rolf Andersen and Johan Eilertsen Arntzen have given invaluable assistance when needed the most and intervened on short notices. This wouldn't have been possible without you...

Thank you to all of my friends encouraging and lifting my spirits. Thank you Tore & Rigmor for coffee, cookies and good moods, and my family for enduring all the bad days...

To Tore. For everything.

Karin Bergbjørn – Desember 2018, Skjomen

Table of Contents

Abstract.....	II
Acknowledgements.....	IV
1 Introduction.....	1
1.1 Background.....	1
1.2 Aim and objectives	2
1.3 Acronyms.....	2
1.4 Project background	3
1.5 Previous work	5
2 Rock failure.....	6
2.1 Rockfall classification.....	6
2.2 Triggering factors.....	7
2.3 Conditional factors.....	8
2.4 Shear strength.....	11
3 Study area.....	13
3.1 Regional geology	13
3.1.1 Bedrocks and structures at Slettind.....	16
3.2 Quaternary Geology of western Lofoten	17
3.3 Climate setting	20
3.4 Geographic location and topography	23
3.5 Historical events and mitigation measures	25
4 Methods.....	32
4.1 Field work and data acquisition	32
4.2 Rock mass classification with GSI	33
4.3 Rock mass classification with Q system.....	34
4.4 GIS -Software and visualization	37
4.5 UAV surveys.....	38
4.5.1 Flightplan	40

4.5.2	Structure-from-Motion processing.....	42
4.5.3	Agisoft workflow	43
4.6	Dips, structural and kinematic analysis	46
4.7	Semi-automated structural analysis with Coltop3D	47
4.8	Identification of potential rockfall areas	49
5	Results.....	50
5.1	Introduction.....	50
5.2	Geomorphology	51
5.2.1	Field observations	51
5.3	Bedrock.....	54
5.3.1	Lithology observations.....	54
5.3.2	Tectonic lineaments at Slettind.....	56
5.3.3	Structural observations from the field.....	59
5.4	Location 1a.....	61
5.4.1	Rock mass quality	61
5.4.2	Q values and GSI	63
5.5	Location 1.b	65
5.5.1	Rock mass quality	65
5.5.2	Q values and GSI	66
5.5.3	Structural orientation data 1.a and 1. b	67
5.6	Location 2	69
5.6.1	Rock mass quality	69
5.6.2	Q values and GSI	70
5.6.3	Structural orientation data.....	72
5.7	Location 3	74
5.7.1	Bedrock descriptions.....	75
5.7.2	Q value and GSI.....	76
5.7.3	Structural orientation data.....	79

5.8	Location 4	80
5.8.1	Bedrock descriptions.....	80
5.8.2	Q values and GSI	81
5.8.3	Structural orientation data.....	82
5.9	Structural observations from Coltop3D	84
5.10	Overview of Slettind joint sets.....	90
6	Kinematic analysis	92
6.1	Kinematics failure analysis	92
6.2	Coltop3D critical joint sets	96
7	Discussion.....	99
7.1	Conditioning factors for rock slope failure at Slettind.....	99
7.2	Kinematic analysis and triggering factors.....	106
7.3	UAV derived SfM models	110
7.4	Applications and future tasks.....	113
8	Conclusion	115
	Works cited.....	118
	Appendix 1: Weather graphs	125
	Appendix 2: Structural measurements with different methods.....	127
	Appendix 3: Agisoft report	129

1 Introduction

1.1 Background

The topography of Norway consists of high mountains meeting the coast and the fjords along the entire length of the country. Historically roads have been built where there is passage, without leaving much room for risk evaluation. The consequences are rockfall/rock avalanches reaching the infrastructure and threatening humans that travel along the roads. In 2017 there were registered 1 884 rock avalanches from mountains or higher rock walls reaching infrastructure (NVE, 2018) and the increasing amount of traffic on roads augments the risk. One of the rock avalanches in 2017 hit Fv 805 Myrlandsvegen, closing the road for two weeks and isolating the settlement of Myrland. At Fv 805 there are weekly incidents with rockfall reaching the road through-out the year, and occasional larger events, but there is no safety mitigation in place and the failure mechanism is not understood.

When the source for rockfalls or avalanches are high on a rock wall both investigation and mitigation become difficult. The rock is often not attainable for field work and the failure mechanisms can't be properly evaluated. Lately photogrammetry has been used to build 3D models and point clouds that can be analyzed in respect of rock structures and kinematics to find failure mechanisms (Böhme et al., 2013; Derron et al., 2013; Jaboyedoff et al., 2007). Unmanned Aerial Vehicle (UAV) are cheap, fast and an excellent tool for producing photogrammetry and lately these have been used in rock failure research (Danzi et al., 2013; Giordan et al., 2015; Manousakis et al., 2016). At Fv 805 the only way to examine the rock structure is from the air, and this is often the case for Statens Vegvesen both at Myrlandsvegen and other hazardous locations.

1.2 Aim and objectives

The objective of this thesis is to determine the failure mechanism of rockfalls from Slettind and analyze the release area in regards of potentially unstable rock. It is also of importance to validate the use of UAV for the purpose of rock failure susceptibility mapping. This will be done by the following steps:

- Manual structural orientation data
- Bedrock evaluation (GSI and Q-value)
- Flights with Unmanned Aerial Vehicle (UAV)
- Building point clouds and 3D models (SfM)
- Kinematic analyses
- Structural analysis in Coltop3D

The use of UAV and semi-automatic kinematic analysis needs to be validated against traditional manual structural fieldwork in stereonet and a workflow needs to be established.

1.3 Acronyms

2D	Two dimensional
3D	Three dimensional
DEM	Digital Elevation Model
DGPS	Differential GPS
DTM	Digital Terrain Model
GCP	Ground Control Point
GIS	Geographical Information System
GSI	Geological Strength Index
GPS	Geographical Position System
GPU	Graphics Processing Unit

GSR	Ground Sampling Resolution
HSI	Hue Saturation Index
JCS	Joint Compression Strength
JRC	Joint roughness coefficient
LiDAR	Light detection and ranging
LGM	Last Glacial Maximum
NVE	Norwegian water resources and energy directorate
RAM	Random Access Memory
RQD	Rock quality designation
RTK	Real time kinematic
SfM	Structure from Motion
SVV	Norwegian Public Road Administration
NGI	Norwegian geotechnical institute
NGU	Norwegian geological survey
TLS	Terrestrial Laser Scan
UAS	Unmanned Aerial System
UAV	Unmanned Aerial Vehicle
ÅDT	Mean daily traffic on road through a year

1.4 Project background

Fv 805 is a 5.5 km long gravel road leading to the settlement of Myrland in Lofoten (Fig. 12). Statens Vegvesen Region Nord (2015) identified the road Fv 805 (Myrlandsvegen) below Slettinden, as the most dangerous road in Nordland county with the highest risk of rockfall and snow avalanche. The cost to protecting the road is estimated at 440 million NOK, which would make it the most expensive project of its kind in the country, should it go ahead.

In 2017 a rock avalanche closed the road for two weeks (Aronsen, 2017), and the 15 residents were isolated. Approximately 1.8 km are subjected to numerous rockfalls, rock avalanches, icefalls, snow avalanches, debris flows or earth slides from the east-facing slope, making it a threat year-round and in almost any weather condition.

Statens Vegvesen (SVV) is the department responsible in Norway for the statistics, surveillance, hazard evaluation and protection of the roads that are threatened by geohazards. They are responsible for all roads at county and national level. The mitigation measures adopted depend on annual traffic numbers and the magnitude of hazard that road users are exposed to. Fv 805 is the most hazardous rockfall-exposed road in the area that continues to lack both protection and understanding of the mechanisms active at the site (SVV, 2015). As early as 1984 a tunnel bypassing the hazardous stretch of road was discussed (Lied, 1984) and again by Aronsen (2001). Manual structural measurements are difficult at the site as there are no available outcrops in the inaccessible release area. It is considered too dangerous to do extended fieldwork on the slope or anywhere within the run-out zone. Aronsen (2017) has concluded that the only way to evaluate the rock face is by remote sensing with UAV.

Modern research has developed the technology of photogrammetry and SfM producing point clouds and 3D models that can be created based on high quality images attained with Unmanned Aerial System (UAS). UAS technology has the benefit of being able to take images from different heights, angles and at a safe distance from hazardous zones. A complex and vertical, or overhanging rock face will not show the shortcomings from a fixed laserscan if filmed from different angles and is a cheaper and often more effective way of capturing images than from a helicopter.

A developed workflow that displays the process of mapping and evaluating a large rockface, building 3D models, needs to be established and tested using UAS. Further, this work will be compared to traditional and semi-automated mapping methods.

This thesis aims to provide data and an interpretation that can be used by Statens Vegvesen in their planning procedures for mitigation at the site. The workflow used is also intended to be a resource for Statens Vegvesen and for similar geohazard sites. Working with this type of semi-automated analysis for rock slope failures would reduce the amount of manual structural analyzes necessary (time/cost/security) and opens for precise and accurate modelling of hazardous locations and/or non-accessible rock sites in a cheaper and more convenient way (Ferrero et al., 2009).

1.5 Previous work

Multiple studies of unstable rock slopes in both Troms and Nordland have been completed in recent years (Braathen et al., 2004; Hermanns et al., 2013), and multiple theses have been written on the subject (Bredal, 2016; Grumstad, 2017; Haukenes, 2018, Skrede, 2013) Many of these focus on creeping-type landslides and LiDAR or terrestrial scanning methods have been used but these are expensive and mostly suitable for either overview, or mapping of unstable rockslopes. However rapid mass movements such as rockfalls, rock avalanches and snow avalanches are of more relevance to road safety. Rockfalls are difficult to predict due to the complexity of triggering factors, and identification of potential release areas and run-out zones is therefore of great interest. Detailed studies on rockfall-prone areas have been based on manual kinematic analyses, laserscan derived Digital Elevation Maps (DEM), aspect maps, slope inclination maps and point clouds for analyzing discontinuities, and potential failure planes (Hermanns et al., 2013; Jaboyedoff et al., 2012; Oppikofer et al., 2009). Throughout Norway NVE has published contract reports concerning rock fall hazard zones on their website (www.skrednett.no).

The last couple of years studies comparing UAV with TLS og LiDAR derived results have started to appear with regards to rockfall and landslide hazard management (Danzi et al., 2013, Manousakis et al., 2016, Giordan et al., 2015), where some studies compare results, but only few have used UAV for more accurate results, especially when dealing with overhanging rockwalls (Hellman, 2018).

2 Rock failure

2.1 Rockfall classification

A failing rock mass is classified in Norway as either rockfall ("steinsprang"), rock avalanche ("steinskred") or mountain avalanche ("fjellskred") based on the total mass volume and type of movement; below 100 m^3 it is defined as a rockfall where singularly blocks detach and fall independently. When the volume augments to $100\text{-}10\,000 \text{ m}^3$ it is defined as rock avalanche and the blocks move more like a flowing continuous mass where the interaction between blocks gives a longer run-out distance. Mountain avalanche is a third Norwegian term used when the volume exceeds $10\,000 \text{ m}^3$, with extreme run-out distances (Devoli et al., 2011) and might be translated to the English terminology of rock avalanche (Hungre et al., 2014). Large individual blocks may easily exceed 100 m^3 without the blockinteraction associated with rock avalanches, (Blikra et al., 2006)has therefore augmented the volumes connected to the definitions.

Internationally the classification differentiates between rockfall/slide/avalanche based on type of movement and material involved, not on volume. Hungre et al., (2014) updated Varnes (1978) classification of mass movement and uses terms like rockfall, rockslide, rock avalanche and rock slope deformation. Since SVV, NGI and NVE uses the Norwegian terms, it has also been used in this thesis for simplification purposes in regard to statistics.

Detached from a steep source, often defined as the rock slope, a rock mass either falls in free air, bounces or rolls downwards with high translational or rotational velocity. The trajectory from the source is usually high-angle and the impact depends on the overall geometry of the transit zone, the size and shape of the block, rock type and impact angle. The transit zone can be split into colluvium slope: that has an angle steeper than the deposit and where rocks doesn't accumulate, and the talus slope: where blocks accumulate in a sorted fashion, fine material from 38° at the apex, and larger blocks at the toe from $10\text{-}20^\circ$ (Evans & Hungre, 1993).

Higher energy blocks that are larger and/or from higher ground reach the run-out zone and can be calculated by a line drawn at 27.5 from the base of the rock slope called rolling friction coefficient of rockfalls (Hungar, 1988). Soft soil in the trajectory zone gives more friction and absorbs the impact of a free-falling block. The block loses more of its kinetic energy and velocity, where the weight of the block also will be decisive. The velocity and therefore also the force at impact is directly dependent on the weight and rocktype of the block, as a hard rock type tends to stay more intact with less interaction between blocks, and a weaker rock type fractionates, interacts and spreads out (Agliardi & Crosta, 2003; Bozzolo & Pamini, 1986). With every interaction the bouncing rocks lose energy and the run-out distance is increasingly shorter. Low angle transit zone offers more friction at impact, and also shorter run-out zones (Guzzetti et al., 2002; Wyllie, 2014).

2.2 Triggering factors

Tectonic history at the source area along with erosion determines if and how failure is initialized and are crucial for strength properties (Braathen et al., 2004; Stead & Wolter, 2015). The number of tectonic deformation episodes and type of damage will in combination with rocktype, weathering, in situ stress and groundwater pressure induce the shear strength and restraining force. Fault zones will influence the groundwater flow and pore pressure, further augmenting the driving force by pressure as well as reducing friction. The sum of triggering and conditioning factors is seen in Fig. 1 (Volkwein et al., 2011) and the tectonic setting of the study site is described further in chapter 3.1.1.

If joints and/or foliation orientation is favorable for rock failure of a massive rock, water is one of the most important external factors, as it causes expansion of clay minerals in combination with erosion on planes and dissolving of minerals. Augmented pore pressure in joints also reduces the shear strength of the rock and friction (Braathen et al., 2004; Domaas & Grimstad 2014). Water is also involved in freeze/thaw events where water expands as a result of freezing. If cold weather persists in a stable manner ice may contribute to stability in

joints (Davies et al., 2001). Thermal stress is almost as important when it comes to large diurnal temperature changes, and studies has shown that rockfall then happens at the coldest time of the day (Dietze et al., 2017). Other triggering factors are seismic activity, human factors and chemical erosion. Other triggering factors are seismic activity, human factors and chemical erosion.

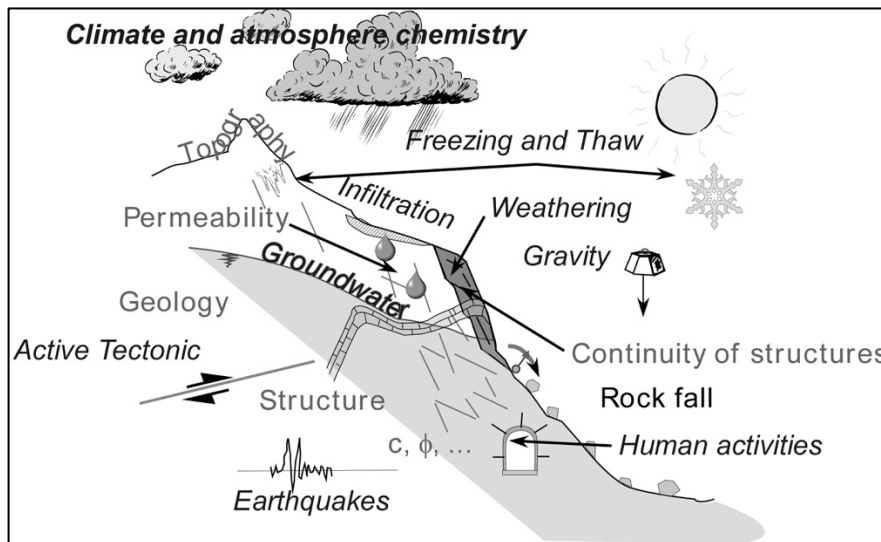


Fig. 1 Overview over conditional and triggering factors for rock failure. Retrieved from Volkwein et al. (2011)

Taking this into account and that the most important climate change factors the next 50 years is an increase in annual precipitation, more occurrent snow melting during cold season, and larger areas without snow which creates larger temperature fluctuations, it is expected to see the rate of rockfall to increase (Bjordal et al., 2011; Hanssen-Bauer et al., 2015).

2.3 Conditional factors

Source areas are often classified as slopes steeper than $> 40^\circ$ (NGU, 2015, (Jaboyedoff & Labiouse, 2003), but most rockfalls are associated with source areas $> 60-75^\circ$ where the bedrock and structures becomes less important (Braathen et al., 2004; Devoli et al., 2011; Lambert & Nicot, 2013; Schanche, 2014; Volkwein et al., 2011; Wyllie & Mah, 2004). In susceptibility maps in Norway all slopes are considered as potential source areas if they are

steeper than 40° , which is problematic as bedrock isn't considered. For a rock to slide on a plane of 40° a trigger is often necessary (Dorren, 2003).

Structural features that creates discontinuities in the rock mass will destabilize a block when the friction angle is exceeded leaving gravitational stress as the main driving force. Structures may be faults that show movement, folds, bedding, joints and/or foliation with cleavage that strongly affects friction and type of mechanics. The extent and distance between structures, surface of the planes and strength of bedrock will affect the shear strength and the size of blocks. Spacing of joints and the joint orientation is decisive for the size of block as heavily jointed rock will produce smaller blocks (Hoek & Brown, 1997; Wyllie & Mah, 2004).

Rockfalls in a specific area is often repetitive, and the same failure system often repeats itself at the same source. Rockfall is classified as either toppling, wedge failure or planar/sliding failure depending on geometry and discontinuities in the bedrock (Varnes, 1978). To identify and map what type of failures that is present it is common to use kinematic analysis in a stereographic projection, which will be further described in chapter 4.6. The interaction between slope angle and discontinuity is decisive for failure mechanism. If the discontinuity plane is within 20° from the slope angle a fall is possible (Høeg et al., 2014).

For planar failure the dip direction of the planar discontinuity must be within $\pm 20^\circ$ of the dip direction of slope and less than the dip of slope, such that it daylight. The dip of the sliding plane must be larger than the friction of the plane for failure to occur. Tension cracks in steep slopes is often present for a planar failure.

Wedge failure can occur when the lines of intersection of at least two sets of discontinuities are perpendicular to the strike of slope and dips and intersects towards the plane of slope, wedge failure can occur. At least one joint intersect must be greater than the friction angle of the joint surfaces. Wedge failure mechanism is otherwise similar to planar failure.

When the center of gravity falls outside of the base of a column of rock that is dispersed with steeply dipping discontinuities the block rotates over its own axis and falls. Toppling is often conditioned by the pressure from other blocks lying behind, or other external forces such as roots. Undercut bedrock made by excavations also causes toppling failures. Block toppling is different to flexural toppling as another set of fractures defines the height of blocks and undercuts them.

Direction and dip of discontinuities are important factors that determine type of failure mode, if they overcome the angle of friction. If dip and dip direction of a discontinuity, or line of intersection, is less than angle of slope, sliding is possible. If they dip into the slope at a high angle, toppling is possible (Fig. 2) (Wyllie and Mah, 2004).

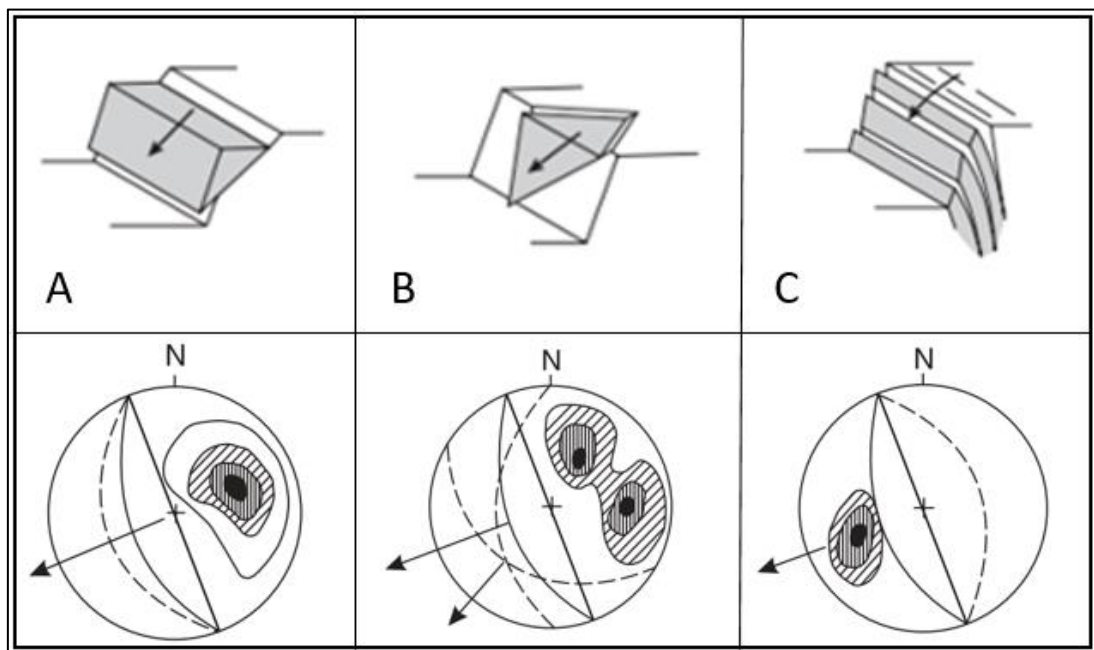


Fig. 2 Geometries of discontinuities causing planar (A), wedge (B) and toppling (C) failure and respective visualization in stereographic projection. Retrieved from Wyllie & Mah (2004).

2.4 Shear strength

The friction angle depends on the non-linear relationship between shear stress and normal stress and is high when normal stress is low across the joint (Fig. 3). The joint roughness from asperities in the bedrock will affect the friction angle reducing the shear strength of the joint as well as the above-mentioned factors that reduce the normal stress (Barton et al., 1974; Nilsen & Ozdemir, 1999).

Shear strength can be calculated as follows:

$$\tau = \sigma_n \tan(JRC \cdot \log \sigma_s) + \varphi_r$$

τ	Shear strength
σ_n	Normal stress
Φ_r	Residual friction angle
JRC	Joint roughness coefficient
JCS	Joint compression strength (from Schmidt hammer)

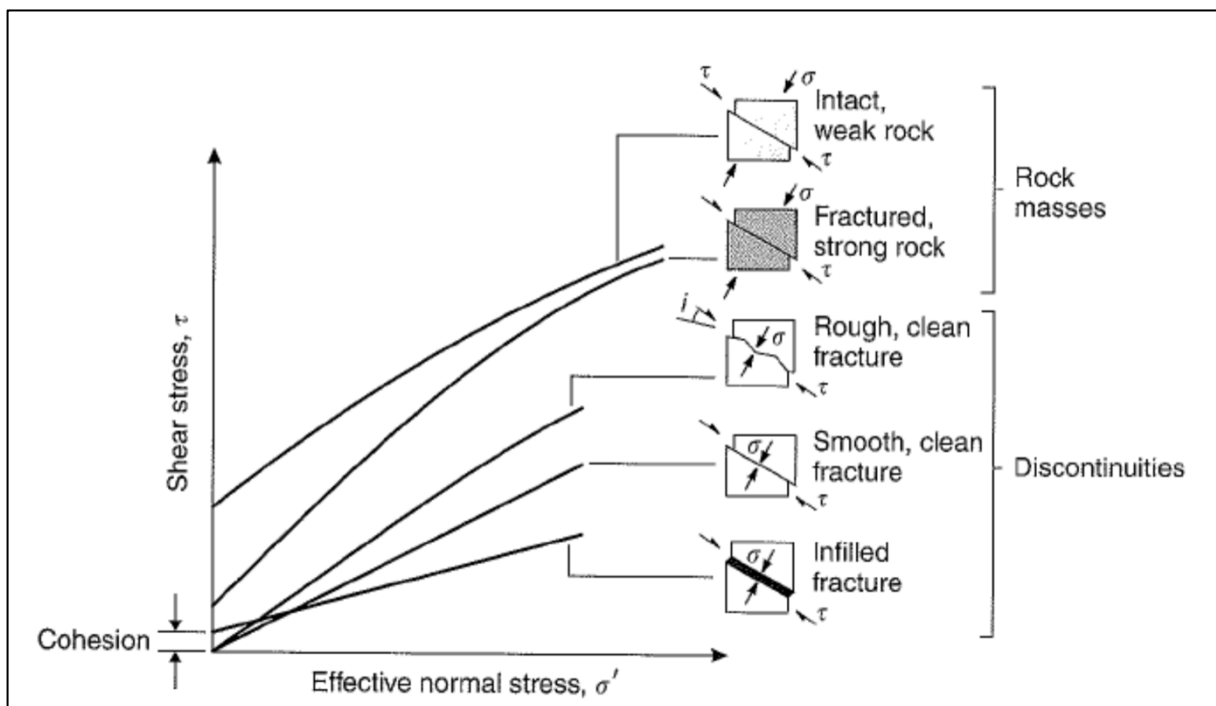


Fig.3 Relationship between shear stress and effective normal stress, and the difference between discontinuities and rock masses. Retrieved from Wyllie & Mah (2004).

Friction angle (joint roughness coefficient, JRC) can be determined by lab testing, in-situ testing, calculation or empirical methods (Q method, GSI, RMR). Many factors will affect the results and as they will vary across the location due to different angles in foliation, joint plane orientation, erosion, water, infill, earlier rock falls etc. Joint roughness in a fault as opposed to joints are very low due to the movement that have erased irregularities, requiring more shear stress for a block to slide. It is therefore common to adopt the friction angles set for common lithologies, resulting from vigorous lab-testing (Barton, 1974). Normally it is set to be the same as the residual friction angle and varies in gneiss between 27-34° (Wyllie & Mah, 2004).

3 Study area

3.1 Regional geology

The Lofoten-Vesterålen islands consist mostly of Neoproterozoic basement gneisses intruded by a suite of Palaeoproterozoic magmatic rocks (Fig. 4; Corfu, 2004; Griffin et al. 1978), and is considered to be a part of the Fennoscandian Shield (Bergh et al. 2014). The islands are bound by the moderate to high-grade West Troms Basement Complex in the northeast (Bergh et al. 2010). The bedrocks in Lofoten are only weakly affected by the Caledonian orogeny, except in the Leknes area where remnants of a Caledonian nappe have been down-faulted to the east (Griffin et al., 1978).

The Palaeoproterozoic magmatic rocks are composed of mostly homogenous and massive mangerites, charnockites, anorthosites, gabbros and granites intruded around 1870-1790 Ma into the Archaean high grade gneisses (Corfu 2004). Since these rocks were not severely affected by the Caledonian orogeny, but resisted deformation, they preserved most of the Precambrian ductile fabrics and structures (Griffin et al., 1978).

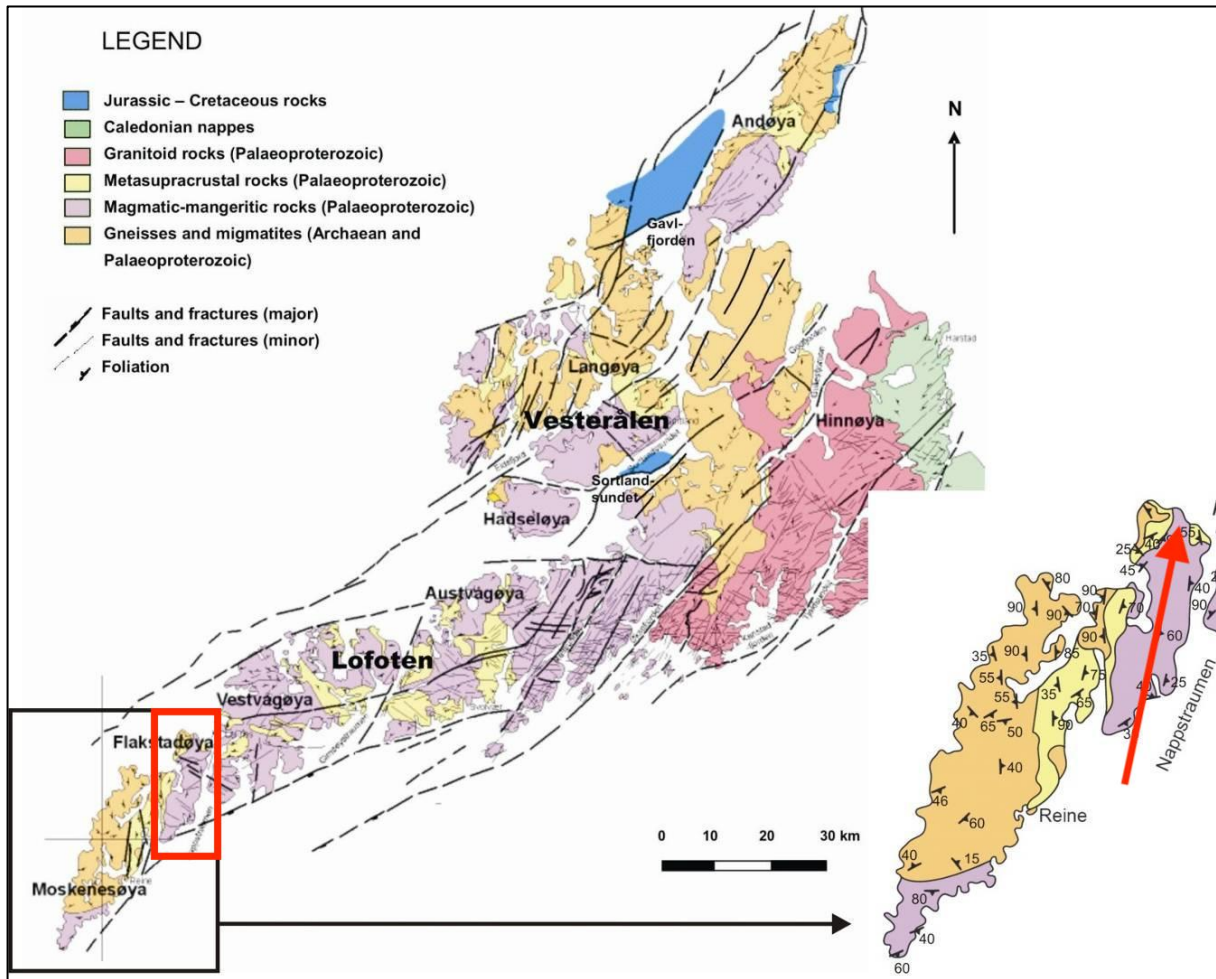


Fig. 4 Bedrocks in relation to age in Lofoten -Vesterålen islands, with faults and foliatin directions. Slettind is marked by red arrow. Modified from (Trullsen, 2008 and Bergh et al., 2007)

The Lofoten ridge was developed as a horst between Mesozoic basins (Vestfjorden and Ribban basins) during several rifting events that created the passive Mid-Norwegian continental margin (Faleide et al., 2008). These events occurred in the Permian-Jurassic to Cenozoic time (Brekke, 2000; Eig & Bergh, 2011; Faleide et al., 2008; Osmundsen et al., 2002). The rifting and opening of the North Atlantic Ocean involved an early ca. WNW-ESE extension direction followed by a NW-SE directed extension, that produced variably oriented, NNE-SSW to NE-SW striking, oppositely dipping normal faults, tilted fault blocks and numerous fracture sets. Northward, the Lofoten margin is linked to the transform plate margin of the Barents Sea along the NW-SE trending Senja-Fracture Zone (Gabrielsen et al. 1990), and this late-stage fault/fracture system is also widespread onshore Lofoten (Eig & Bergh, 2011).

During the Cenozoic-Quaternary, the Lofoten Ridge was tectonically uplifted and exhumed as a horst (Bergh et al. 2007; Hendriks et al., 2010; Schermer et al., 2017) and glacially eroded creating alpine landscapes controlled by local bed rock foliations, steep scarps, valleys, fjords and sounds (normal faults and fractures) and low-relief surfaces (fault blocks, etc.)(Trulssen 2008; Hendriks et al., 2010; Eig & Bergh 2011; Koehl et al., 2018).

Onshore Mesozoic and Cenozoic brittle faults and fractures in Lofoten and Vesterålen have been recently mapped and analyzed (see Fig. 5). These studies indicate the presence of three main fault/fracture sets striking NNE-SSW, ENE-WSW to E-W, and NW-SE, respectively (Bergh et al. 2007; Eig 2008; Gabrielsen et al., 2002; Hansen 2009; Hansen & Bergh 2012). The first set is arranged parallel to many narrow fjords and sounds in Lofoten, e.g. Tjeldsundet, Øksfjorden, Gullsfjorden, Raftsundet, Gimsøystraumen and Nappstraumen (Fig. 5). They all show a straight to right-stepping geometry, where individual fault traces die out or breach along strike. The second set is parallel to the main NE-SW trend of the Lofoten islands and Vestfjorden Basin (Gabrielsen et al. 2002). It is marked by linear escarpments along the coastal cliffs to the north and south of Lofoten (e.g. Myrland to Eggum, and Henningsvær), linear valleys of the interior such as at Leknes and Olderfjorden on Vestvågøya, and the linear depression along Ingelsfjorden (Fig. 5). In all these areas brittle faults/fractures produced rhombic and zigzag-shaped landscapes. The third, NW-SE striking set is well displayed as rectilinear fault-fracture strands along steep valleys and coastal cliff sections in the westernmost Lofoten islands (Fig. 5).

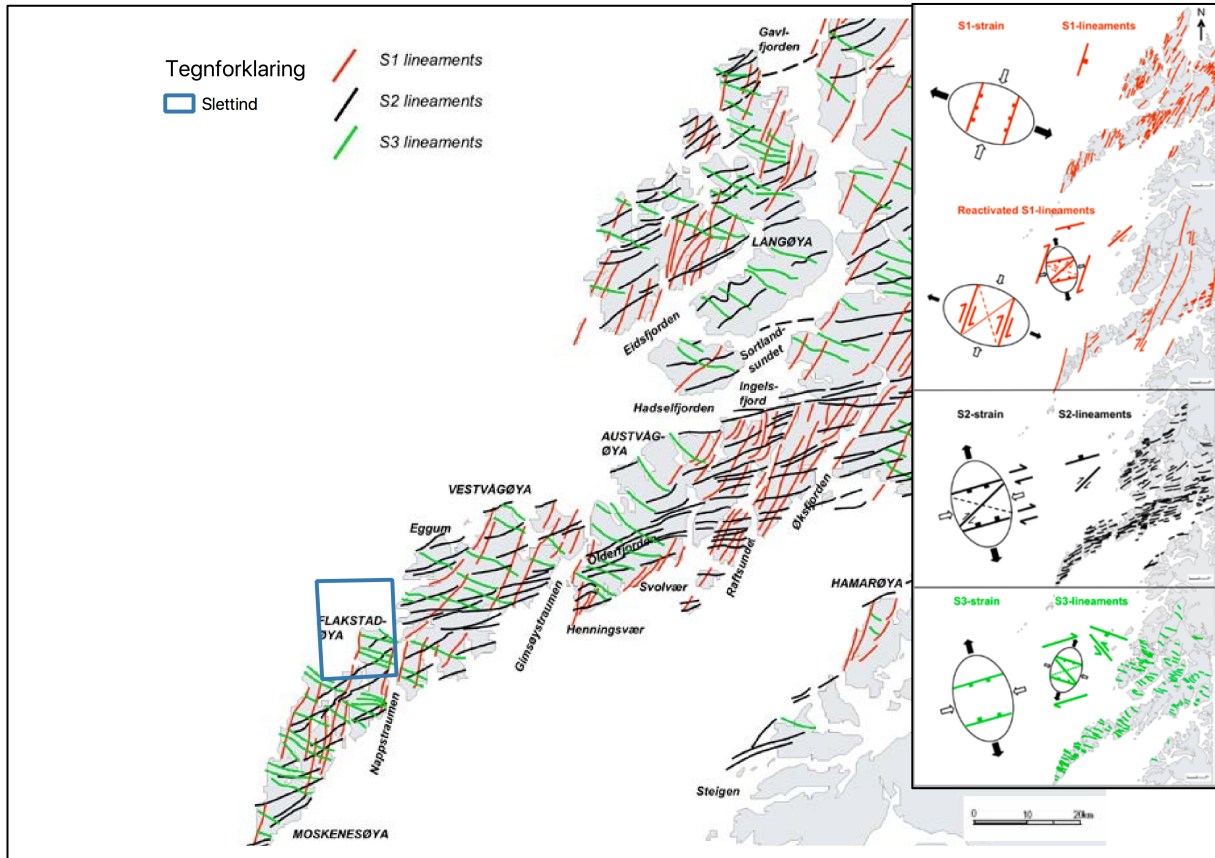


Fig. 5 Lineaments in Lofoten, relative to age where S1 (red) is the oldest, pre-rift lineaments, S2 (black) are younger syn-rifts and S3 (green) post-rift lineaments. Slettind is within the blue box. Retrieved and adapted from (Bergh et al., 2007).

3.1.1 Bedrocks and structures at Slettind

The study area of Slettinden (Fig. 6), is composed of massive and weakly foliated mangerites and mangeritic gneisses of the Palaeoproterozoic plutonic magmatic suite (Corfu 2004; Griffin et al. 1978;). The mangerites are separated on both sides by felsic and mafic Neoproterozoic gneisses, and numerous brittle normal faults and fracture sets of presumed, Mesozoic-Cenozoic age (Bergh et al., 2007). The contrasting massive and competent mangerites and less rigid gneisses, and the many steep brittle faults and fractures found in the study area are critical in order to further describe and evaluate the unstable rock slopes at Myrland/Slettinden.

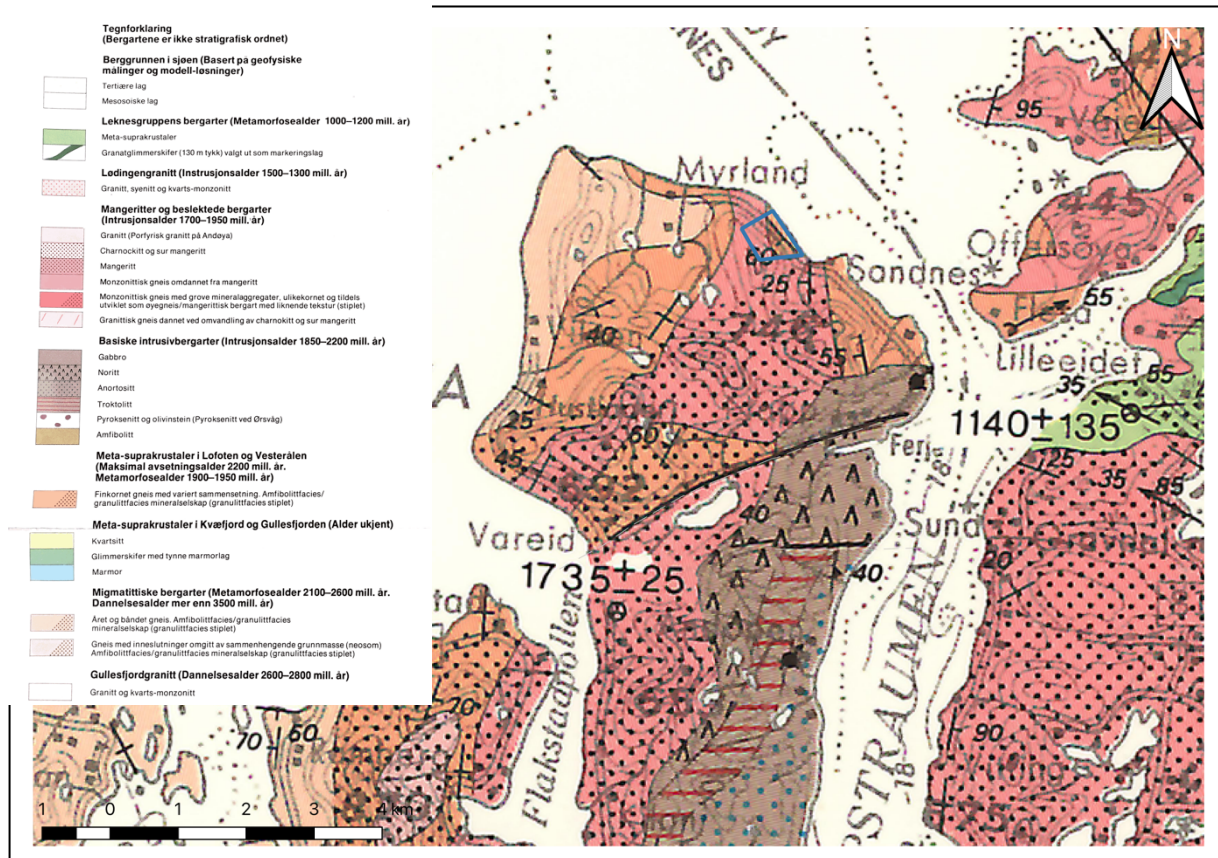


Fig. 6 Geological map of the study area at Myrland, 1:250 000. Study area is within the blue box. This is the most recent WMS layer available. Adapted from Tveten (1978).

3.2 Quaternary Geology of western Lofoten

During the Last Glacial Maximum, Lofoten and the Vesterålen area was completely covered by the Scandinavian ice sheet from as early as 29-28 ka, including marine-based, fast flowing ice streams in the fjords (Hughes et al., 2016). The ice sheet was located at the continental shelf edge along the entire Norwegian coast until about 19 ka BP and the Egga moraines marks the maximum extent (Fig. 7). Lofoten were then covered by a locally active ice sheet during the Skogvoll event (16.9-16.3 ka) (Vorren et al., 2015).

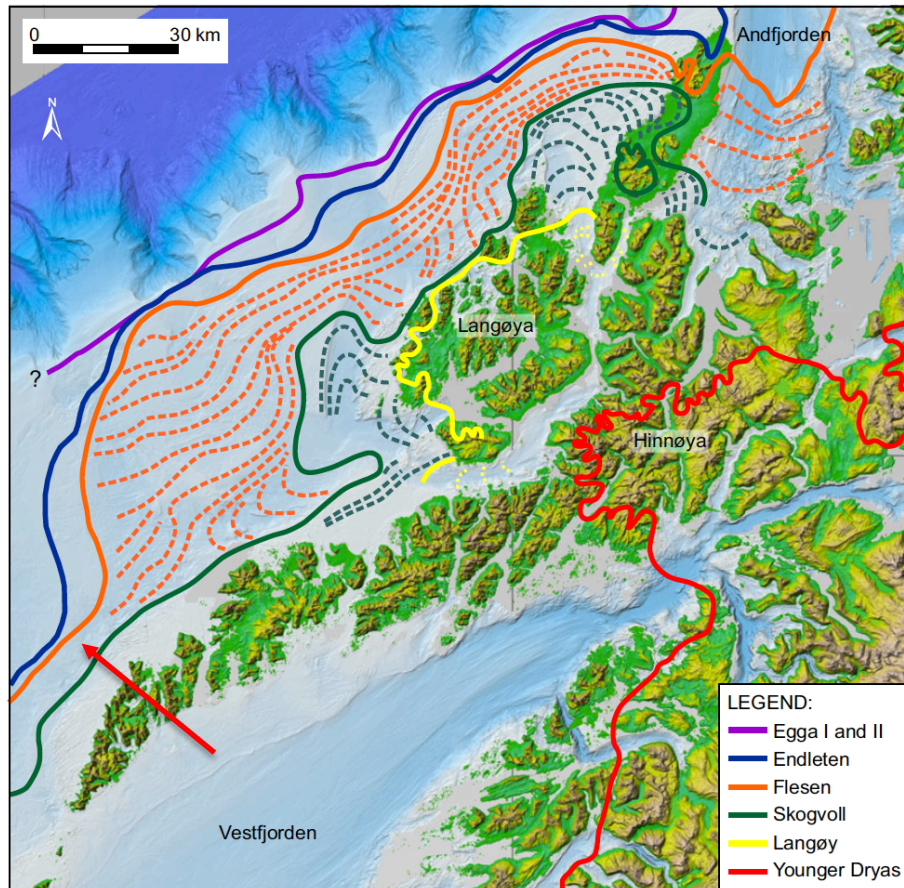


Fig. 7 Ice sheet advances marked by moraines north of Lofoten, the youngest being the Skogvoll event (green) dated to 16.9–16.3 cal. ka BP (Vorren et al., 2015)

There is little evidence of moraines onshore in Lofoten. The ice streams travelled through Vestfjord towards south west and past Andøya towards the north (Fig. 8), and most large moraines are to be found at sea (Laberg et al., 2009; Vorren et al., 2015). The fjords between the Lofoten islands, including Nappstraumen outside of Slettind, have been carved by the ice sheet with flow patterns both northwards and southwards (Fig. 8). The average ice thickness is estimated to 600 m in this area, meaning that today's summit of Slettind was below the ice.

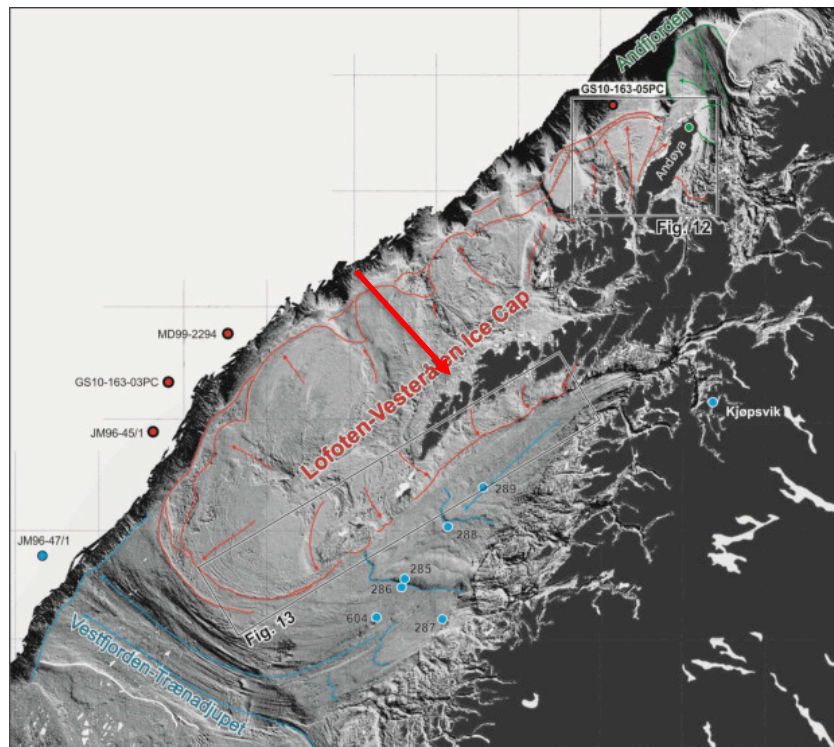


Fig. 8 Ice flow patterns, blue and red represents the two different ice streams, Vestfjorden-Trænadylpet and Andfjorden (Brøndryen et al., 2015). Myrland is marked by red arrow.

Deglaciation around Lofoten islands went extremely fast and the fjords were ice free after the Skogvoll event 16.3 ka and before the Younger Dryas. During deglaciation the sea-level rose to 35-38 m above present day sea level on Andøya (north of Lofoten), before dropping due to isostatic rebound (Laberg et al., 2018). Myrland is further west than Andøya but similar rise in sea-level is to be expected.

When the large ice sheet retreated cirque glaciers and valleyglaciers stayed on the islands. Cirque glaciers erode backwards and downwards and continued doing so after the retreat of the ice from the fjords. The immediate proximity to Nappstraumen suggests that the NE slope of Slettind stopped being affected by glacial erosion when the ice retreated from this stream.

Geochronological data from Lofoten and the beginning of rock slope failures don't exist, however, studies from about 22 rock avalanches in western and southern Norway suggest that the initial deglaciation of the Scandinavian ice sheet was followed by rapid rock slope failures (Ballantyne et al., 2014).

3.3 Climate setting

Lofoten is strongly affected by the passing Gulfstream and often creates a barrier between weather coming from north and south. The islands are very exposed to weather coming from the west, and the prevailing wind direction is from the south west. Lofoten is coldest in February (Fig. 9) with an average temperature of 0°C and is considered the mildest place on earth at its latitude (68°) with an average summer temperature in July (Fig. 9) at 11°C (Store Norske Leksikon, 2009).

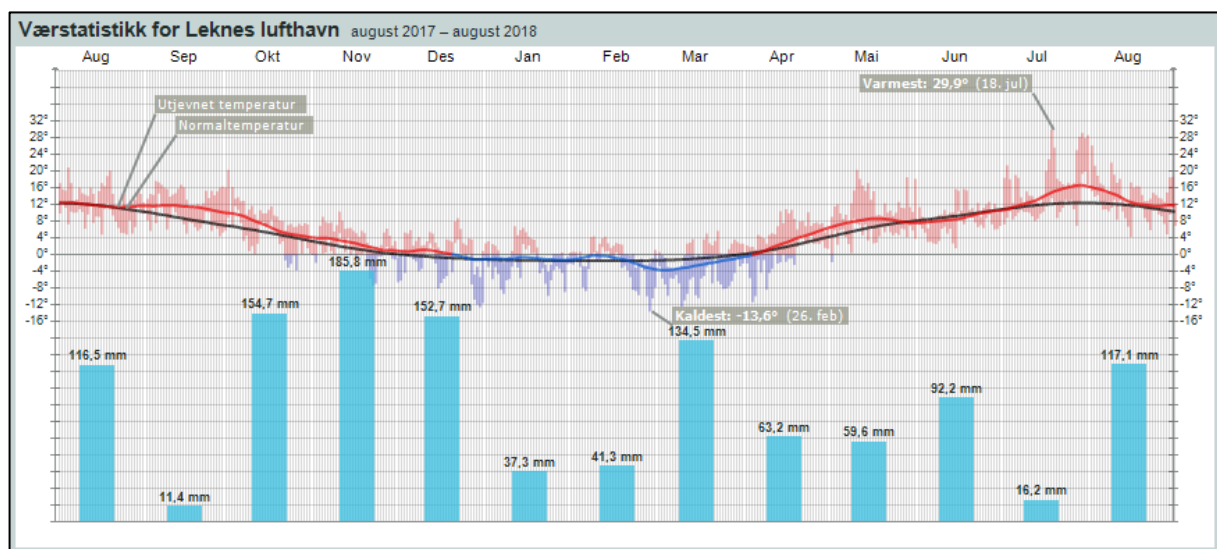


Fig. 9 Weather for one year (aug 2017-2018) showing a short cold period (mid-December to mid-April) and a large amount of precipitation through the year (Meterologisk Institutt, 2018).

The statistics from Leknes Airport from the last six years show winter middle temperature to be between 6-8°C (Nov-March). Maximum precipitation through the same period lies between 32-44 mm/24 hrs, as snow this would translate to approximately 32 cm/24 hrs. There are four events registered during the last 7 years, with precipitation above 40 mm during 24 hrs, and they have all happened in wintertime. In summer the precipitation rates are slightly less (18-32mm/24 hrs), (Appendix 1). The closest weather station that measures snow depth nearby Myrland, (Skjelsfjord, 15 km southwest) have had between 20-40 cm of snow at sea-level through the last six years. The snow depth is expected to be greater at higher altitude, but the mild and unstable winters, in combination with wind, reduces the snowpack through

winter (Appendix 1) (Meteorologisk Institutt, 2018; Xgeo, 2018). Land at sea-level is often snow free in April but rarely before May in altitude.

Climate has been increasingly warmer in northern Norway since 1980s (Fig. 10). Norsk Klimaservicesenter (2018) simulates climate change in Lofoten islands to have some of the largest change in days without snow cover, and an augmentation in precipitation. For the next thirty years, in a worst-case scenario, Lofoten is to expect 90-120 days less snow-covered days in winter and 7.5-12.5% augmentation in precipitation (Fig. 11). This indicates more precipitation falling as rain, and less isolating snow cover exposing rock to freeze- and thaw-events.

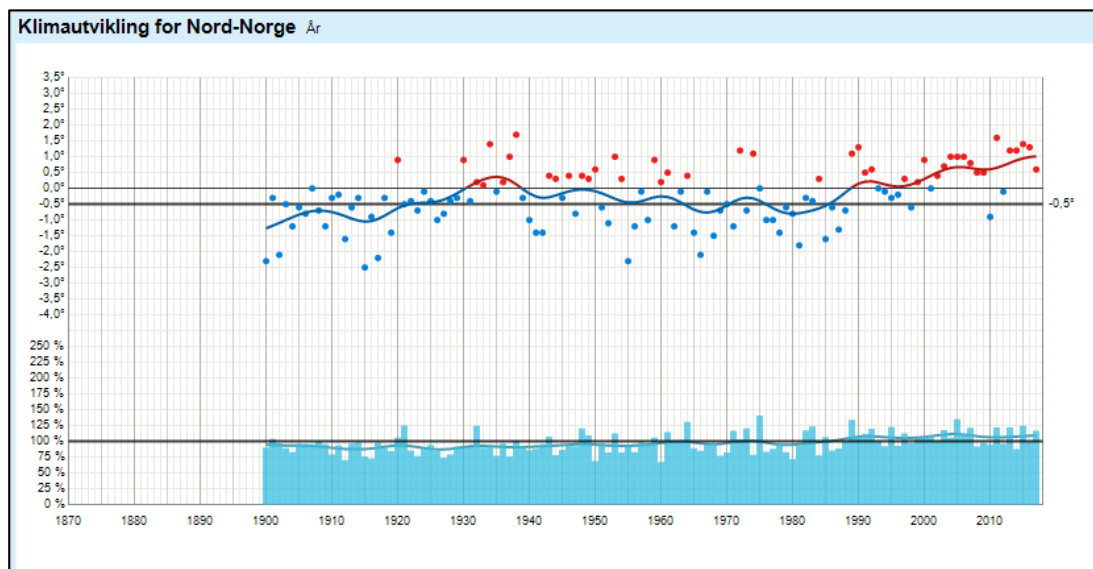


Fig. 10 Blue poles show a variation compared to normal. A rise in average temperature is found from the end of the 1980s (Meteorologisk Institutt, 2018).

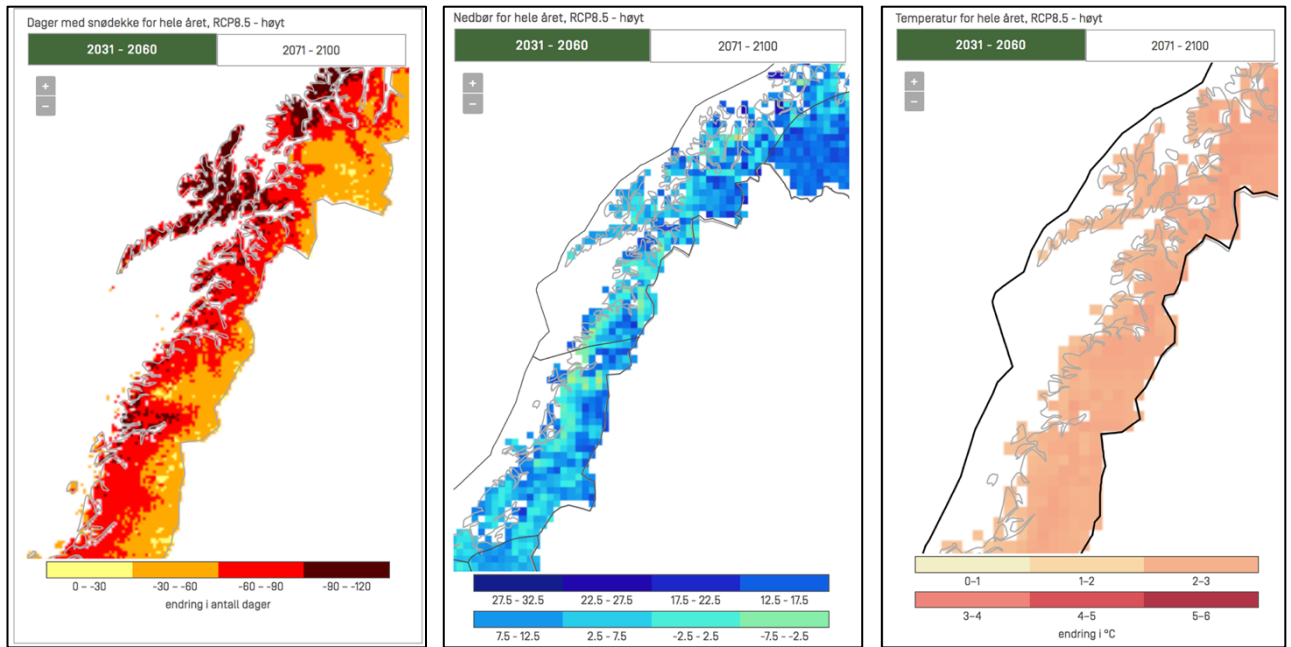


Fig. 11 Worst-case scenario climate change for northern Norway, for the 30 next years. Prognosis indicates less snow, more precipitation and 2-3° warmer average temperature. Retrieved from Norsk Klimaservicesenter (2018).

3.4 Geographic location and topography

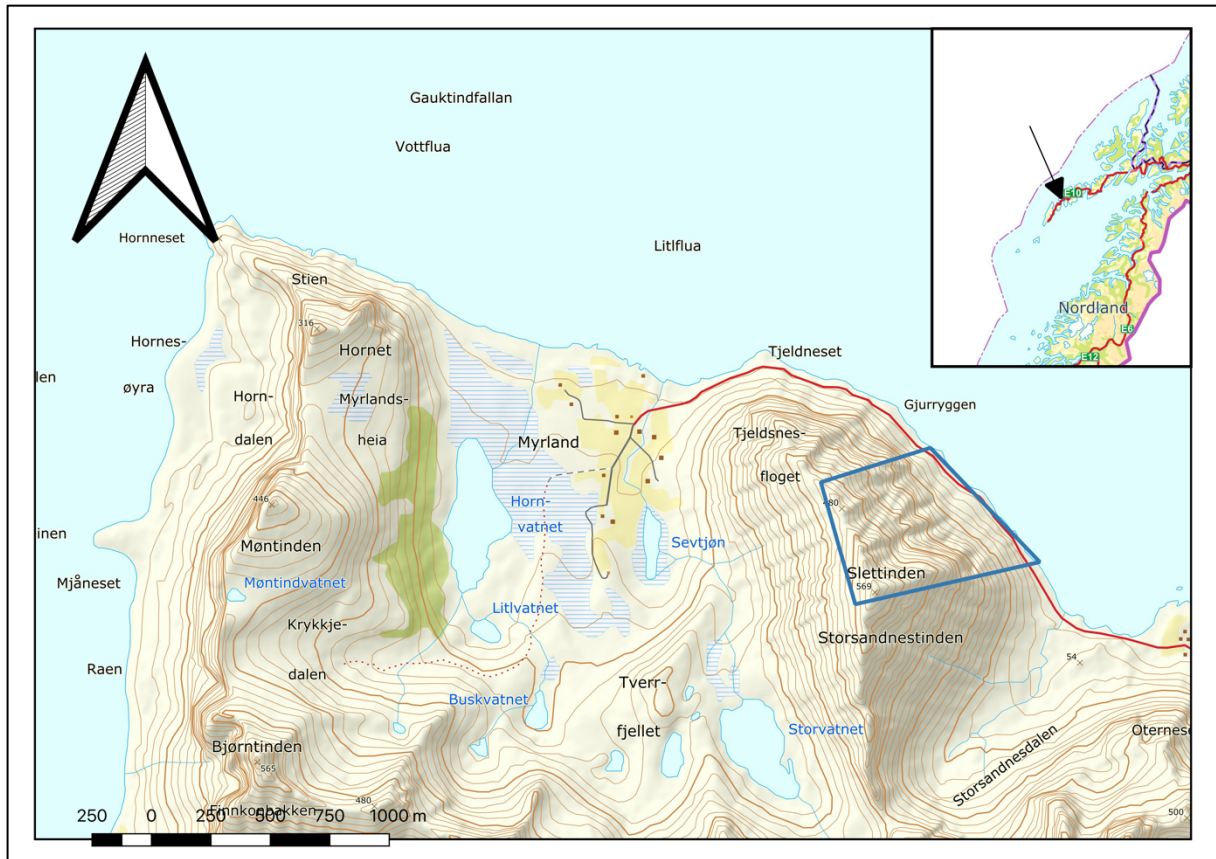


Fig. 12 Topographic map over northern Flakstad Island, and Myrland (middle of the picture) and Slettind (blue box indicates investigated area).

Lofoten is a group of islands in northern Norway stretching in a NE-SW direction oblique to the coast of Nordland (Fig. 12, indicated by black arrow). The islands are all defined by steep mountains and deep valleys, intersected by deep fjords. Myrland is located in the northeastern part of Flakstad Island. The island is situated on the western edge of the archipelago and is very exposed to the weather systems coming from the north with high winds and rough sea.

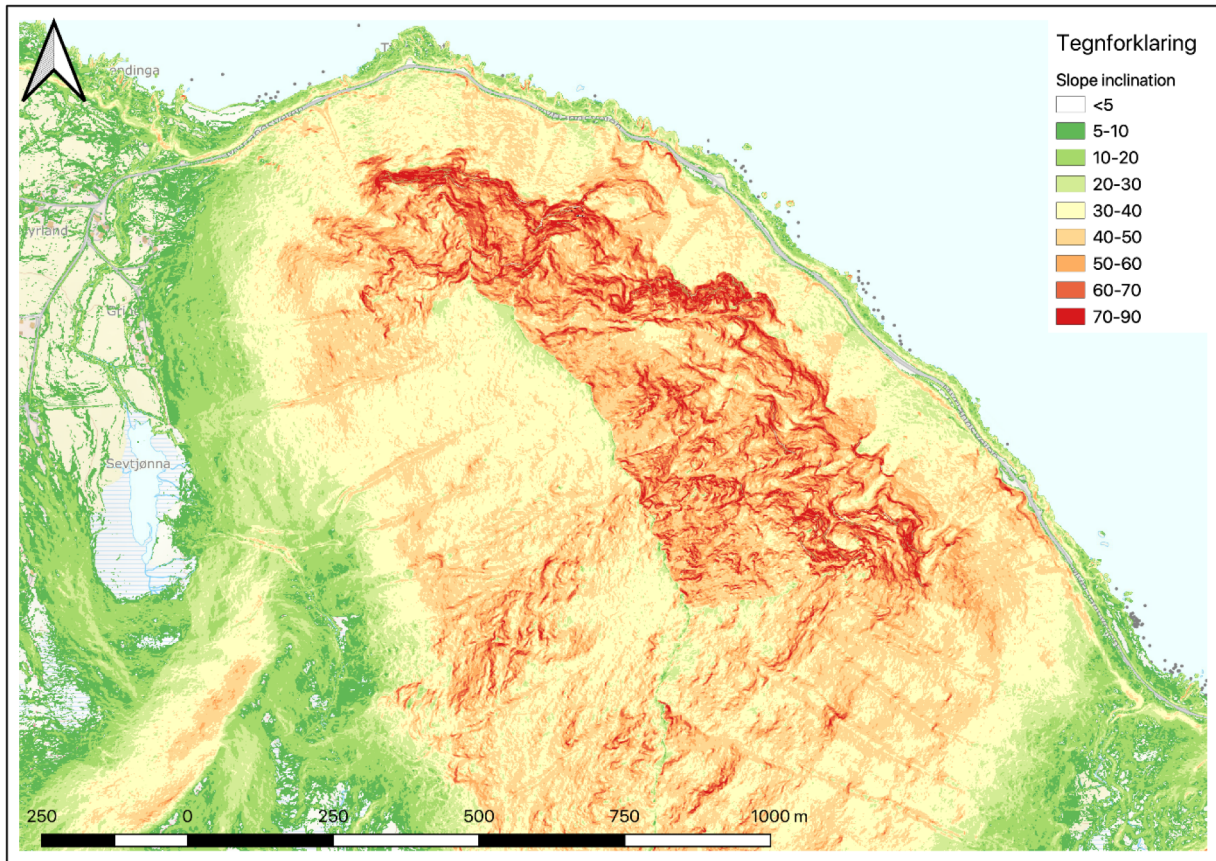


Fig. 13 Slope inclination map at Slettind. 40-70° are considered as potential source areas for rockfall. Rocks are free falling from slope angle >70°, and blocks have continued contact with the surface from <math><30^\circ</math>. The slope doesn't ease to such low angle until the road.

The north-east facing talus of Slettinden, (569 m asl) is composed of very loose and easily dislocated blocks covered with a thin grass vegetation. The upper 100 meters are very steep and over >math>40^\circ</math> (Fig. 13). The steep rockface above the talus (>math>70^\circ</math>) forms larger pillars and grass covered runnels separate shelves. Below the road large boulders (>math>15 m^3</math>) are visible along the entire length of the road and a distance out towards the sea. The south and westfacing wall are covered by grass slopes, and only occasional pieces of rock are visible. Sheep graze on the entire mountain in summertime, and many smaller trails are present. It is difficult to understand the complexity from the road, as it is very steep, and many pillars are only visible from summit or the air.

3.5 Historical events and mitigation measures

Construction of Fv 805 was completed in 1962, and was built by shovel, hand-droven drills by the residents of Myrland (Fig. 12). Previously, the only access to Myrland was by boat, or by crossing the mountain pass by foot. The maximal number of residents at the time was 62 persons at Myrland, mostly fishermen and sheep farmers. The sea has traditionally been the only access to and from the bay but after the pier was destroyed by a storm, residents have been dependent of the road. The initiative to build the road came from an artist who wanted to attract tourism to his farm, and no geohazard evaluation was conducted prior to road construction (Arne Nilsen, personal communication, 2018).

In order to design appropriate rockfall protection one has to evaluate first the hazard vulnerability based on size, run-out distance and frequency of rock fall activity. The frequency of rockfall activity is described in Figure 14 as annual potential return interval. Therefore, the high frequency of events places the site into class I of the SVV risk matrix (Fig 14). In a second step the vulnerability analysis is integrated with a consequence analysis towards a risk evaluation. The consequences can be described in the case of Myrlandsvegen with the amount of traffic passing underneath the exposed area. The “Årlig Døgn Trafikk” (ÅDT) meaning an average of traffic spread over the year at a daily basis, is set to 65 at Fv805 (SVV, 2018), placing the road well within category A (Fig. 14).

Rockfall events have been logged in various ways through the years. For a number of years, the locals had the responsibility to register each time boulders or (rock/snow) avalanches hits the road, with date, time and weather specifications recorded. Today this is done by the entrepreneur responsible for maintenance in the area.

The locals know that a higher frequency of rockfall reported may push government and municipalities to invest in road protection and therefore, might report more rockfalls per year to increase the risk to yellow based on a higher frequency of events placed in group I (Fig. 14). As SVV has reported (Statens Vegvesen Region Nord, 2015) protection is very expensive. So far, no protection has been built and the only action has been closing the road when rockfalls or snow avalanche danger is high, or immediately following impact events. The result is that the locals tend to report fewer events than what is the actual case, to keep the road open (Mortensen, personal communication, 2018).

The entrepreneur is supposed to inspect the road at a weekly basis and then log if there has been any rockfall since last inspection. This is not necessarily the practice and in recent years it has been more common to do one summer inspection logging all rocks lying at, or on the road, as cumulative rockfalls that have fallen since after the snow melted. It is also expected that rocks that have crossed the road and landed in the sea are not registered, except very large specimens that are easily observed.

Årlig nominell skredssannsynlighet pr. enhetsstrekning	I ≤ 1/2	Yellow	Red	Red	Red	Red	Red
	II ≤ 1/5	Yellow	Yellow	Red	Red	Red	Red
	III ≤ 1/10	Green	Yellow	Yellow	Red	Red	Red
	IV ≤ 1/20	Green	Green	Yellow	Yellow	Red	Red
	V ≤ 1/50	Green	Green	Green	Green	Yellow	Red
	VI ≤ 1/100	Green	Green	Green	Green	Green	Yellow
Trafikkmengde (ÅDT)	A < 200	B 200 - <500	C 500 - <1500	D 1500- <4000	E 4000- <8000	F ≥ 8000	
■ Akseptabel strekningsrisiko		■ Tolererbar strekningsrisiko. Aksept avhenger av skredintensitet og kost-nytte-analyse. Akseptnivå besluttes på regionledernivå.		■ Uakseptabel strekningsrisiko			

Fig. 11 Risk matrix from Statens Vegvesen (Eidsvig, 2014), the Norwegian Road authority, integrating the hazard vulnerability as the annual potential return interval (Y-axis) with the consequences described as traffic amount per day (ÅDT; x axis)

This is why the rockfalls reported in recent time may not be accurate by date, weather or temperature and it is difficult to use this for statistical purposes. The habit of reporting volume is also differing, as some inspections at larger rockfalls have noted “rocks covering 45 m of the road” which doesn’t say much of volume or block size. Only larger events will be precise as the locals will alert authorities, and reports from SVV contains detailed pictures.

All historical events registered are shown in Fig. 15 and contains data from both SVV and NVE. In Fig. 15 one dot shows where a rock has landed, or a snow avalanche hit, but doesn't necessarily contain information about source. If a rock has been moved by locals or tourists travelling the road prior to inspection the location might not be accurate.

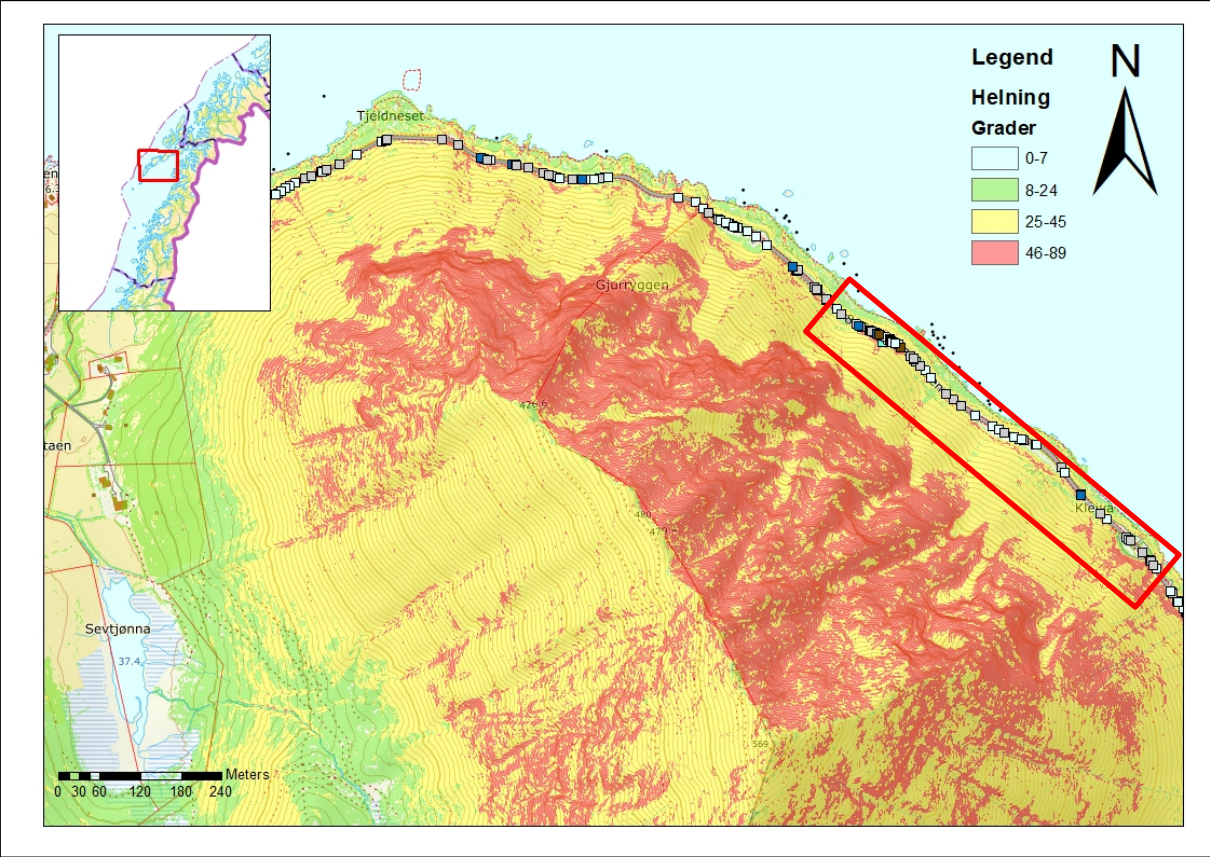


Fig. 15 Historical events registered in NVE database, including rockfall (grey dots), earth slides (brown), ice fall (blue) and snow avalanche (white), with slope inclination map over Slettind.

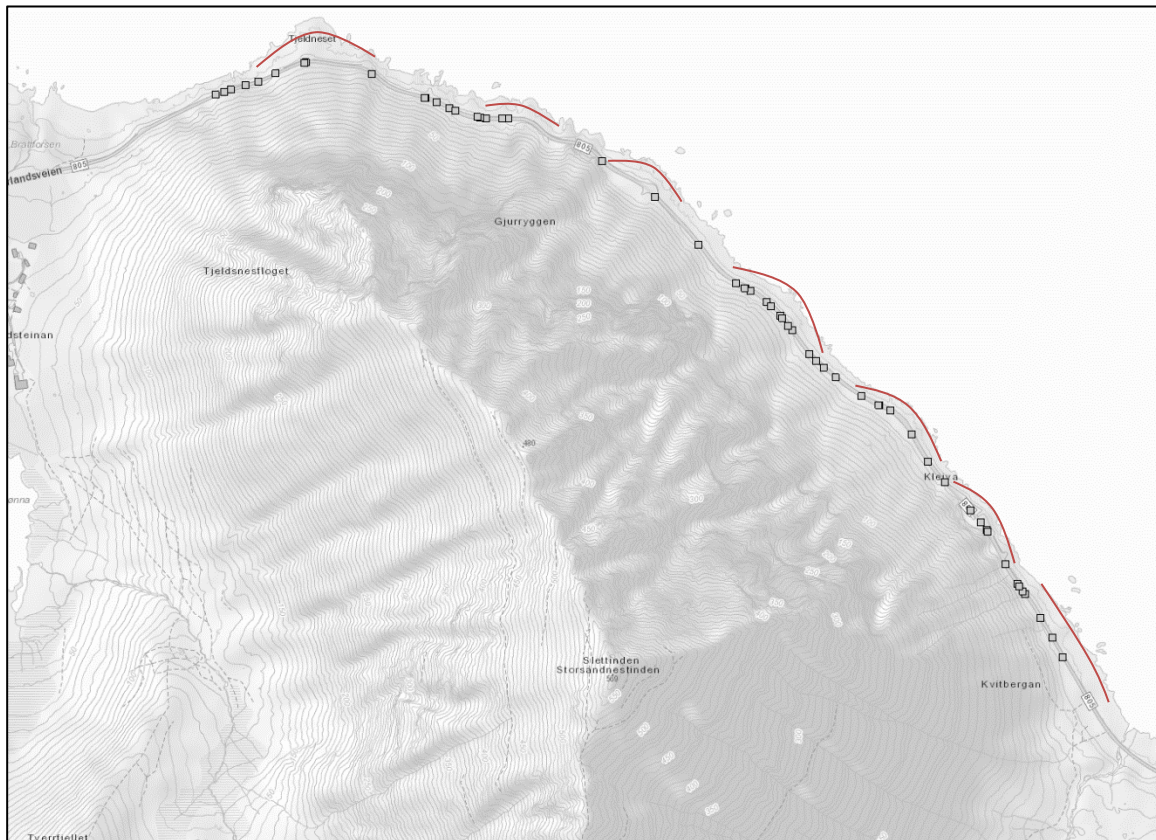


Fig. 16 Historical events from SVV database, sorted only on rockfall events (grey markers). One marker can represent one or multiple events. Rockfalls seem to concentrate at at the bottom of debris fans (marked in red lines).

Hazards reaching the road, sorted on only rockfall, from SVV (Fig. 16) contains observations about the source area (Fig. 17) (in total 14 observations), only one of the sources for rockfall is higher than 200 m in altitude, meaning that most of these rockfalls are released from low on the rockwall. Out of 123 registered rockfall events, 18 of them has resulted in closure of the road.

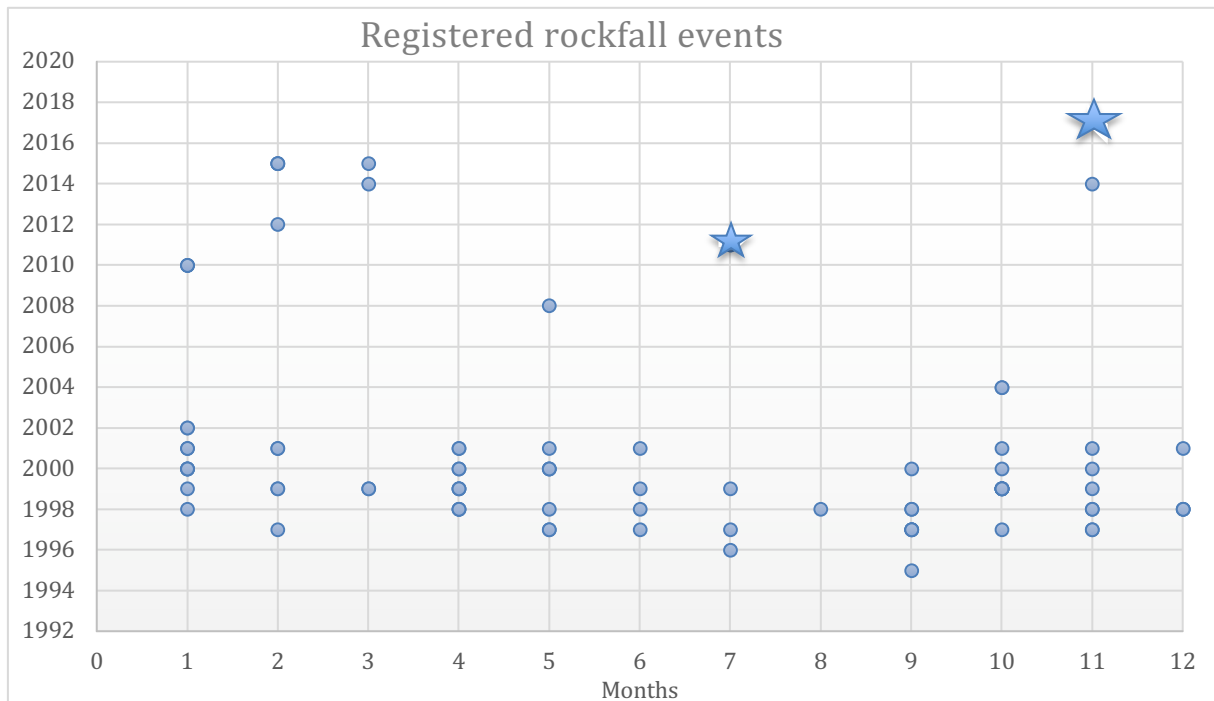


Fig. 17 Registered rockfall events displayed over months and year, stars mark the two major events of 2011/17. There were more registered events 1997-2002, which is a result of logging differences, and so is also the gap between 2004-2008. There seem to be a trend of less rockfall during summermonths.

The many incidents through the years have seen different propositions of mitigation. Already in 1978 (Grimstad) deemed it was necessary to build 7 protective structures over the road, over a total length of 300 m. Avalanche report from 1984 (Lied) suggests a 1,8 km long tunnel, as the best way to protect the road from rockfalls. In 2008 (Aronsen), reported about weekly rockfalls. Based on earlier reports it was decided to create a trench between the mountainside and road, but this resulted in a near-accident with rock hitting an excavator as the slope started to move when they tried to dig out the toe of the talus. SVV then concluded that the only reasonable way of protecting the road was tunnel.

In 2011 there were two events following major rainfall, 19th of July a large rockfall of 70-100 m^3 reached the road, and a couple of days later on the 25th of July a rock avalanche of 2000 m^3 closed the road (Fig. 18 and 19). After the rock avalanche in 2011 the source area was flushed with water from helicopter (Kvalvågnes, 2011), which cleared 100 m^3 of rock masses. In November 2017 there weren't any unusual amount of precipitation but 16-25th November 2017 a rock avalanche of 3000 m^3 from the same source closed the road (Fig. 20). After the incident the road has been recommended to be closed in wintertime when

precipitation >10 mm/24hrs (Persson, 2011) and temperatures >4° (Aronsen, 2017) as the only mitigation.

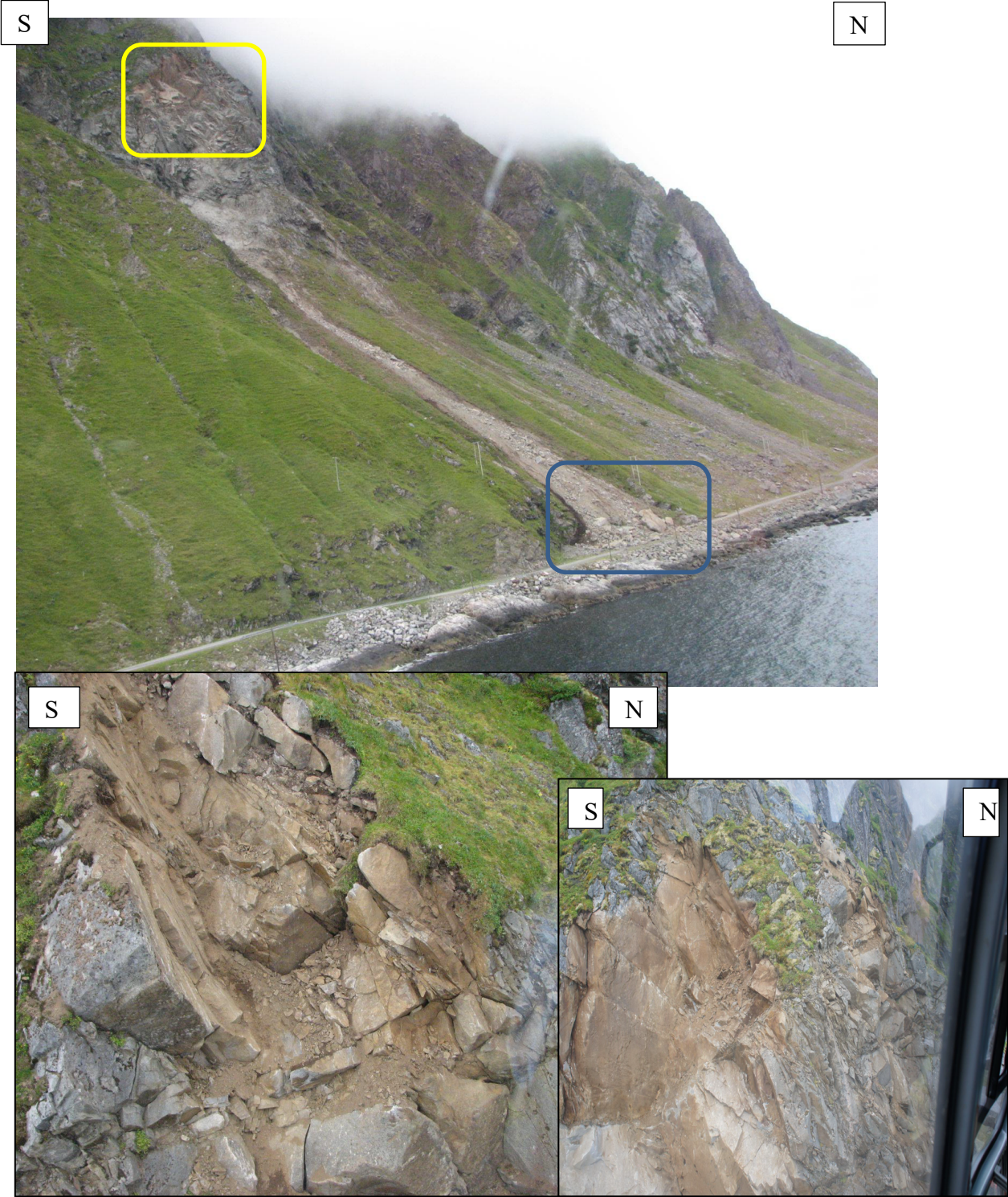


Fig. 18 Pictures taken from helicopter after the rock avalanche in 2011, showing the release area (yellow), and avalanche path and deposit (blue). Visible joint sets and more loose blocks underneath a thin layer of soil. Picture taken by Persson, SVV, 2011



Fig. 19 Debris on the road, after the rock avalanche in 2011. The large boulder in front of the man is still in place, keeping the talus slope stable. Picture by Persson, SVV, 2011

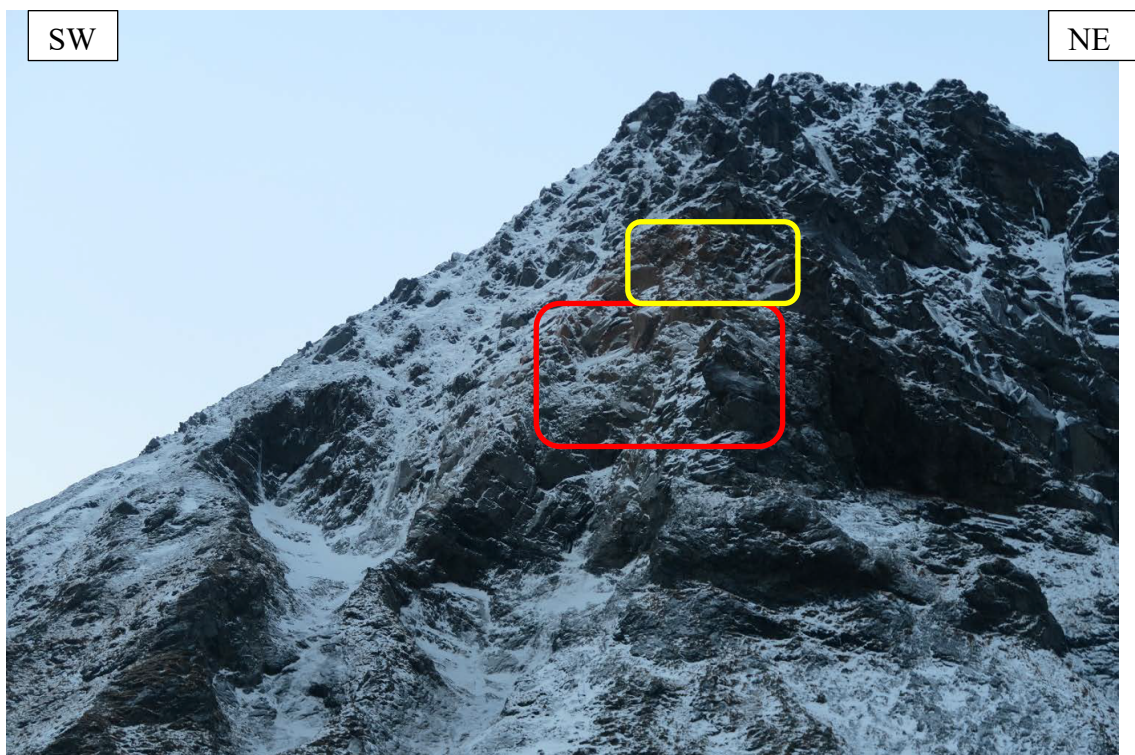


Fig. 20 Release area after the rock avalanche in 2017. The release area in 2011 is marked in yellow, and the fresh from 2017, in red. Picture by Aronsen, SVV, 2017

4 Methods

4.1 Field work and data acquisition

Fieldwork at the site was carried out 6th to 12th of June, and 17th of July. It consisted of field/outcrop mapping, geomorphic mapping, structural orientation data and UAV campaigns.

The outcrops that were accessible from the road were mapped, and structural orientation data were made using a compass measuring dip and dip direction. This was validated against the app GeoID, which was further used on every outcrop on an Iphone. GeoID has been tested to be one of the most precise apps if used on an Iphone, and the amount of measurements done statistically eliminates any bias that might occur. The ability of a traditional compass shows that today's modern smartphones are as precise as traditional compasses, but needs to be calibrated and validated before use (Lee et al., 2018). The app Clino Fieldmove was also used to measure dip and dipdirection both for comparison between the two apps, but also to increase the number of measurements. Clino Fieldmove was also used on an Iphone.

Five different hand samples from the outcrops were collected for geological description purposes (Fig. 21). Every location was photographed and rocktype, joint sets and foliation was described.

Handsamples are logged as following:

Location 1.a: Handsample 1

Location 1.b: Handsample 2

Location 2: Handsample 3 and 4

Location 3: Handsample 5

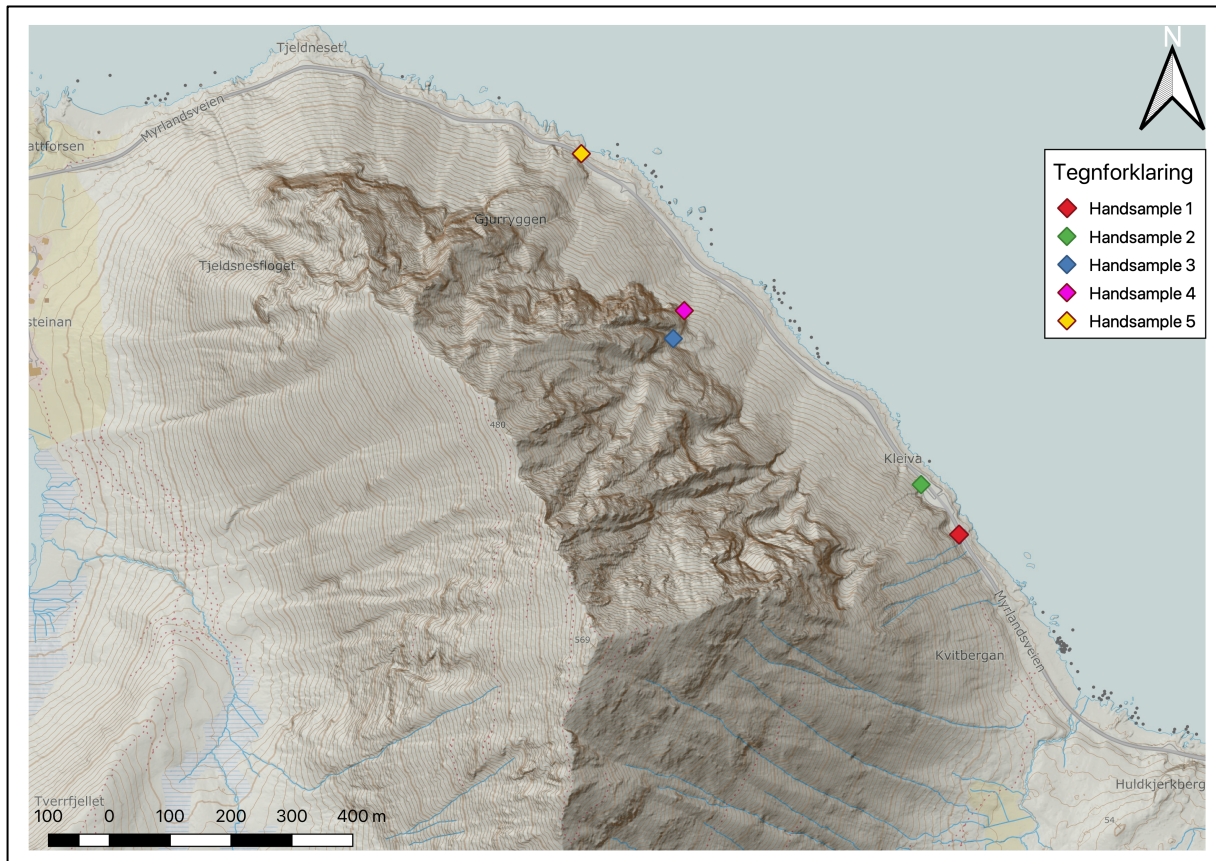


Fig. 21 Map showing locations where handsamples were retrieved

Measurements from the compass, GeoID and Clino Fieldmove were later assembled into Dips 7.0 by Rocscience (2018) to create stereonet and kinematic analysis.

4.2 Rock mass classification with GSI

Based on the failure criteria of (Hoek & Brown, 1980) the Geological Strength Index (GSI) was introduced (Hoek, 1994; Hoek et al., 1992; Hoek et al., 2000). The rock failure criterion and index were designed to be used based on visual observations in the field, to find the strength of the rock (Fig. 22). It considers the rock mass property such as lithology, structure and condition of discontinuity surfaces. It has later been developed and further adapted to different types of rock (Hoek et al., 2002). The number applied can then be used in numerical analysis, in particular it can be used to calculate the compressive strength (σ_{cm}) and deformation modulus (E).

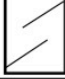
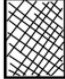




GEOLOGICAL STRENGTH INDEX FOR JOINTED ROCKS		SURFACE CONDITIONS					
		VERY GOOD	GOOD	FAIR	POOR	VERY POOR	
STRUCTURE		DECREASING SURFACE QUALITY →					
	INTACT OR MASSIVE—intact rock specimens or massive in situ rock with few widely spaced discontinuities	DECREASING INTERLOCKING OF ROCK PIECES ↓	90				
	BLOCKY—well interlocked undisturbed rock mass consisting of cubical blocks formed by three intersecting discontinuity sets		80				
	VERY BLOCKY—interlocked, partially disturbed mass with multi-faceted angular blocks formed by 4 or more joint sets		70				
	BLOCKY/DISTURBED/SEAMY—folded with angular blocks formed by many intersecting discontinuity sets. Persistence of bedding planes or schistosity		60				
	DISINTEGRATED—poorly interlocked, heavily broken rock mass with mixture of angular and rounded rock pieces		40				
	LAMINATED/SHEARED—Lack of blockiness due to close spacing of weak schistosity or shear planes		20				
						10	

Fig. 22 GSI index is based on visual inspection of the rock and compared to a scheme, that gives a destined value. Retrieved from Marinos et al. (2005)

4.3 Rock mass classification with Q system

The Q system was developed to help designate tunnels (Barton et al., 1974). Parameters such as joints, friction and rock mass strength are given a value that, shown in a chart, designate how much and what type of protection the tunnel would need (Fig. 24). It has later been further developed with more parameters to solve more specific problems and become more flexible. It is commonly in use in outcrops, although it may not be well designed for this, as it was created for tunnel roofs (Palmstrom & Broch, 2006). To calculate the stability of a rock mass (Barton, et al., 1974) the equation is based on the three important factors: the degree of jointing (block size), joint friction and stress (Barton, et al., 1974; Barton & Bandis, 1990; Barton & Grimstad, 2004).

$$Q = \frac{RQD}{J_n} \times \frac{J_r}{J_a} \times \frac{J_w}{SRF}$$

RQD= Rock quality designation

J_n= Joint set number

J_r=Joint roughness number

J_a= Joint alteration number

J_w=Joint water reduction factor

SRF= Stress reduction factor

The Q system developed by NGI are related to a schematic support chart, where means (type and support) for securing rock masses depend upon their Q-value (Fig. 24).

The RQD/J_n value shows the overall quality of the rock, where joints per m^3 is divided by the amount of joint sets, to give an indication of block size.

The J_r/J_a represents roughness and frictional characteristics of the joint planes (Fig. 23), divided by the amount of coating and filling, and is the parameter that indicates shear strength.










		JRC ₂₀	JRC ₁₀₀
	Stepped		
Rough		20	11
Smooth		14	9
Slickensided		11	8
	Undulating		
Rough		14	9
Smooth		11	8
Slickensided		7	6
	Planar		
Rough		2.5	2.3
Smooth		1.5	0.9
Slickensided		0.5	0.4

Fig. 23 Rock surfaces classification for use with the Q system. Retrieved from NGI, 2015

The Jw/SRF needs to be tested in laboratory and shows the active stresses that affect the rock mass strength, by dividing the amount of outflow by shearzones or open joints. Swedish Trafikverket (2015) uses Q-base values, putting the Joint Water reduction factor and Stress reduction factor to 1, assuming no water in-put (dry conditions) and tight structure.

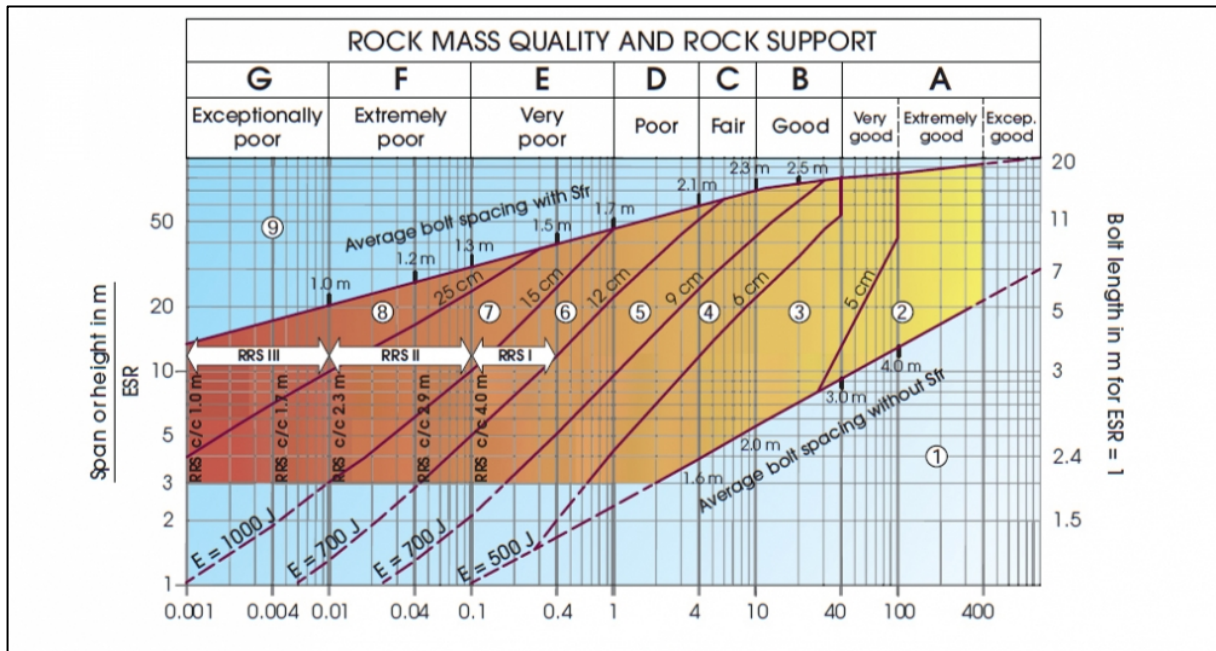


Fig. 24 The Q-chart that estimates rock mass quality and support needed, developed for tunnel support. Retrieved from NGI, 2015.

The Q-system app developed by NGI in 2015, was used on an iPhone to log estimates in the field.

4.4 GIS -Software and visualization

QGIS 3.2.2 has been used for geographic projection of geomorphology and structural geology maps in coordinate system ETRS89/WGS 84 UTM 33N. QGIS is open source software and builds models and maps in 2D and 3D, and can along with digital elevation models (DEMS) be used for analysis of release areas based on the slope angle, calculation of shadow angle, identification of deposit fans, run-out distances etc (Derron et al., 2005; Frattini et al., 2009; Jaboyedoff et al., 2007; Jaboyedoff et al., 2012).

The ortophoto (Flakstad Vestvågøy 2013 series) has been retrieved from www.norgebilder.no (accessed 2018), and also extracted from drone photogrammetry. The digital terrain model (DTM; NDH Lofoten 2 pkt 2017 series with a 0,5 m resolution) has been

retrieved from www.hoydedata.no (accessed 2018). The 1: 250,000 Bedrock map NGU (1978) is used, as no public bedrock map with more detail exists.

4.5 UAV surveys

The entire site area prone to rockfall, was too wide and too high an area to cover with the drone, so a 500 m-long section was selected for photogrammetry purposes.

Six GCPs were marked with orange spraypaint (Fig. 25) and logged with a Montana Garmin handheld GPS and Leica dGNSS system. Additionally, 3 GCPs were marked and logged with the handheld GPS on Slettinden summit.

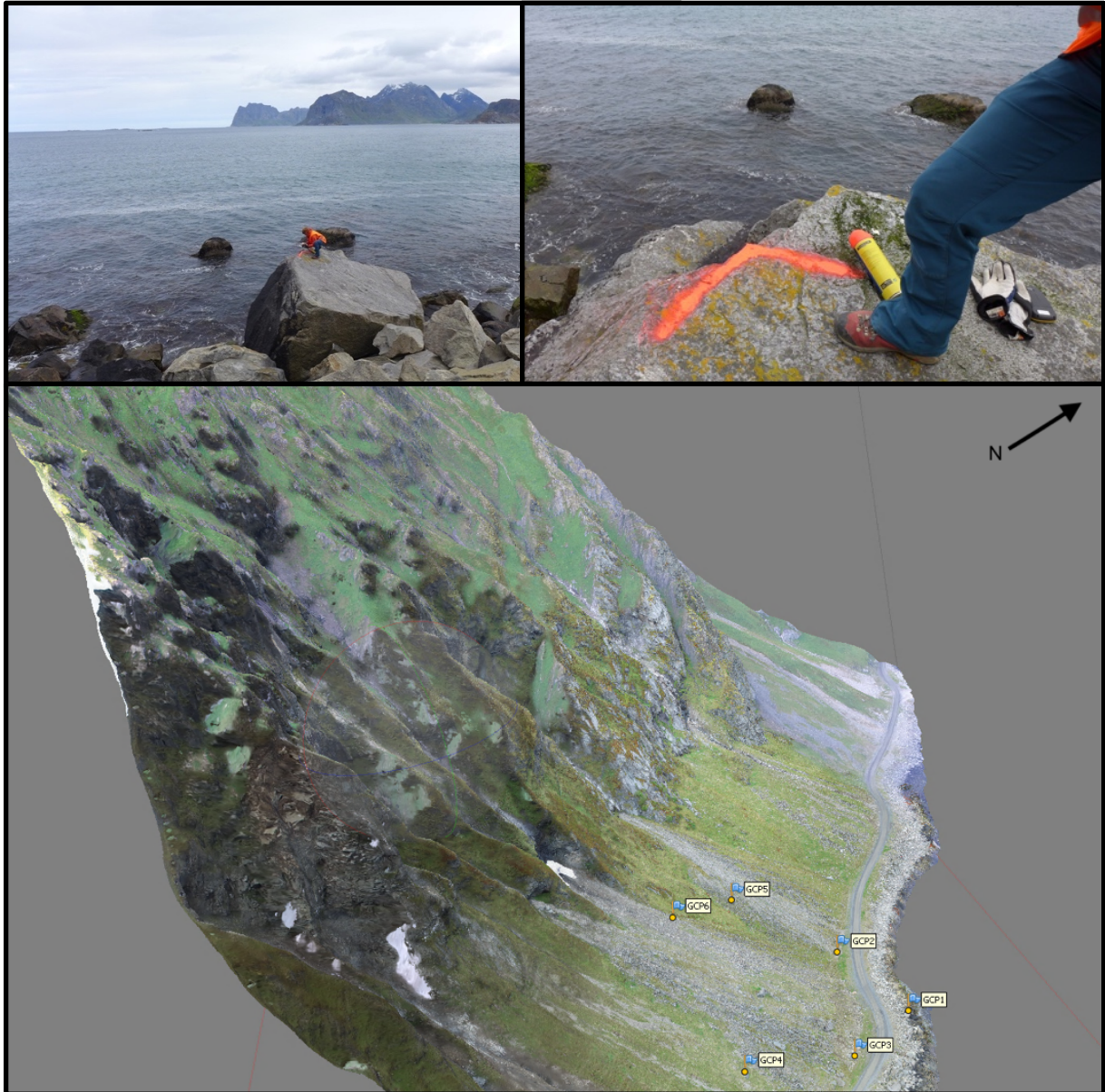


Fig. 25 Spraypainting the GCPs on large and easily recognized boulders. The 3Dmodel derived from the drone photogrammetry shows the locations of the GCPs with blue flags. Private photographs, 2018.

The UAV used was a DJI Inspire 1 with a Zenmuse X3 camera, 4 K video, 12-megapixel photos, and a 3-axis gimbal (Fig. 26).



Fig. 26 The DJI Inspire1 is a large drone constructed for being stable at high altitude and taking good quality images. Picture from Drone business directory (2014).

4.5.1 Flightplan

The flight was done at two different occasions, firstly the manual flying vertically along the NE slope, and secondly horizontal grids from the summit. The weather was very poor during the fieldwork in June, with too much cloud at the summit to conduct the orthographic flight. The horizontal grid flown in Pix4D Capture was therefore done in July. The weather was very good during this period, and the resulting pictures came out much brighter. There was also a great difference in grassgrowth, a fact that can be inconvenient when trying to merge models.

Manual flying was carried out in three flights at three elevations (Table 1) at the wall front. Flights used different camera angles to capture most of the structure of the wall. Photos considered too dark were excluded later before processing, resulting in 1122 images used.

Tabell 1 Manual flightplan, showing altitude over sea-level, camera angle, speed and Ground Sample Distance (GSD).

Elevation (m asl)	Camera angle from horizontal	Speed of drone (m s⁻¹)	GSD (cm px⁻¹)	Comments
Manual flightplan				
80,4	-80°	3	3,72	Poor light
	-60°	8	4,04	
	-45°	4-5	4,95	
	-80°	4-5	3,55	
	-30°	5-6	4,6	
119,7 -120,8	-45°	3-5	7,42	
	-60°	3,5-5	6,06	
149,7-150	-70°		6,98	
	-60°		7,58	
	-45°		9,28	
Pix4D horizontal grid				
650	-70°	Fast	4,66	

During the orthographic flight from the summit, five hundred images were produced from two (654x349 m and 563x351 m) grids. The strong light conditions affected the images such that the summit ridge was very bright, and the painted GCP points were not visible. It was difficult to locate exact positions of the ground-based GCP points and these were approximated later during processing.

4.5.2 Structure-from-Motion processing

Photogrammetry creates 3D surfaces by using overlapping images and Structure-from-Motion technique uses algorithms producing grids with x, y, z values. It has a documented agreement within a 1-3 degrees on joint orientations (Westoby et al., 2012). The resulting model is similar to LiDAR but cheaper and more flexible to use, as SfM isn't dependent on ground control points, but uses the drone as a moving sensor and georeferenced each photograph with coordinates (Bemis et al., 2014; Müller et al., 2014; Westoby et al., 2012).

An accurate model from SfM techniques may be prevented by homogenous surface texture, changes in the target, spatial resolution or illumination. Surveys longer than 30 mins with changing light can cause high variation in the image texture. The method involves keypoints that are identified and linked, minimum two are needed to create a track, and those images that don't meet this criterion are discarded. This means that unwanted objects are automatically removed, such as birds or dirt on the lens.

Automatic programs designed to use with UAV is for example Pix4D, where the flightplan can be designed together with other settings, such as overlap percentage, camera angle and flight speed.

In point clouds deriving from SfM, it is possible to detect structural geology, generating discontinuity data, and assess rockfall susceptibility (Derron et al., 2005; Dewez et al., 2016; Jaboyedoff et al., 2007; Jaboyedoff et al., 2012; Matasci et al., 2017). Drone imagery is particular useful in steep or overhanging rock walls as pixel distortion is avoided by the amount of different camera angles. TLS and satellites drapes a 2.5 D onto a 3D model which leads to errors in elevation positions of pixels and blurry spots (Gigli et al., 2014; Matasci et al., 2017; Müller et al., 2014; Pavlis & Mason, 2017). The DEM of the site of Myrland deriving from satellites is for example affected by shadowing, making it difficult to use.

Agisoft Photoscan is a software that assembles drone imagery and has been extensively used in creating 3D models. Agisoft recommends a 64-bit processor and 12 Gb RAM memory for processing 200-300 images, for a large project containing over 1000 photographs the only processor capable of handling the processing had following specifications:

Processor: Intel Core i9-7900X (10-Core, 20-Thread, 3.3/4.5GHz)

RAM: 128 GB

OS: Win 10, 64-bit

GPU: 2x NVIDIA Titan XP (12 Gb/card)

4.5.3 Agisoft workflow

Agisoft (2018) has a well outlined workflow to follow.

All the images are reviewed one by one, manually deleting the ones too blurry or unclear for use. The software has a function that can handle this, but for optimizing the result it is better exclude images with unreliable quality, especially with such a large dataset. Photos were then organized based on the flight height and loaded into one chunk in the software and aligned. It took almost a full day to align 1622 photos, and later this model would fail due to a too large

overlap between manual taken photographs. The first test took almost one week, and it was then opted to try to load photos into different chunks, for merging later. All chunks were processed individually and markers for the GCPs were placed manually. Upon merging the chunks the software didn't manage to align the chunks properly, as all of the GCPs were not visible on every chunk. Too few references caused the model to become skewed.

The photos were once again loaded into one chunk and aligned after Agisoft's recommendation (Agisoft Support Team, personal communication, 2018). This time they aligned properly, and in a shorter time, possibly due to the GCP markers already being placed. The error in space at this stage of processing has an error of about 38 m as seen in Fig. 27.







Cameras	Longitude	Latitude	Altitude (m)	Accuracy (m)	Error (m)
<input type="checkbox"/>  DJI_009...	13.396730	68.161678	48.385000	10.000000	38.030143
<input type="checkbox"/>  DJI_009...	13.396730	68.161678	48.385000	10.000000	38.038307
<input type="checkbox"/>  DJI_009...	13.396735	68.161676	48.385000	10.000000	38.056668
<input type="checkbox"/>  DJI_009...	13.396747	68.161671	48.285000	10.000000	38.203621
<input type="checkbox"/>  DJI_009...	13.396766	68.161662	48.385000	10.000000	38.084524
<input type="checkbox"/>  DJI_010...	13.396795	68.161650	48.385000	10.000000	38.082420

Fig. 27 The cameras (position of the drone at the instant of taking the image) are here used as the only x,y,z reference. Position, altitude and error in distance for each image taken by the drone. The estimated error is calculated between the known camera locations and the position of the object.

The photos were aligned following the recommendations from Advanced geo (2015), Agisoft (2018), Dinosaurpalaeo (2015) and the option accuracy was set as “high”, generic preselection is a function that deletes non-overlapping photographs and it was set as active, key point limit (amount of points sampled on each photo) was set to 60 000, and tie point limit (amount of points tied together between the photos) were analyzed later.

The sparse cloud is then scanned for points being in the wrong place or of bad quality. The gradual selection “reconstruction uncertainty” was set to 100. Alignment was again optimized. “Reprojection error” was set to 0.5, and “Projection accuracy” to 10.

The ground control data were imported, and the markers were placed individually on each photo. They were not marked if the GCP were unclear or difficult to place. The software shortly finds the correct spots automatically and only needs a confirmation. There was a large offset between the horizontal grid and the manually flown images parallel to the wall. Once all GCPs marked, the georeferencing from the drone is unactivated and the model updated with the GCP coordinates. Finally, the alignment was optimized once more, and some markers with a high error were replaced manually. This resulted in a low error value as seen in Fig. 28.

Markers	Longitude	Latitude	Altitude (m)	Accuracy (m)	Error (m)
<input type="checkbox"/>	GCP2	13.398426	68.160674	8.811000	0.005000
<input type="checkbox"/>	GCP2	13.398426	68.160674	8.811000	0.005000
<input type="checkbox"/>	GCP2	13.398426	68.160674	8.811000	0.005000
<input type="checkbox"/>	GCP3	13.400713	68.160118	9.455000	0.005000
<input type="checkbox"/>	GCP3	13.400713	68.160118	9.455000	0.005000
<input type="checkbox"/>	GCP3	13.400713	68.160118	9.455000	0.005000
<input checked="" type="checkbox"/>	GCP3	13.400713	68.160118	9.455000	0.005000
<input checked="" type="checkbox"/>	GCP3	13.400713	68.160118	9.455000	0.005000
<input type="checkbox"/>	GCP3	13.400713	68.160118	9.455000	0.005000
<input type="checkbox"/>	GCP3	13.400713	68.160118	9.455000	0.005000
<input type="checkbox"/>	GCP3	13.400713	68.160118	9.455000	0.005000
<input type="checkbox"/>	GCP3	13.400713	68.160118	9.455000	0.005000
<input type="checkbox"/>	GCP3	13.400713	68.160118	9.455000	0.005000
<input checked="" type="checkbox"/>	GCP4	13.400770	68.159500	33.354000	0.005000
<input checked="" type="checkbox"/>	GCP4	13.400770	68.159500	33.354000	0.005000
<input type="checkbox"/>	GCP4	13.400770	68.159500	33.354000	0.005000
<input type="checkbox"/>	GCP4	13.400770	68.159500	33.354000	0.005000
<input type="checkbox"/>	GCP4	13.400770	68.159500	33.354000	0.005000
<input checked="" type="checkbox"/>	GCP4	13.400770	68.159500	33.354000	0.005000
<input type="checkbox"/>	GCP4	13.400770	68.159500	33.354000	0.005000
<input type="checkbox"/>	GCP4	13.400770	68.159500	33.354000	0.005000
<input checked="" type="checkbox"/>	GCP4	13.400770	68.159500	33.354000	0.005000
<input type="checkbox"/>	GCP4	13.400770	68.159500	33.354000	0.005000
<input type="checkbox"/>	GCP5	13.397362	68.160301	46.380000	0.005000
<input type="checkbox"/>	GCP5	13.397362	68.160301	46.380000	0.005000
<input type="checkbox"/>	GCP5	13.397362	68.160301	46.380000	0.005000
<input type="checkbox"/>	GCP5	13.397362	68.160301	46.380000	0.005000
<input checked="" type="checkbox"/>	GCP5	13.397362	68.160301	46.380000	0.005000

Fig. 28 GCPs are here used as coordinate reference for alignment of the cameras. The errors between the cameras and object is in cm.

The sparse cloud was cleaned manually for white points or points that were out of place. The quality was set to “high” and filtering “aggressive”. The final model was left with 1206 images and 2,7 million points.

Sparse cloud was duplicated into three chunks, and the processing region box defines three regions to be run in one batch process for building the dense cloud. Agisoft uses the GPU of the computer to build the dense cloud, but only RAM for generating. The software has problems handling photographs with too much overlap, resulting in crash during processing. It is difficult to manually remove photos taken in manual flight and still keep a certain amount

of overlap, and it is recommended to fly in a preprogrammed app such as Pix4d to ensure the overlap stays stable.

The final model had a ground resolution of 7,67 cm/pixel, covering an area of 0.575 km², the ground control points had a total error of 7.73 cm and the resulting DEM 15.3 cm/pix, 3D model have 71.5 million points (Appendix 3). The ortophoto exported from the photogrammetry was light and detailed. For comparison the ortophoto originating from satellite imagery was difficult to use as the relevant face of the mountain was in the shadows. In Fig. 34 the ortophoto is draped over satellite ortophoto.

Texture and mesh were also built in Agisoft and could be used for further analyzing. This have not been necessary for this thesis, but the 3D model was exported as an .obj file subsampled in Cloudcompare to reduce size, and uploaded in Sketchfab for viewing:

https://sketchfab.com/models/3c8d2091059e4eb39950095d1b265871?fbclid=IwAR3AiWr0Iix5run_XNc5xwK4dK-JPWeaMRB3XUiYr8pxdgZ8FUX5L_XaPOs

4.6 Dips, structural and kinematic analysis

The kinematic analyses done in a stereographic projection visualizes whether any discontinuity sets at a site has a potential failure zone, taking into account the dip and direction of the slope, and the friction angle, but doesn't say anything about other factors that reduce the original strength of the rock mass such as joint fillings, roots or water pressure (Aksoy & Ercanoglu, 2007; Barton et al., 1974; Hoek & Brown, 1997; Wyllie, 2014)

To analyze the data from GeoID, Fieldmove Clino, handheld compass and Coltop3D, the software Dips 7.0 (Terranum) were used. Settings in Dips were lower hemisphere, equal area,

and friction angle 27° . The friction angle was estimated at a conservative and intermediate angle for gneiss and granite (Barton et al., 1974; Wyllie & Mah, 2004). Lateral limits were set at 20° for planar and toppling failure, and none for wedge sliding (Goodman, 1989; Wyllie & Mah, 2004).

4.7 Semi-automated structural analysis with Coltop3D

Coltop 3D uses DEMs and point clouds to provide data for structural analysis. It identifies dip and dip direction for each point and gives it a color from the Hue Saturation Index (HSI) Fig. 29, similar to a stereonet (Jaboyedoff et al., 2007; Metzger et al., 2009). The colors visualize structures in the 3D point cloud such as discontinuities and joints and makes it easy to identify both large systems and more detailed geometries of discontinuities. From the software it is possible to extract data to be used in other software such as Dips 7.0.

Using the point cloud processed in Agisoft it is possible to sample structural data from the source area at Slettind. The point cloud was exported as `ascii.txt` directly from Agisoft with a ground resolution of 7.67 cm/pixel. The following settings were used: 1) x, y, z coordinates and signal strength (RGB), 2) pyramid (0.25-0.5), 3) normal vector computation search radius (0.5 m) and min/max number of points (9/15). Recommended settings were given by Michoud C. (personal communication, 2018).

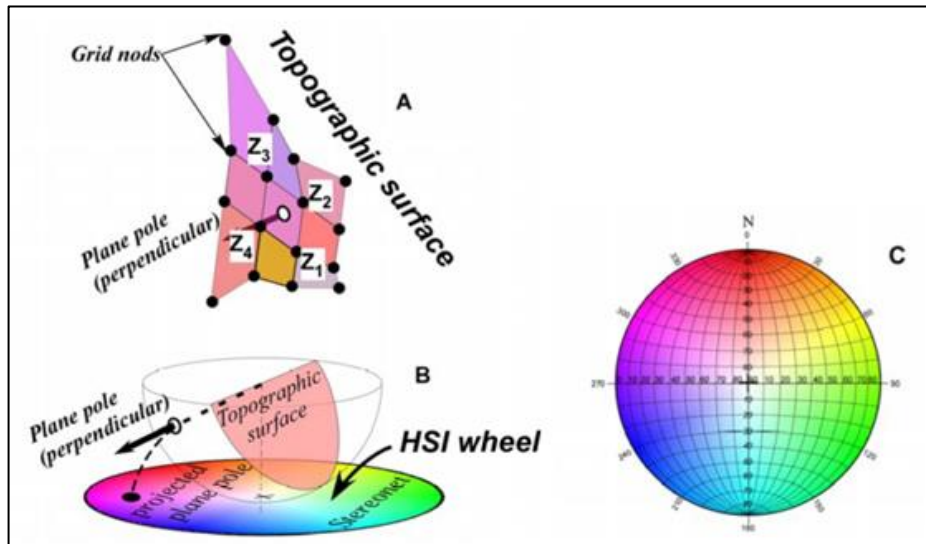


Fig. 29 Illustration of the HSI, A) orientation is determined by using 3-4 points on a grid, B) the relation between a stereographic projection on the HSI wheel, C) the unique colors of the HSI on a stereonet. Retrieved from Jaboyedoff et al. (2007)

The dominating colors of Slettind were identified, and a more detailed analyze was done on each joint set. The size of the data returned varied on the size of polygon but returned between 20 000-500 000 dip/dip directions which is too large for Dips 7.0 to handle. The data was treated in Microsoft Excel (2016) by the function “random” and a selection of 1000-1200 dip/dip directions were extracted and treated in Dips 7.0 for each polygon.

Coltop3D has difficulties handling such large datasets as the one from Slettind, and a large polygon over multiple joint sets tend to overrepresent the general slope direction instead of individual joint sets. With large datasets small, but significant, joint sets are difficult to detect and identify as larger structures statistically return more points. The software is very useful for areas not accessible and identifies the large structures and joint sets, such that potential unstable areas and volumes can be estimated (Jaboyedoff et al., 2007).

Means for each color was also noted in Coltop3d by the “Selection set mode”. There is a difference in Dips 7.0 compared to Coltop3d of the mean in dip/dipdirection as Dips 7.0 often came out with a steeper dip than expected and also more often with a skewed direction towards NE. This is also based on the expected dip/direction from the colors of the HSI wheel (Fig. 29). In extracting and transferring measurements this way it seems that the general

slopedirection (green color) gets overrepresented and affects especially those slopes that are expected include discontinuities with a flatter. Especially it is true for the low angle planes, and joint set J2 have not been represented with measurements extracted from Coltop3d. It is correctly displayed in the “selection set mode” where areas with the same color are chosen, analyzed and return with a mean (reviewed in chapter 5.10). The small percentage of points used in Dips 7.0 may be one reason for this slight incorrect return of data.

4.8 Identification of potential rockfall areas

Potential release areas are possible to locate by inclination maps (Statens vegvesen, NVE), and analyzing kinematic structural data to find intersecting joint sets, that may be susceptible to failure. By combining this in a semi-automatic 3D analyze program such as Coltop3D rockfall prone areas can be identified.

5 Results

5.1 Introduction

This chapter presents results from desktop study, field observations and data analysis. Firstly, the local geomorphology and geology will be described, including lineaments. Secondly, structural data will be presented including structural orientation data and rock mass evaluation from fieldwork and Coltop3D. Kinematic analysis is used to determine likely failure mechanisms. Lastly, the 3D model is used to highlight the location of critical joints (determined from kinematic analysis) for different failure mechanisms (Fig. 30).

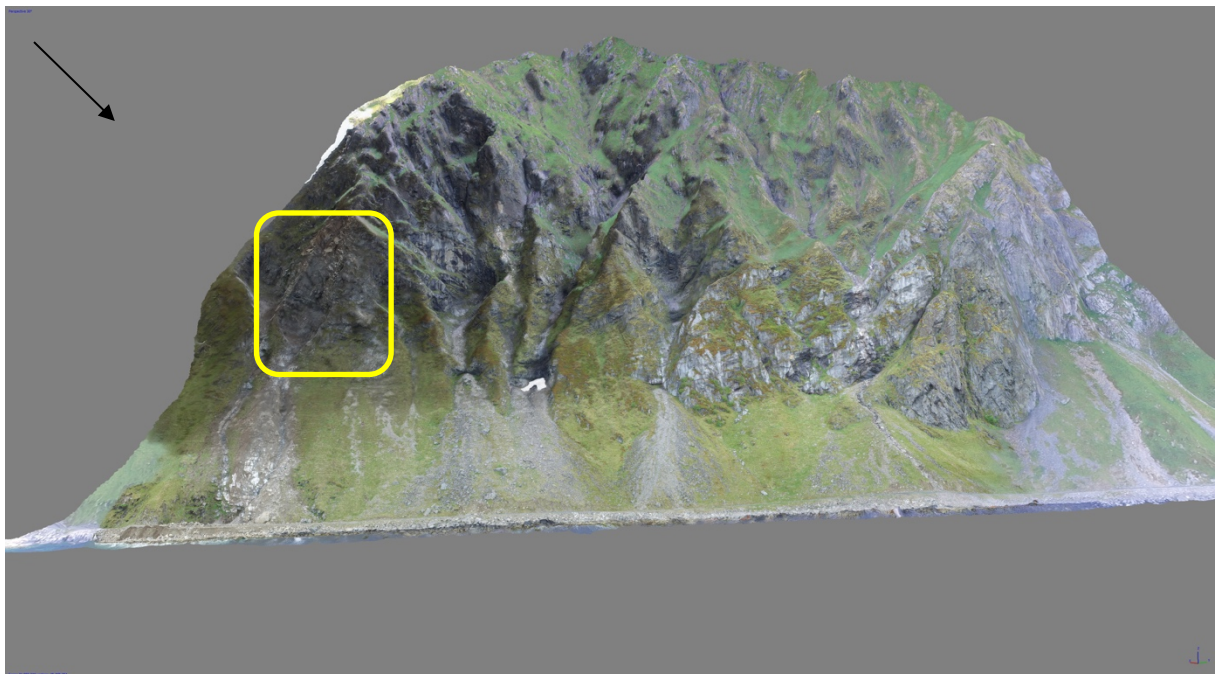


Fig. 30 3Dmodel of Slettind, viewed from NE. Release area within yellow box.

5.2 Geomorphology

5.2.1 Field observations

Slettind (Fig. 30) is a NW-SE striking ridgeline (569 m) with steep (c 60°) slopes dipping to the NE and gentler grassfilled slopes (40°) to SW. The NE-dipping slope is the primary concern of this study. The summit ridge is narrow, and ends towards the south in a smooth, vegetated SSE-facing slope that is steep and continues to sea-level.

The NE-face consists of steep, almost vertical spires of exposed rock down to 200 m. a. s. l. The spires are connected with lower angle grassfilled shelves, ridges and funnels that cease at 350 m. a. s. l. There are five major funnels that reach the bottom of the mountain and end in colluvium fans, and erosion only starts just above the apex of the fans (Fig. 31). Many minor funnels from the summit connects with the larger ones or end above a rockband.

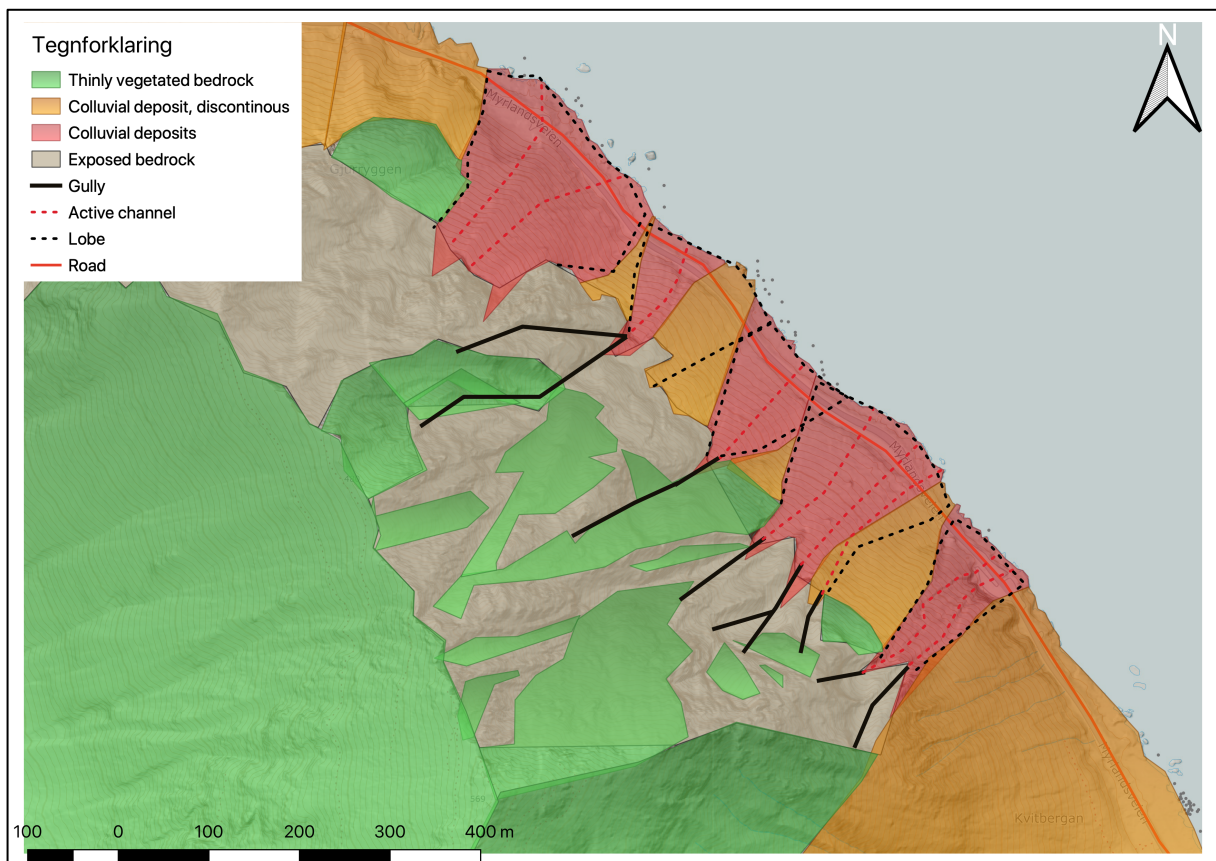


Fig. 31 Geomorphological map of Slettind. The colluvium covered slopes ranges from sea level to 200 m. a. s. l. There is little deposit on the slopes, suggesting that most deposit crosses road and reaches the sea.

The spires and ridges of the NE slope are blocky, and there are no compact rockwall at the site. The joint sets divide the rock into smaller blocks that look like they are balancing on top of each other, and the spires have many minor scars from recent rockfalls. From 350 m. a. s. l. the slope becomes vertical and the vegetated shelves stop. The funnels surpass into successive overhangs of bare rock (Fig. 32), before reaching the colluvium fans.

Below the rockband the ground cover consists of colluvium fans, and thin, discontinuous debris (Fig. 32). The fans are steep (30-40°) and reach to sea level, suggesting that all larger rockfalls or avalanches cross the road and reach the sea. The sizes of these large boulders are from 2x2 to 4x4 m.

The colluvial fans success along the mountain and are at some places difficult to separate. There are clearly defined, eroded, debris channels, but no levees. Most large boulders reach the ocean and are visible in the sea at low tide, and the toe of the colluvium fans are visible under water on aerial photographs. Smaller rocks are dispersed on the slope (Fig. 32) the channels and are sorted, coarsening downwards. The blocks are angular, and somewhat aligned in the falling direction. The fans display layering, suggesting episodic events have formed them.

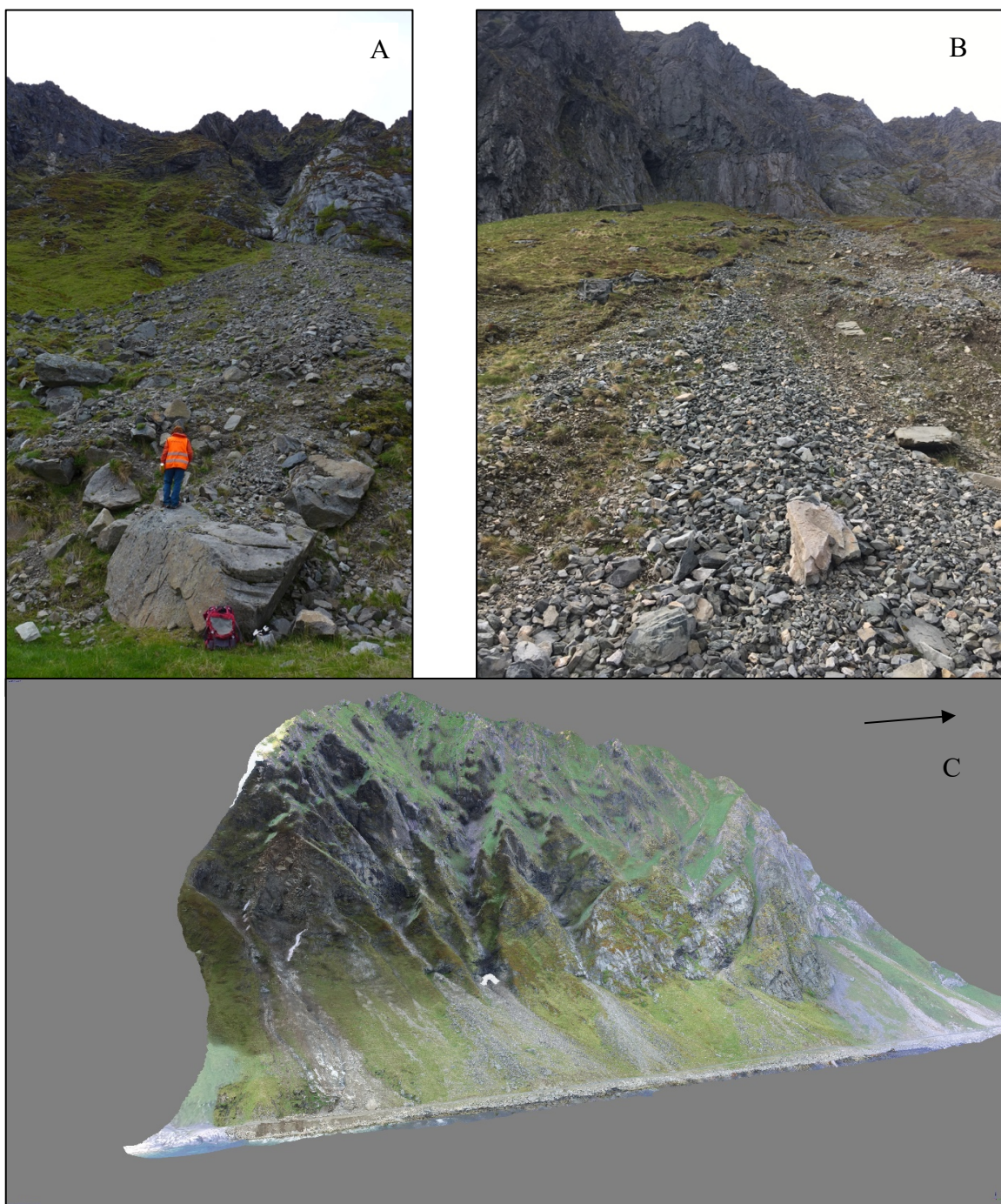


Fig. 32: Photos showing cliff section and various colluvial fans and debris. A) Colluvial fan with thin talus cover below the main bed rock cliff. Fan deposits have internal layering, mostly small rock fragments at the surface, suggesting that larger boulders have travelled further. C) 3D model of the entire hillside slope of Slettind, made from Agisoft. Note the many debris fans along the lower part of the cliff section.

There is little drainage visible from the slope, and only minor streams from a couple of the funnels during fieldwork. The erosion in the funnels suggests that the streams are larger during snowmelt and reduced once the snow has melted. There is outflow and seepage from the rock at many locations but not enough to create drainage channels.

5.3 Bedrock

5.3.1 Lithology observations

The bed rocks in the study area are composed of various types of magmatic and metamorphic rocks, including monzonitic and granitoid gneisses and mangerites (Tveten, 1978). The gneisses have a weak ductile foliation which is gently dipping to the SW whereas the mangerites are generally massive and non-foliated. Representative bed rock samples were taken and used for further petrographic analyses (Fig. 21). The samples include granitic gneiss, monzonites, and schists.

Tveten (1978) mapped the area as mainly monzonite gneiss with fine-grained gneiss around the source area (Fig. 6). The hand samples have been examined and discussed with S. Bergh (personal communication, 2018).

The bed rock sample collected at location 1 is a granitic gneiss. The rock is fine grained with smooth surface and weakly foliated made of alternating quartz, feldspar and minor biotite (light-colored) and layers of amphibole and/or chlorite (dark color). The second sample at this location has a higher feldspar content and is slightly lighter in color.

The hand sample from location 2 is a fine-grained, well-foliated and/or banded quartz-feldspatic schist probably, meta-sedimentary in origin. It is quartz-rich with some minor hornblende and biotite. The surface is smooth but with little secondary stains.

At location 3 the hand sample is dark-colored, massive igneous rock with amphibole and minor pyroxene, possibly a mangerite or monzonitic gneiss, with a large amphibole content, uniformly distributed and randomly oriented mineral grains.

The 3D model shows a change in lithology with a lighter colored bedrock splitting the monzonite in a ductile manner (Fig. 32) and diminishing in the middle of the slope. The rock differs from the surroundings both in color and structure, as it is less broken and show less of the characteristic ridges and spires.

This is not consistent with the bedrock map from NGU (Tveten, 1978) that suggests monzonite gneiss at location 2, 3 and 4. Based on observations from handsamples and 3D model the following bedrock map is proposed (Fig. 33). There is an uncertainty of bedrock type on the southwestern side of the mountain, as there have been no fieldwork here.

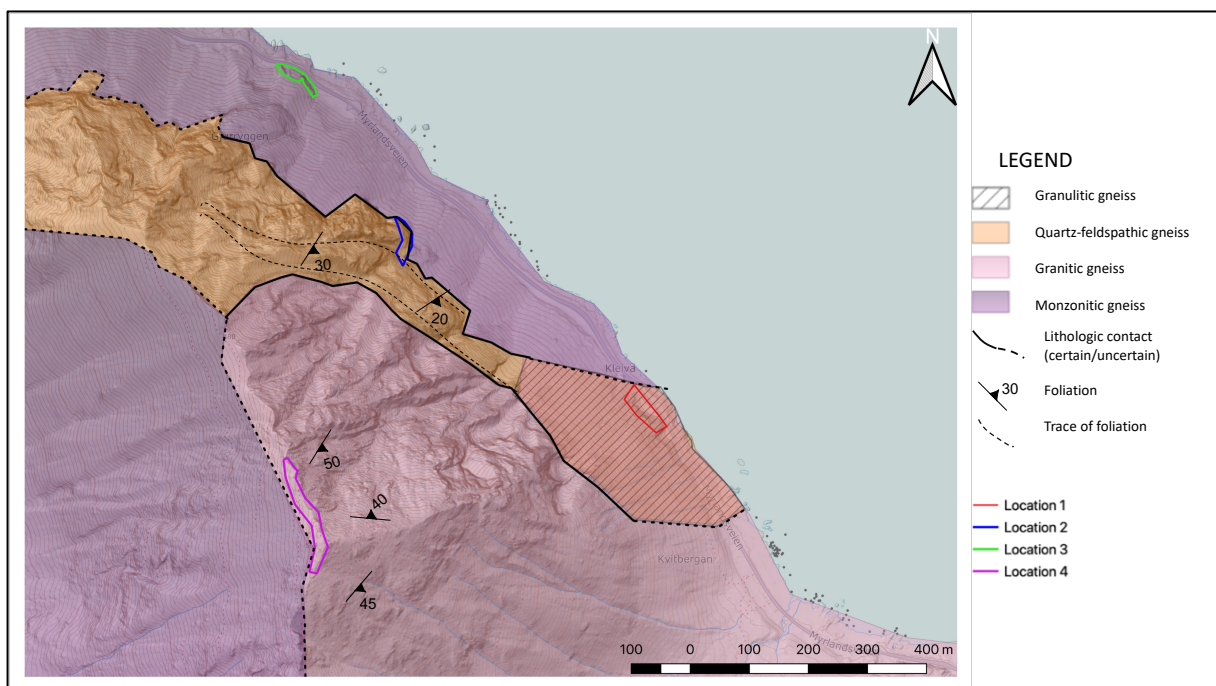


Fig. 33 Bed rock map of Slettind, showing the main lithologies, foliation and contacts. Note that the unit of meta-psammitic schists and its contacts are parallel to the weak foliation and intercalated with the monzonitic gneisses.

5.3.2 Tectonic lineaments at Slettind

Tectonic lineaments in the bed rocks of Slettfjellet were identified using the ortophoto and 3D model from the SfM processing. Three lineament sets are identified and marked J1-J3 in Fig. 34.

J1) A set of brittle fractures that strike variably, NNE to SSW, and dip steeply to the SE, locally following the main attitude of the gneiss foliation and lithological contacts/units (formations). These structures are parallel to the SE-face of the mountain that interrupts the source area (2011/17). They curve slightly in the northern part of the mountain likely due to ductile folding of the gneisses (see below).

J2) A set of WNW-ESE striking, steep lineament follows N-dipping ravines/gullies. These are larger and more dominant in the southern part of the mountain (FIGURE). The J1-J2 lineaments when cross-cutting each other, create a zig-zag geometric pattern at the ridge (Fig. 34) and the triangular large-scale structures in FIGURE.

J3) The third lineament is difficult to recognize in the ortophoto, but it is NW-SE trending and subparallel to the strike of the foliation in the host rock gneisses, and more or less parallel to the general hillside slope direction. Foliation is not directly identified in the ortophoto, but well outlined in the 3D image.

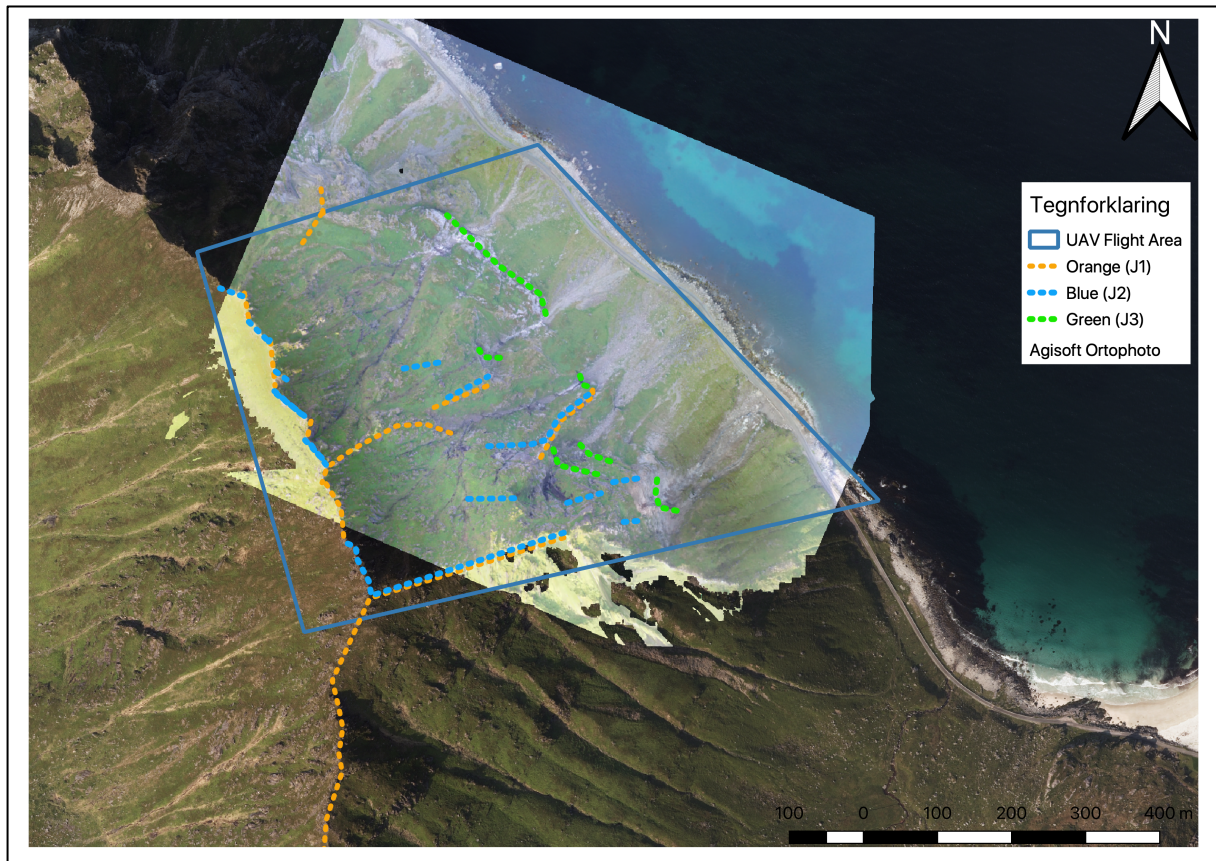


Fig. 34 Orthophoto from Myrland (norgebilder.no) overlaid with the SfM generated image (the area of interest is in the shadow in the orthophoto). This figure shows structural lineaments identified with stipled lines along the strike.

The 3D image of the steep mountain side at Slettind (Fig. 35) displays many detailed structures, and the high resolution of the image makes it easier to identify structural elements and their orientations compared to a 2D-map. The main bed rock foliation of the mangeritic gneisses is well outlined in the image, as alternating benches/layers of felsic and mafic units and dipping gently to the south (left in image). The foliation is parallel to a set of more steeply, south-dipping fractures (J1). In addition, the triangular, or wedge-shaped ravines and gullies, and corresponding ridges shelves aligned parallel to the J1 set, and a second lineament set (J2), are clearly visible. These structures are dominant in the southern and northern parts respectively. The third (J3) lineament set follows the hillside slope direction, and thus, is not well seen.

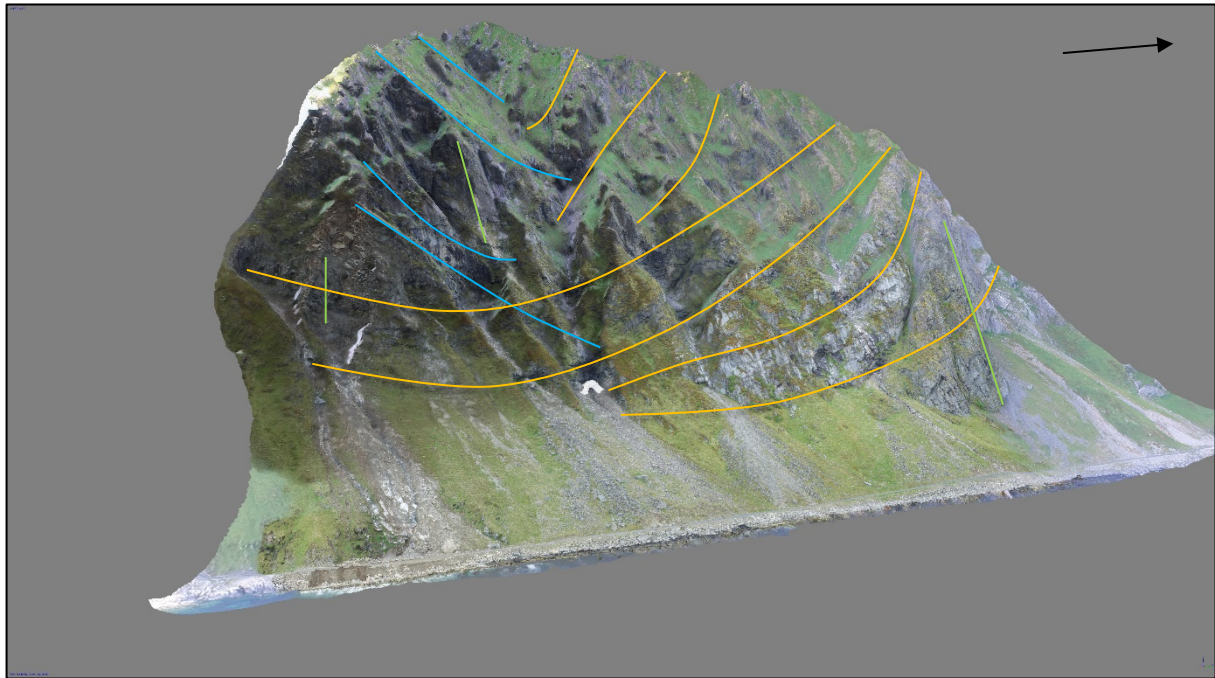


Fig. 35 Main structures marked (lines follow the dip of the structures) with orange, a steep north-south dipping feature, and blue, a low-angle north-dipping structure. Green marks the steeply dipping slope parallel lineament.

The south dipping (J1) lineament is parallel to the main ductile foliation of the bed rock gneisses, which is thought to be Palaeoproterozoic in age (Corfu, 2004). Its orientation, however, at least locally, overlap with the first brittle fracture set observed (J1), which is again parallel to main faults (and fractures) that bound the Lofoten Ridge termed S2 by Bergh et al. (2007).

The second set of lineaments (J2), strikes NNE-SSW, and it is present not only in Slettind, but along fjords and major valleys between the different Lofoten islands. This lineament set is related to the Permo-Jurassic rifting/extension event along the Lofoten margin with extension in a W-E direction (Bergh et al. 2007; Hansen et al. 2012). This lineament (termed S1) has been mapped just south of Slettind where it is parallel to Nappstraumen and similarly oriented fjords in westernmost Lofoten. (Fig. 5)

The third lineament (J3) that trends NW-SE along the mountain side of Slettind, can be explained as related to the late Cretaceous to Paleogene rifting event of the Lofoten margin (termed S3) (Bergh et al. 2007). This event was linked to the transform movement along the

Hornsund-DeGeer fault system near the Barents Sea margin, with extension in a NNW-SSE to NNE-SSW direction, creating normal faults and fracture sets dipping NE and SW, and subsidiary NW-SE trending strike-slip faults (Eig & Bergh, 2011).

On a closer view at the 3D model (Fig. 36) the outline of the three different lineament sets are visible. In particular, the orientation of the first and second lineament sets (J1-J2), when they interact in outcrop, creates wedge-shaped structures.

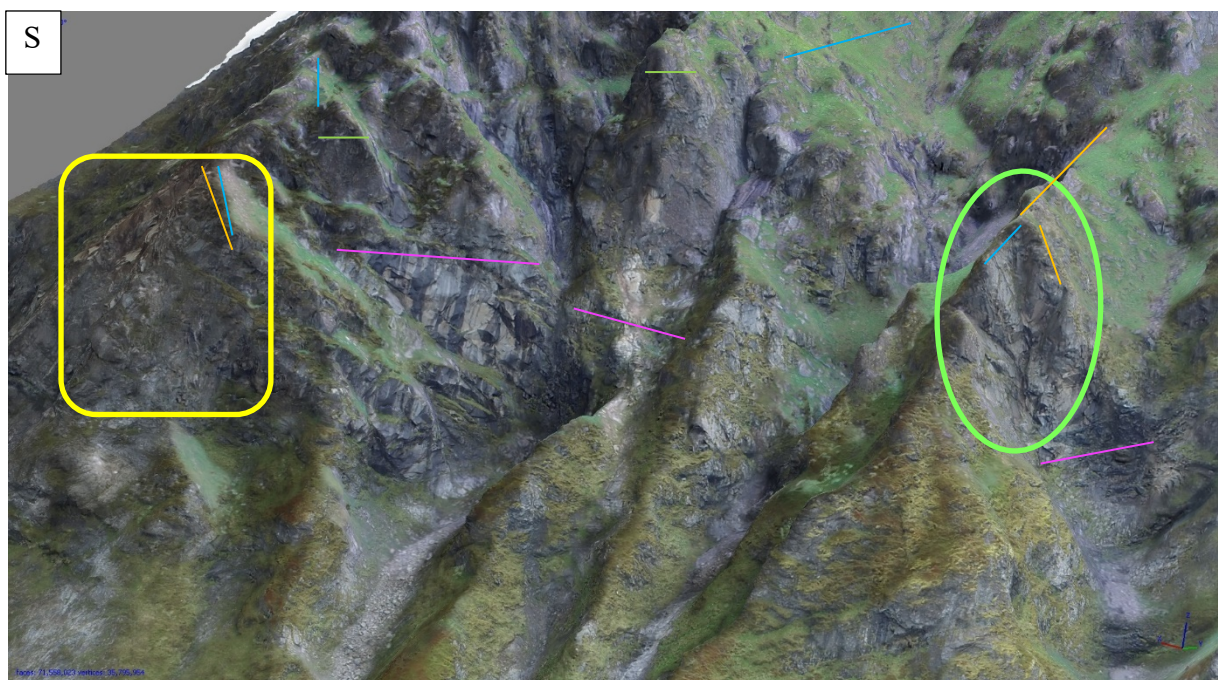


Fig. 36 Detail map view from NE, outline of the 3D image in fig. 35 showing the source area of 2011/17 within the yellow box, and main structures marked by green, orange and blue lines following the strike. Foliation is marked in purple. The green circle marks a defined triangular shape.

5.3.3 Structural observations from the field

The main bed rock foliation of the gneisses, and the three sets of presumed brittle fractures/joints (discontinuities) were mapped in more detail at Slettind, at four outcrops that were accessible in the field, Location 1, 2, 3 and 4. (Fig. 37). Location 1, further divided into 1a and 1b, is located directly below the release area from the major 2011 and 2017 rock avalanches. The two outcrops are 50 meters apart. Location 2 is situated further north, at the

top of the colluvium fans. Location 3 is another outcrop close to the road north of the UAV flight investigation site. Location 4 is situated at the summit ridge (Fig 37).

The field observations are presented for each location with bedrock type, rock mass quality (Q values and GSI), and structural orientation data, and for comparison a summary is presented at the end.

Structural orientation data are displayed in stereographic projections made in Dips 7.0, in northern hemisphere, equal area projection with poles surrounded by 1σ deviation. Structural orientation data made with different tools (handheld compass, GeoID and Clino Fieldmove) has been compared, showing negligible variation (Appendix 2).

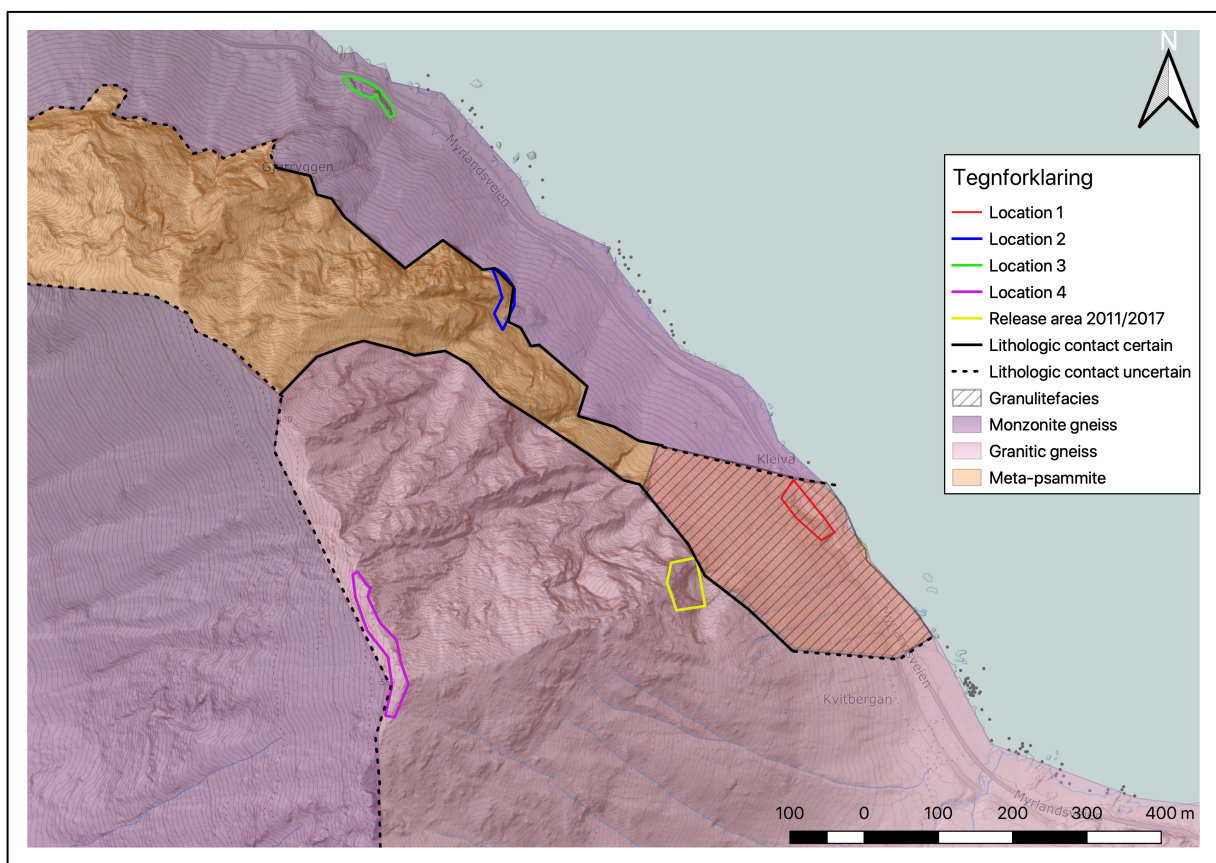


Fig. 37 Topographic map of Slettind with bed rock geology, showing the studied localities 1-4. The release area of the rock avalanches (yellow polygon), and the four outcrop locations are shown. Map also shows proposed geology from chapter 5.3.1

5.4 Location 1a

The roadcut is six meters high and surrounded by a thin layer of soil on talus from the rockfall and avalanches. Location 1.a is a roadcut that has been affected by blasting and 1.b is bedrock exposed by the regular rockfalls (Fig. 38 and 39).



Fig. 38 Picture showing an overview of the first outcrops. Location 1.a is within the red box and location 1.b within yellow box. Joint sets J1, J3 and J2 are visible in the picture. Picture taken with the UAV

5.4.1 Rock mass quality

The rock is a mafic granitic gneiss, medium grained, dark colored, poorly banded with amphibolite minerals like amphibole and pyroxene, and slightly weathered, thus yielding a high competence or strength. The foliation strikes WNW-ESE and dips moderately to the WSW, i.e. inwards (56/211). There is no obvious sign of scree/fall out material from this host rock ductile fabric. Smooth planar and wedge-shape open joints are present, with surfaces

covered by hematite, epidote stains and occasional slickensides. The fracture frequency is ca. 1 m persistent joints for $<1 m^2$.

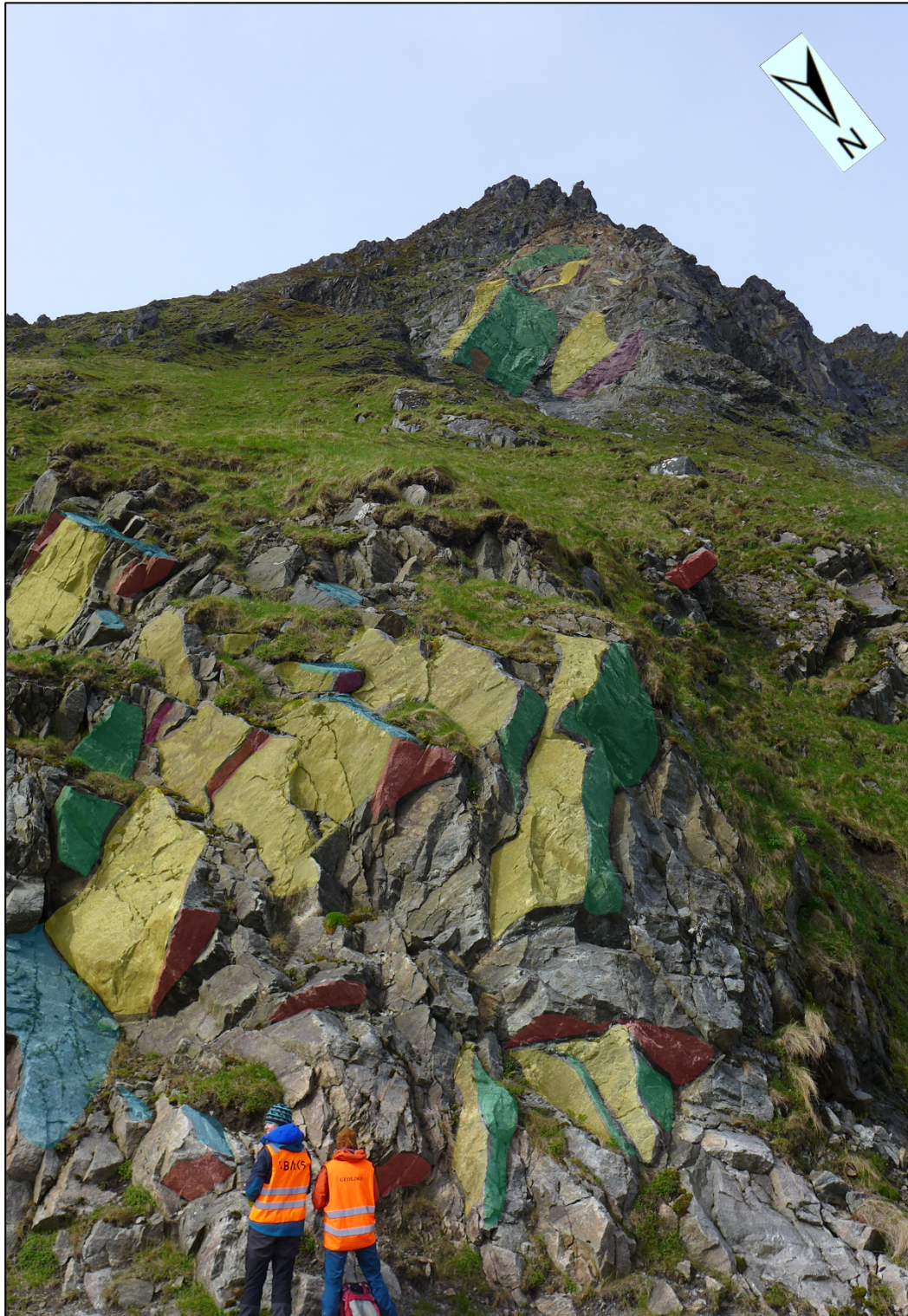


Fig. 39 Outcrop with numerous brittle fracture/joint at location 1, are marked in different colors according to their joint sets. Joint set J1 (yellow) facing towards E, joint J2 (blue) towards NE, joint set J3 (green) towards NE and foliation (red) towards SW. Private picture, 2018.

Three very clear joint surfaces intersect in combination with the foliation plane that dips SW about 60°. The sets have steep dip directions both to the NE and E, whereas the daylighting foliation plane dips SW and creates overhanging surfaces (Fig. 39). The bedrock is prone to toppling, wedge and planar failures with brittle joint fractures and smooth planes (Fig. 40).

5.4.2 Q values and GSI

Q value (Tabell 2) indicates a poor to very poor rock mass, with smooth planes, minor to medium inflow of water, loose open brittle joints with three-four joint sets (8-12/m³). The structure is blocky and disintegrating.

Tabell 2 Q chart location 1a.

RQD	75-90	8-12 joints/m ³
Jn	15-12	Three plus random joints sets
Jr	1-1	Smooth, planar
Ja	1	Surface staining
Jw	0,66-1	Minor-medium inflow
SRF	5-5	Loose open joints
Q estimate	0,66-1,5	Very poor rock

GSI value was estimated to 55 with the following characteristics:

Blocky/disturbed, folded with angular blocks formed by many intersecting discontinuity sets. Persistence of bedding plane or schistosity. Poor, slickensided highly weathered surfaces with compact coatings or fillings or angular fragments.

Both Q values and GSI result in corresponding values representing to poor rock quality.



Fig. 40 Outcrop photo of mangeritic gneiss showing several brittle discontinuity surfaces, J1 (yellow) and J2 (blue). The J1 surfaces are clearly defined as steeply dipping sets, whereas J2 surfaces are low-angle and gently N-dipping. Note that smooth J1 surfaces are coated with hematite and epidote. When the two fracture sets interact, or cross-cut each other, they define triangular scarps (wedge) that are prone to wedge failure. The foliation is weak and less visible with no related fractures developed.

5.5 Location 1.b

Location 1.b is situated in the run-out zone below the rock avalanches (Fig. 41). The base of the outcrop has been cleared of debris by machines but not affected by blasting. There is a mylonitic shear zone visible that splits the outcrop in two. It is free from vegetation due to the regular rockfalls and a minor water stream coming down the middle.



Fig. 41 Outcrop 1.b looking up towards the source area. Yellow surfaces are the steep north-south striking planes of J1, blue J2, green J3, and red the foliation. Dotted lines show joint sets of J2. From location 1.2 the source area 2011/17 and surfaces are easily identified and comparable.

5.5.1 Rock mass quality

The bedrock is mafic granitic gneiss, medium grained, dark, poorly banded, felspar rich with amphibolite minerals and slightly weathered, high strength. Foliation is dipping inwards, and the outcrop has no clear failure along its structures.

Smooth planar and wedge structured joints, with hematite, epidote stains and occasional slickensides. The fracture frequency is ca. 1 m persistent joints for $<1 m^2$.

The large rock from 2011 lies against the slope (Fig. 19) and an attempt of removing it revealed that it stabilized the talus slope above. It has been left there to stabilize the foot of the slope, preventing it from creeping downwards.

Three joint sets and foliation is intersecting creating brittle fractures that is clearly visible with smooth joint planes. Dip direction is low angle northeast, steep south west and steep south east (Fig. 41).

5.5.2 Q values and GSI

Less joints per m² and less joint sets than location 1 were observed. Smooth and surface stained planes with dry or minor inflows can be documented (Tabell 3). The competent rock that seems less brittle compared to location 1, that has been affected by blasting.

Tabell 3 Q chart for location 1b.

RQD	90-100	Excellent 0-7 joints/m ³
Jn	12-6	2-3 joint sets+ random
Jr	1	Smooth, planar
Ja	1	Unaltered, surface staining
Jw	1	Dry or minor inflow
SRF	7,5	Multiple shear zones, within competent rock
Q value	1-2,2	Poor rock quality

The GSI was estimated to 65 with following characteristics:

Structure: Very blocky, interlocked, partially disturbed mass with multi-faceted angular blocks formed by 4 joint sets or more. Surface: Fair, smooth, moderately weathered and altered surfaces.

The values indicated have slightly better strength index compared to 1.a, and the result may be due to the undisturbed rock from human interference.

5.5.3 Structural orientation data 1.a and 1. b

The stereonet plotted contains 188 measurements from both Location 1a and 1b and has a very clearly defined N-S going joint set which is vertical (Fig. 42). A low angle J2 and the overhanging structures from foliation is also found. The joint set called J3 is less prominent.

J2 is a low angle plane that normally would be too low for a sliding plane (normally $>45^\circ$). The joint system creates a blocky structure with smooth planes, especially J1 where the planes seem to have particular low friction and abundant secondary epidote and hematite stains. This gives low Q values, although the GSI value mostly reflects the blocky structure created. The

amphibolite facies contribute to weak zones, and as it is following the foliation in the gneiss, a fourth weak discontinuity factor affects the structure.

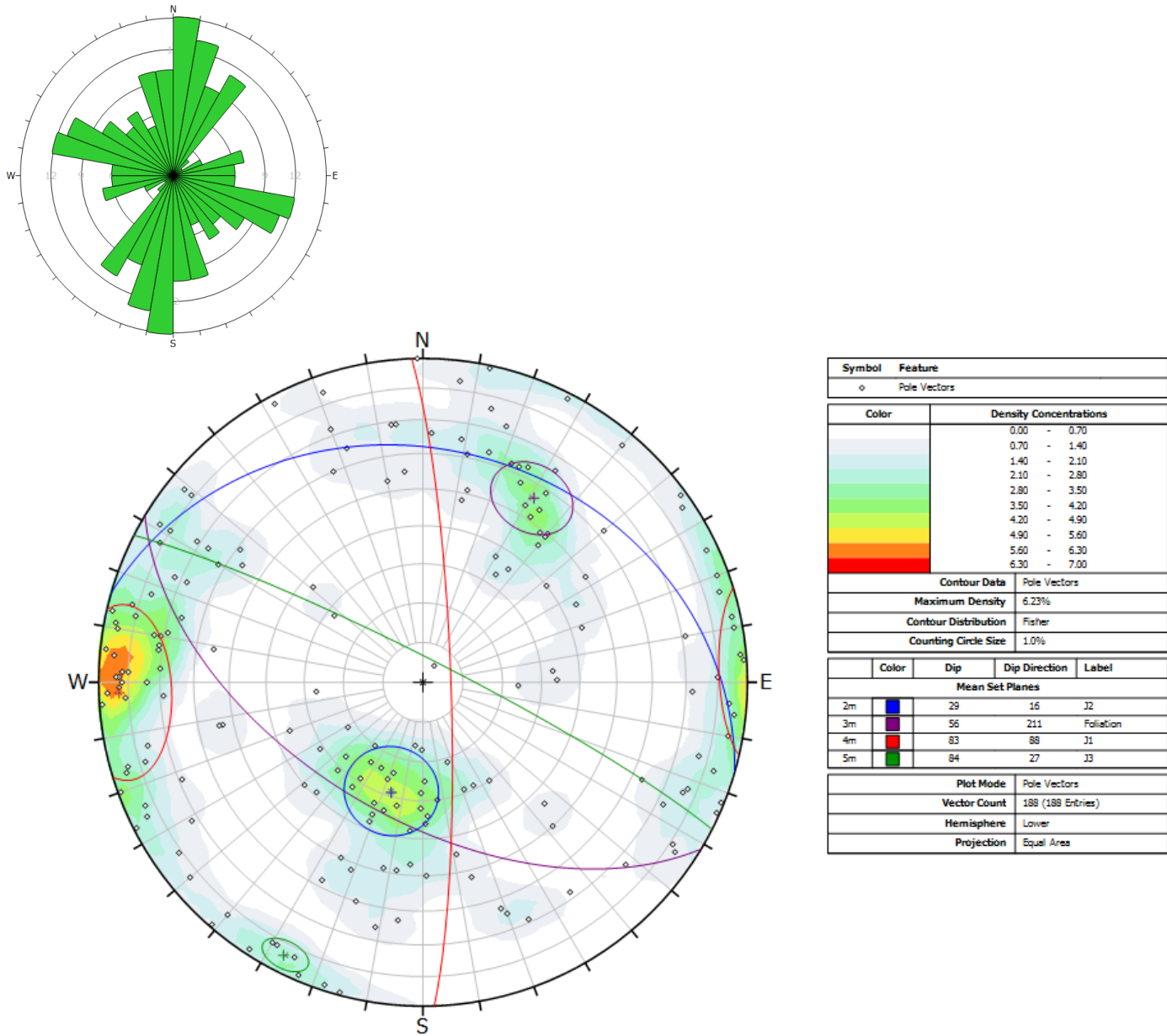


Fig. 42 Rosette diagram and stereonet at location 1 a and b. The most dominant joint set is the N-S striking J1 and the low-angle N facing J2. Foliation is less dominant and J3 has very few measurements. Rosette diagram show two major joint set directions.

There are three defined joint/fracture systems in location 1.a and 1. b:

Joint set	Dip/dip direction	Color
J1	83/083 \pm 5°	Red
J2	29/016 \pm 10°	Blue
J3	84/027 \pm 5°	Green
Foliation	56/211 \pm 5°	Violet

5.6 Location 2

Location 2 was the only rock above the talus that was accessible and safe to attend for structural orientation data. The rock had different structure and color, compared to the lower outcrops and was undisturbed from human factors. A clearly defined change in lithology follows the north-south striking lineaments in a ductile manner (Fig. 43).

5.6.1 Rock mass quality

The bedrock is a meta-psammitic quartz-feldspatic schist, uniformly distributed and slightly layered, fine grained with hornblende, light grey of color. Slightly weathered, and with high strength. Foliation dips steeply inwards and very few failures are found. The slope faces north-east and smooth planar joints are prone to toppling, blocky, well interlocked, cubical blocks with a fracture frequency c. 1 m persistent for $>2 m^2$. Three intersecting discontinuity sets were documented.



Fig. 43 Outcrop photo of the steep mountain side of Slettind, with close-up view of location 2 (see fig. 44). The light-colored meta-psammitic schists/gneisses have well-defined composite foliation dipping gently to the SW (left in photo) and is apparently folded by open folds yielding variable dips (and strike directions). Brittle J2-fractures/joints (red-colored stippled lines) are low- to moderate angle and subparallel to the gneiss foliation. Red dotted lines follows the N-S striking joint set J1, that here changes slightly in dip. Blue dotted lines follow the low angle north dipping J2 and green areas represents the planes of J3. Photo taken with UAV.

5.6.2 Q values and GSI

Three intersecting joint/fracture sets with smooth and planar structure. Dry excavations, and surface stained erosion on planes. Gives a quite high Q value for the area (Tabell 4).

Tabell 4 Q chart location 2

RQD	90-100	0-7 joints/ m^3
Jn	9	3 joint sets
Jr	1-2	Smooth, planar
Ja	1	Unaltered, surface stained
Jw	1	Dry excavations
SRF	5	Loose, open joints
Q estimate	2-4,4	Poor rock quality

GSI was estimated to 75, the highest level we found at Slettind.

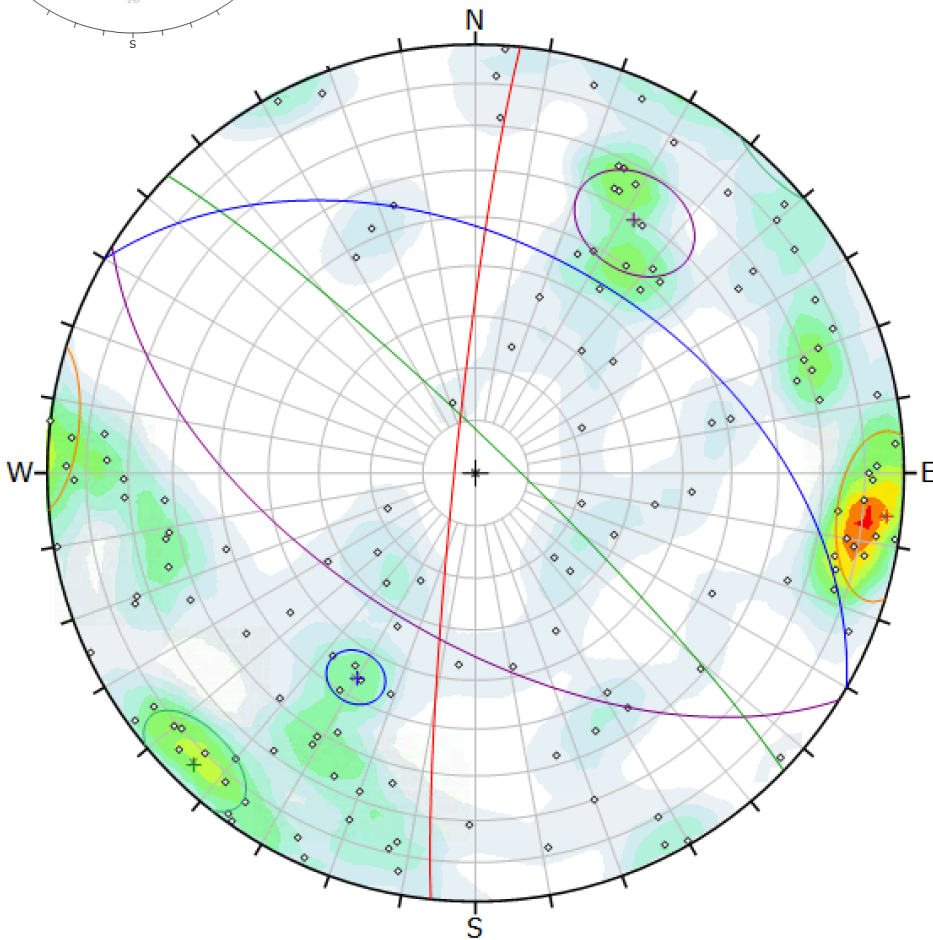
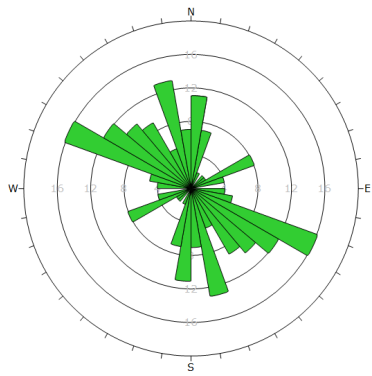
Blocky, well interlocked undisturbed rock mass consisting of cubical blocks formed by three intersecting discontinuity sets. Fair, smooth, moderately weathered and altered surfaces.



Fig. 44 Folds and fold hinges were found high near a larger weak structure. The overhanging joints follows the foliation orientation.

5.6.3 Structural orientation data

In total 140 separate fracture/joints (J1-J3) (Fig. 45) were identified and the orientation measured as strike and dip, using Geo ID and Clino Fieldmove were done and plotted in stereonet in Dips 7.0. The data show three main orientations, including one steep set striking N-S (J1), and two sets alternating NW-SE strikes and NE and SW-dips (J2-J3), which is almost perpendicular to the former. These orientations are similar to those observed at the other locations, but deviate by being slightly more west dipping, in addition to a steeper dip of the J2-set, and the gentler dip (10) of the foliation.



Symbol	Feature
◊	Pole Vectors

Color	Density Concentrations
	0.00 - 0.65
	0.65 - 1.30
	1.30 - 1.95
	1.95 - 2.60
	2.60 - 3.25
	3.25 - 3.90
	3.90 - 4.55
	4.55 - 5.20
	5.20 - 5.85
	5.85 - 6.50

Contour Data	Pole Vectors
Maximum Density	6.04%
Contour Distribution	Fisher
Counting Circle Size	1.0%

	Color	Dip	Dip Direction	Label
Mean Set Planes				
1m	■	86	276	J1
2m	■	59	212	Foliation
3m	■	84	44	J3
4m	■	46	30	J2

Plot Mode	Pole Vectors
Vector Count	140 (140 Entries)
Hemisphere	Lower
Projection	Equal Area

Fig. 45 Rosette diagram and stereonet at location 2. The dominating J1 is dipping slightly towards west (towards slope). J2, J3 and foliation is rotated towards east, compared to location 1. Rosette diagram shows dominating joint sets of NW-SE.

Joint set	Dip/dip direction	Color
J1	86/276 $\pm 5^\circ$	Red
J2	46/030 $\pm 15^\circ$	Blue
J3	84/044 $\pm 10^\circ$	Green
Foliation	46/212 $\pm 10^\circ$	Violet

The GSI value is quite high with less joints per square meter resulting in a more massive rock. The planes are smooth and the joints loose, which still gives a low Q value (poor rock quality).

5.7 Location 3

There were no other outcrops (Fig. 46) close to the road but until the northern part of the mountain, outside of the UAV flight area (Fig. 34, 37). This outcrop lies within the monzonitic gneiss-region and the outcrop has been subject to blasting due to roadwork.



Fig. 46 Location 3, north of the UAV flight inspection area. The bedrock is weakly foliated and rather dominated by brittle fractures/joints. Surfaces are smooth and stained with epidote growth. Low-angle sliding plane (J2, blue) indicates planar failure. N-S striking joint set (J1) is colored with yellow and is the most dominating one. J3 (green) occurs occasionally. Foliation (red) are overhanging structures mostly seen higher in the bedrock. Location has been subjected to blasting.

5.7.1 Bedrock descriptions

The rock is a monzonite gneiss, homogenous tabular grained, uniformly distributed and randomly oriented hornblende-rich, dark, minor ductile deformation bands, quartz veins and amphibolite facies (Fig. 46). The rock is slightly weathered and has a high strength. Foliation

dips steeply inwards with no prominent failure along it. The north-east facing outcrop shows smooth planar joints, with secondary compact coating fillings of chlorite and epidote growth and slickensides (Fig. 47). The fracture frequency is ca 1 m persistent for $<1 m^2$, with a brittle block structure.

The monzonite gneiss is a bit younger than the metasupracrustal rocks and is 1700-1900 million years old.

5.7.2 Q value and GSI

The bedrock has slickensides, very low friction, with a lot of secondary epidote and hematite stains. Clearly defined joint sets with larger blocks are documented (Tabell 5).

Tabell 5 Q chart location 3

RQD	75-90	Good 8-12 joints/ m^3
Jn	12	3 joint sets+ random
Jr	0,5	Slickensided, planar
Ja	2	Slightly altered walls
Jw	0,66-1	Dry-medium inflow
SRF	5-2,5	Single weak zones-loose open joints
Q value	0,206-0,75	Very poor

GSI was estimated to 45, which is the lowest of all locations.

The rock mass is disintegrated poorly interlocked, heavily broken rock mass with mixture of angular and rounded rock pieces. Poor, slickensided, highly weathered surfaces with compact coatings or fillings or angular fragments can be seen.

There is evidence of both ductile and brittle fault deformation at the outcrop. Within the low angle daylighting joint set there have been brittle movement between blocks (FIGURE), and a quartz vein is clearly split and displaced (Fig. 46). In Fig. 47 a ductile shearband witness about strain in a NW-SE direction. There is low friction on all planes with a tendency towards planar failure. Some pieces show ductile shear in a E-W direction (Fig. 47).



Fig. 47 Outcrop of location 3 shows surfaces marked with yellow (J1) and blue (J2). Yellow dotted line encircles a N-S striking surface where the greenish color is from epidote stains. Blue dotted lines follows the joints of J2. Note the ductile deformation band below the hammer.

5.7.3 Structural orientation data

322 structural orientation data (Fig. 48) are shown as poles and planes in the stereoplots with two clearly defined sets: N-S striking vertical (J1) and E-W striking steep southwards dipping foliation. In addition there is a E-W striking, low-angle, N dipping plane (J2). These are also clearly seen in the photographs Fig. 46;47. J3 is slightly less represented here.

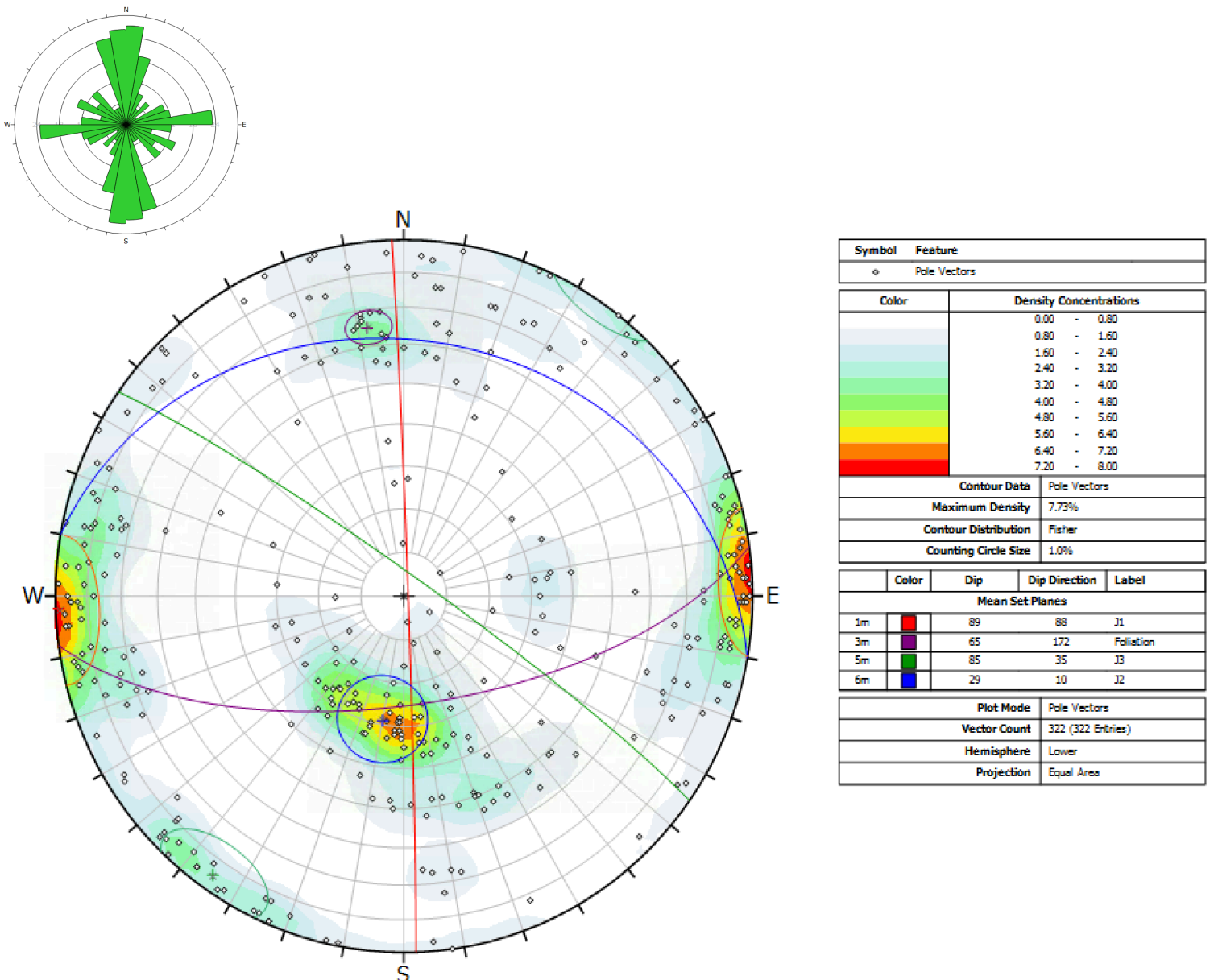


Fig. 48 Stereonet and rosette plot showing structural measurements from location 3. J1 and J2 are the two dominating sets. While J3 is only slightly present. Foliation is rotated towards SE.

Joint set	Dip/dip direction	Color
J1	89/088 ±10°	Red
J2	29/010 ±15°	Blue
J3	85/035 ±5°	Green
Foliation	65/172 ±10°	Violet

J1 is the most dominant joint set at the location and the planar orientation towards the road is undercut by the low angle N dipping J2 (Fig. 48). Slickensides and low joint roughness, in combination with larger water inflow, random joints and single weak zones gives the location a very low Q value. The GSI value is also very low, as the bedrock is blocky and disintegrated in combination with the low friction planes.

5.8 Location 4

The field investigations were done at the summit ridge (Fig. 37), where some sparse outcrops were feasible for measurements. The NE dipping mountainface contained many smaller pieces of rock, but the steep ground made them inaccessible. The rock at the ridge was mostly situated on the southwestern side and all were heavily weathered with rounded joints, interrupted by funnels between straight planes of the rock (Fig. 49).

5.8.1 Bedrock descriptions

The rock is a monzonitic gneiss, medium grained, dark, poorly banded felspar rich with amphibolite facies and moderately weathered, high strength. Foliation is horizontal, slightly dipping northeast. Rounded, planar structured joints in a blocky structure, prone to toppling. The fracture frequency is 1 m persistent joints for <1 m² in the outcrop.

5.8.2 Q values and GSI

Three well defined joint/fracture sets, with smooth planes where newly fractured, heavily eroded with rounded edges. Silty material covers the joints/fractures.

Q chart

RQD	90-100	Excellent 0-7 joints/ m^3
Jn	9	Three joint sets
Jr	1	Smooth, planar
Ja	3	Silty or sandy clay coatings
Jw	1	Medium inflow
SRF	5	Loose open joints
Q value	0,667-0,742	Very poor

GSI was set to 60. Blocky, well interlocked undisturbed rock mass consisting of cubical blocks formed by three intersecting discontinuity sets. Fair, smooth, moderately weathered and altered surfaces.

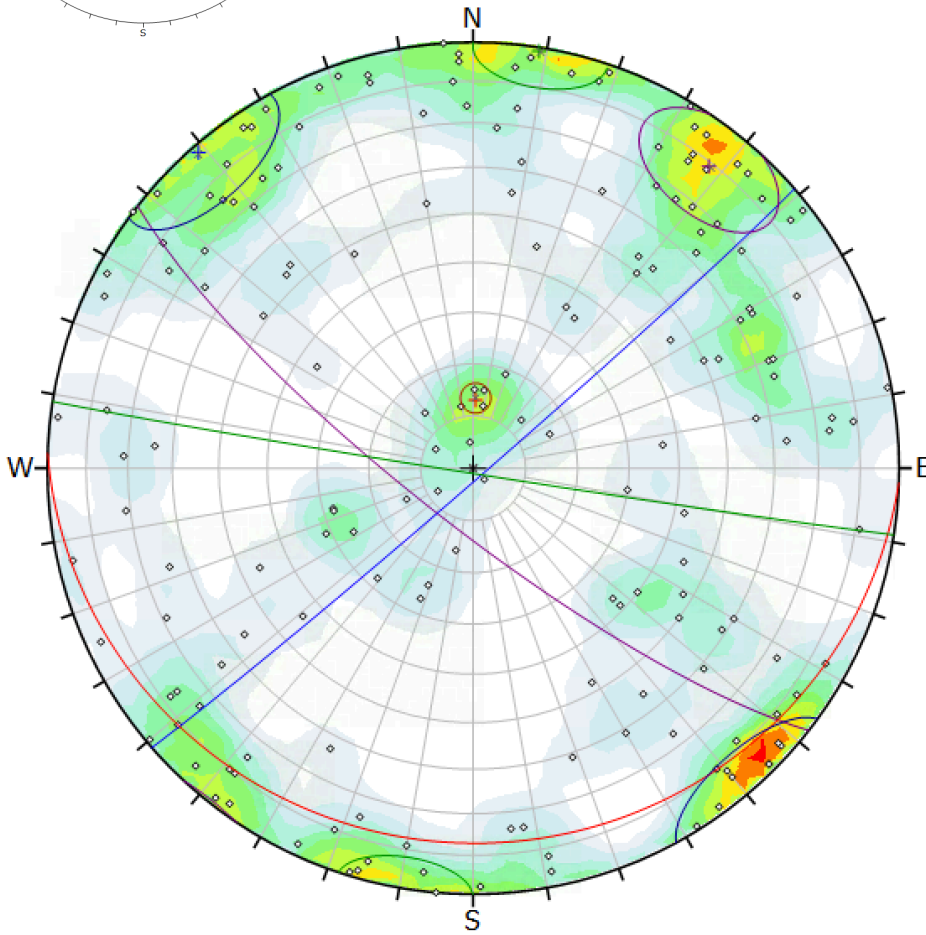
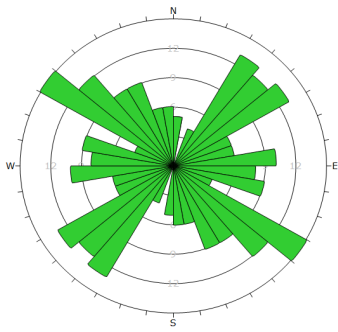


Fig. 49 Pictures from the summit ridge looking southeast. Clean vertical planes along the side of the funnels (marked as a red surface) are split by vertical, evenly distributed NW-SE striking joints and a horizontal joint set (red lines) creating an orthogonal blocky structure.

5.8.3 Structural orientation data

Along the summit ridge 178 measurements were done with Geo ID (Fig. 50). Measurements were performed on both sides of the summit ridge, (NE and SW).

There are two steep, almost vertical joint sets along with foliation, and one horizontal south dipping joint set. The dominant N-S striking joint is not present at the summit ridge. The most prominent joint sets are instead the almost vertical and opposed ones, NE-SW (J1) and steep NW-SE striking foliation. The low-angle S dipping J2 and the steep and slightly south rotated joint set J3 creates a blocky structure.



Symbol	Feature
o	Pole Vectors

Color	Density Concentrations
	0.00 - 0.50
	0.50 - 1.00
	1.00 - 1.50
	1.50 - 2.00
	2.00 - 2.50
	2.50 - 3.00
	3.00 - 3.50
	3.50 - 4.00
	4.00 - 4.50
	4.50 - 5.00

Contour Data	Pole Vectors
Maximum Density	4.66%
Contour Distribution	Fisher
Counting Circle Size	1.0%

	Color	Dip	Dip Direction	Label
Mean Set Planes				
1m		79	218	Foliation
2m		88	139	J1
3m		13	182	J2
4m		89	189	J3

Plot Mode	Pole Vectors
Vector Count	178 (178 Entries)
Hemisphere	Lower
Projection	Equal Area

Fig. 50 Stereoplot and rosette from location 4. The dominating joint sets are here striking NW-SE and NE-SW.

Joint set**Dip/dip direction**

Foliation	Dip/dip direction	Color
J1	79/218 ±5°	Violet
J2	88/139 ±15°	Blue
J3	13/182 ±5°	Red
J4	89/189 ±10°	Green

The Q value is very low, mostly due to heavily eroded rock, silty fillings and open joints. The structure is blocky and there are less blocks per square meter compared to the other locations. The GSI value is therefore quite high (60).

5.9 Structural observations from Coltop3D

In Coltop3D the dominant structures are N facing shelves on the southern part of the mountain, that are interrupted by NE facing steep pillars and overhanging areas of foliation. The release area of the 2011/2017 rock avalanche is the only larger area that is striking N-S and facing E in the southern part (Fig. 51). From summit and northwards the mountain is dominated by SE facing shelves, interrupted by slope parallel steep pillars. Foliation is sparsely represented with an orientation 84/210.

The mean and median orientation from polygons with a specific color (Fig. 52) confirms the dip and dip direction within the given section. When the surfaces are steep, only a slight change in dip direction and/or dip changes the color to the opposite side of HSI wheel, which is the case with joint set J1. Both green/yellow and violet represents the same set.

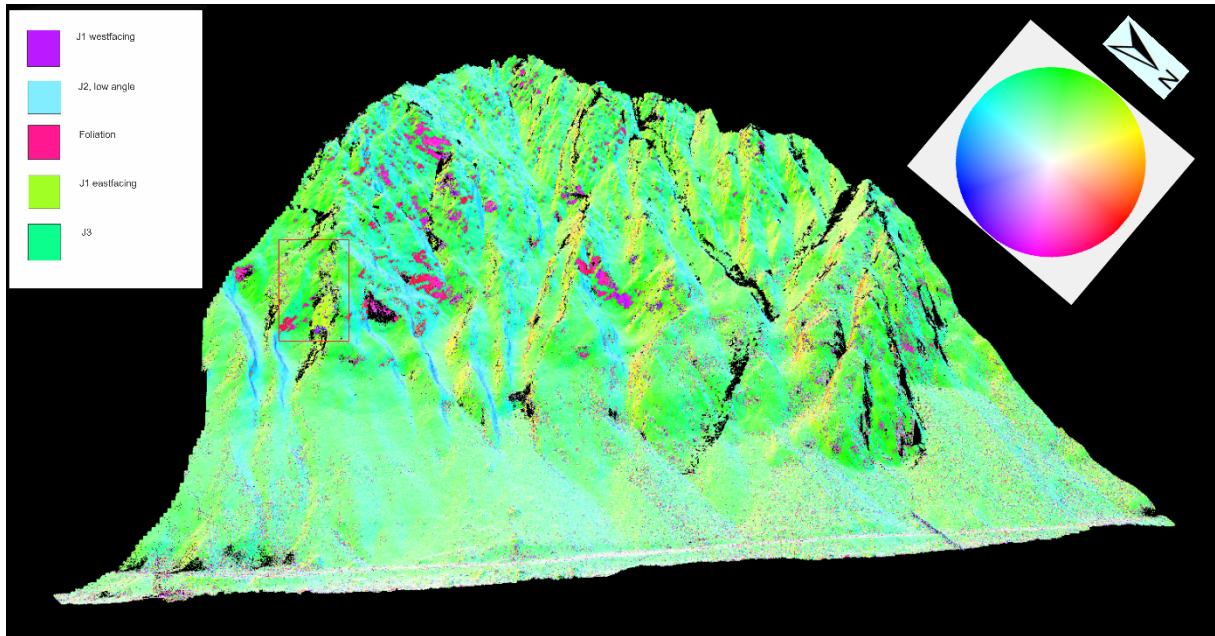


Fig. 51 Overview over Slettind analyzed in Coltop3D. The HSI wheel is rotated in N direction aligned with the image. Red rectangle marks the release area of 2011/17. Joint set J1 (violet and green/yellow) is N-S striking dipping east (green/yellow/orange) and west (violet), J2 is low-angle shelves dipping N. Joint set J3 follows pillars and general slope direction dipping NE. Foliation is represented as small patches (pink) dipping SW.

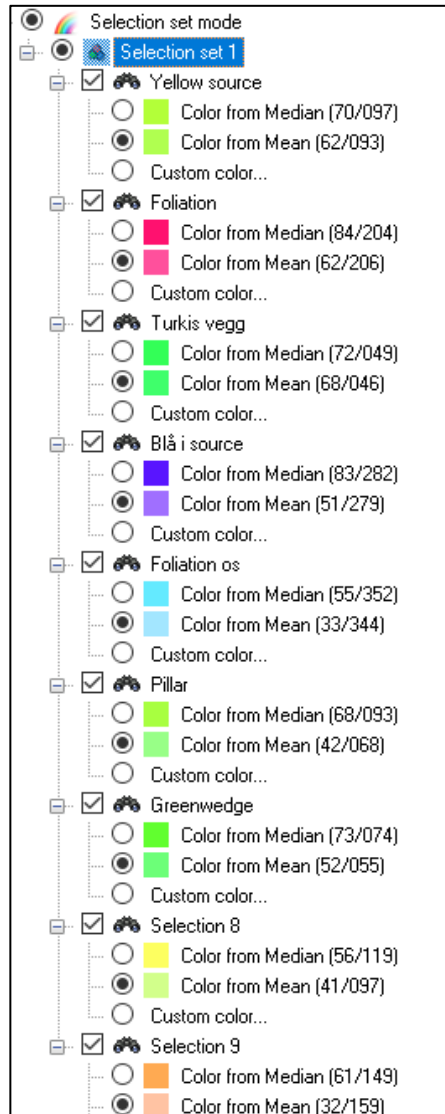


Fig. 52 Measurements from Coltop3D showing mean and median dip and dip direction of different colorcoded polygons on the point cloud.

Dip and dip direction of structures within polygons are shown on the HSI wheel in Fig. 53 and the same data has been exported and plotted on stereonet Fig. 54. The poles show steep NE-SW striking surfaces, low-angle N dipping surfaces, WNW-SSE striking foliation, steep N-S striking surfaces, and NW-SE structures. The poles plotted in Dips have, as mentioned in chapter 4.7, been statistically reduced and show steeper planes than would be expected. The poles also display structures that are more NE facing than would be expected from the orientations given in Coltop3D.

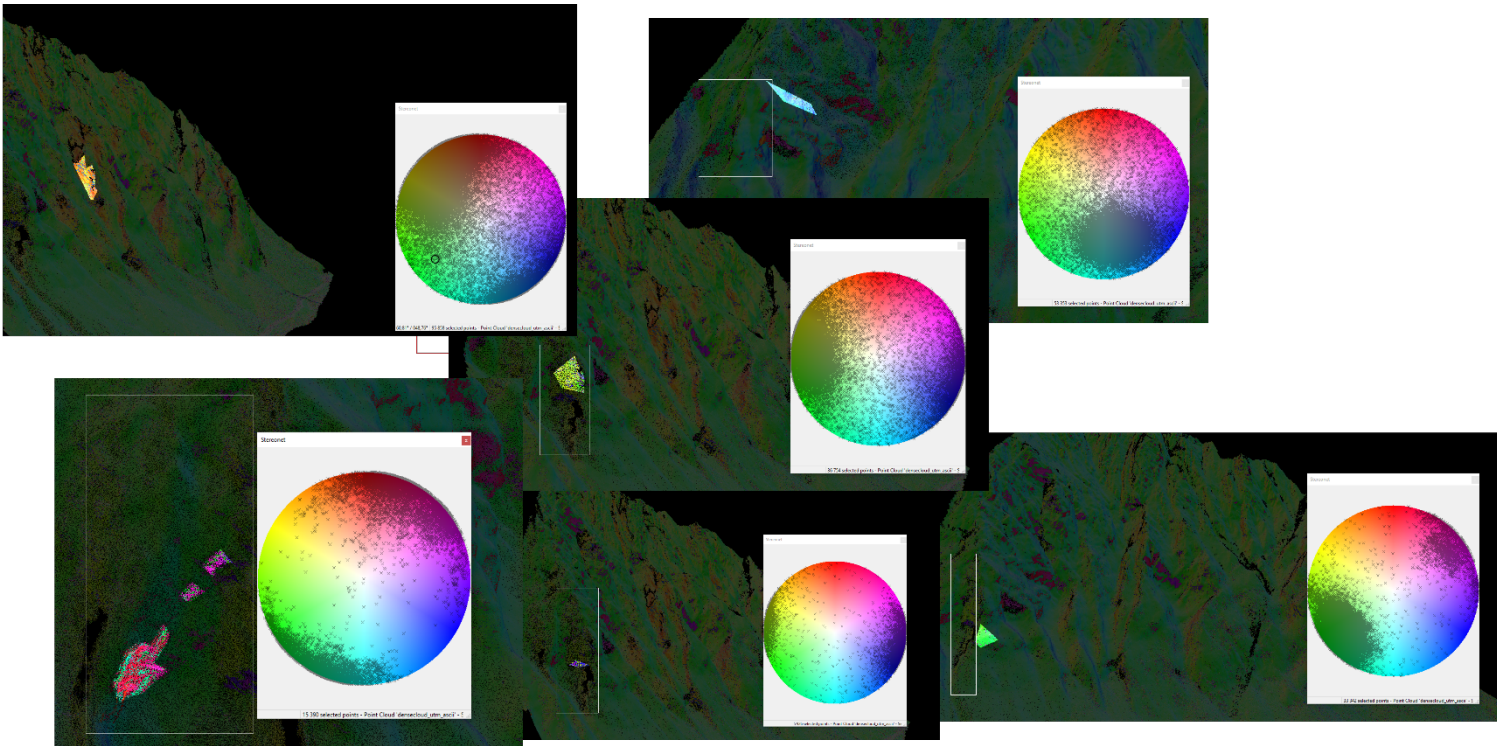


Fig. 53 Figures show dip/dip direction of poles from selected polygons on the HSI wheel and displays the orientation of the structures. There is some scatter of poles but they correlates well with observations from structural orientation data from the field.

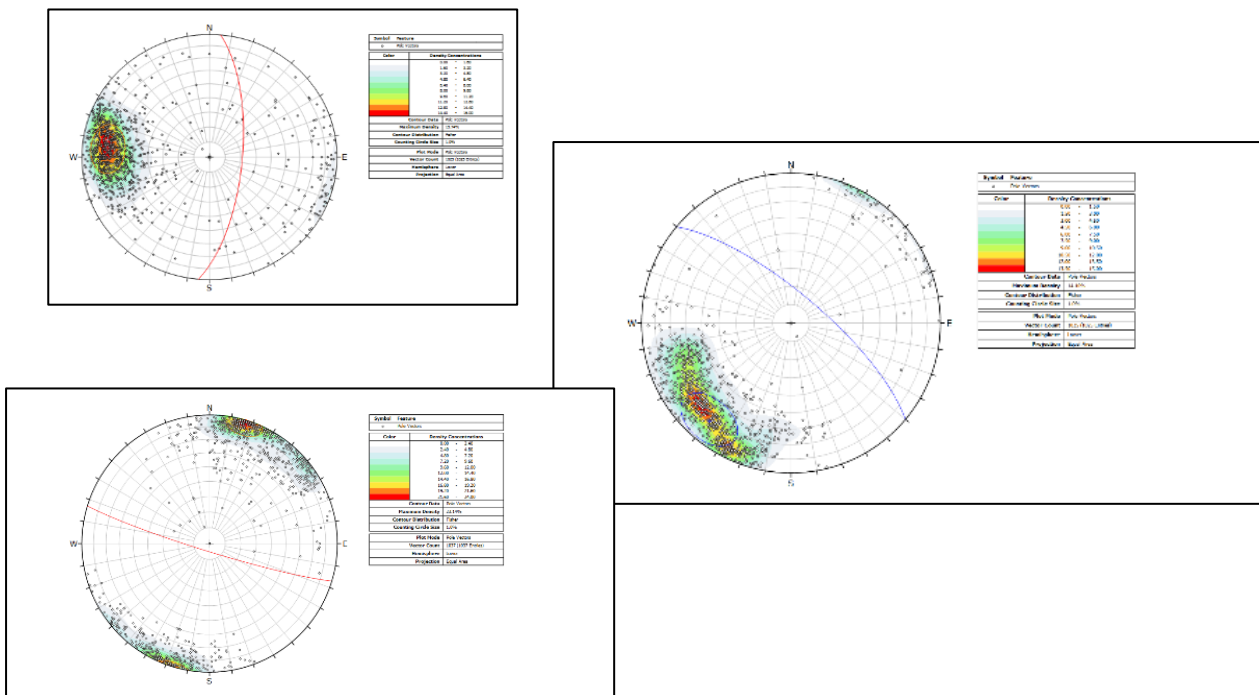


Fig. 54 Structural orientation data retrieved from Coltop3D and plotted in Dips, from selected polygons in Fig. 53. Top left represents data from N-S striking structures (green/yellow-yellow/orange polygons), bottom left WNW-SES structures (pink polygons), and stereonet to the right, N dipping structures (light blue polygons).

A closer look on the southern part of the wall clearly show steep, SW facing areas (Fig. 55), that are overhanging and not easily identified on other models or maps based on satellite images. The rockfall prone area is N-S striking with such a steep dip that it shifts to overhanging and changes color at the bottom of the wall. The N facing shelves are also recognizable as structures in the NE facing pillars and general slope direction.

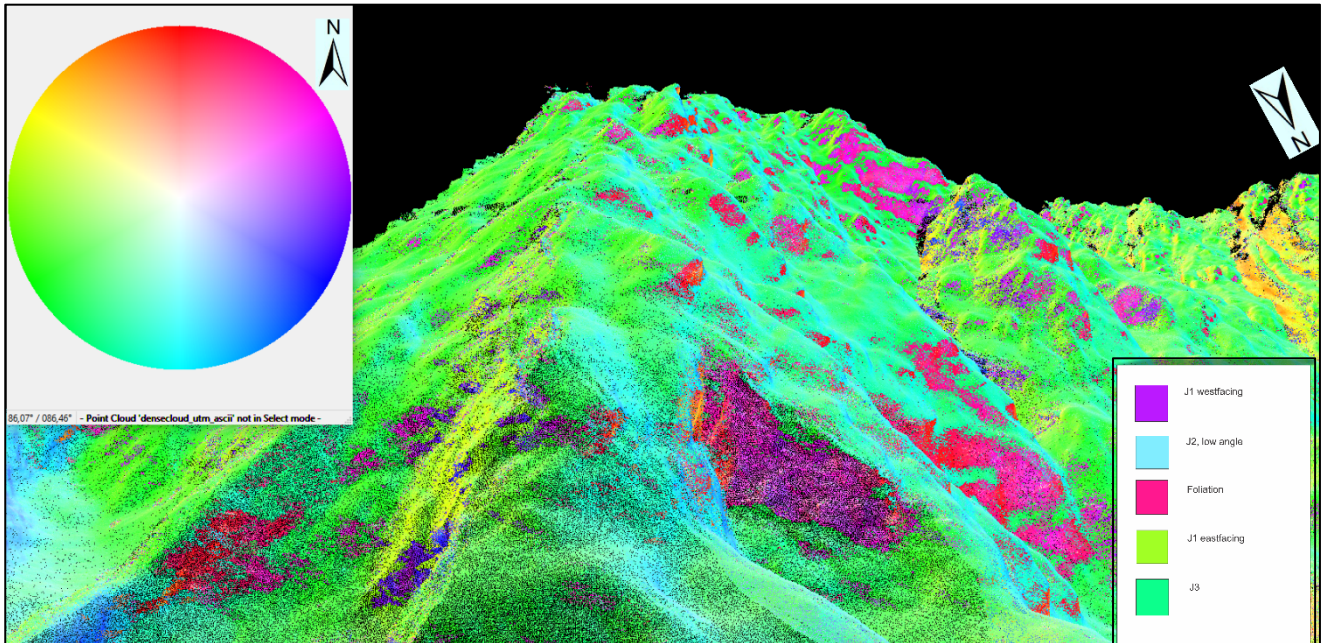


Fig. 55 Close up of release area of the rock avalanche on the southern part of the wall (dihedral left in picture). The large areas of overhanging foliation dipping to SSW are clearly seen in the lower part of the face, at the same height as the overhanging area (blue) in the opposite wall. The NE facing (green) surfaces is interrupted by fractures/joints from the low angle N facing structures (light blue). This image also visualizes well the many pillars that the slope consists of.

5.10 Overview of Slettind joint sets

The main joint sets from field observations are shown at each location in Fig. 56, in combination with bedrock type. The lower altitude locations have similarities in deformation structures, while measurements from the summit differ.

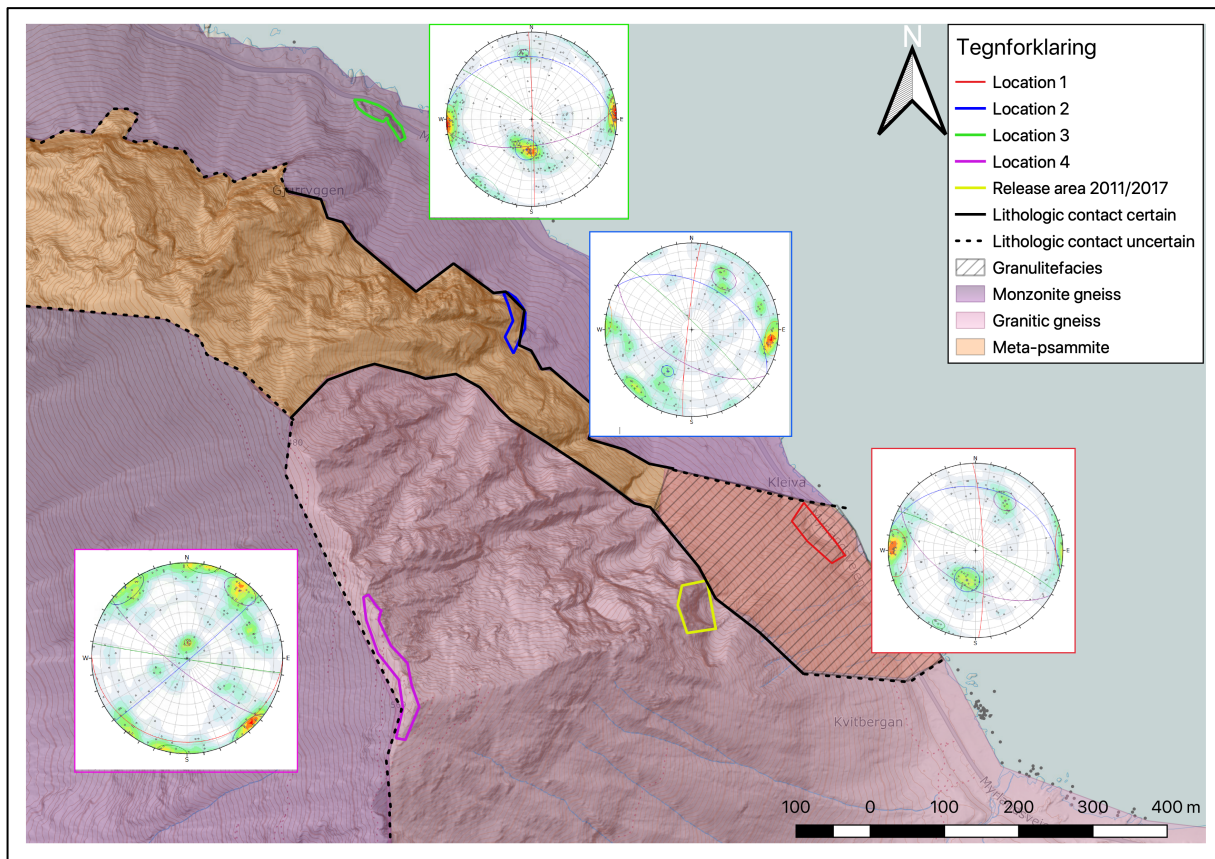


Fig. 56 The mean joint sets and foliation at the locations are shown, along with the difference in lithology. The three lower locations are quite similar, while the summit (location 4) differs and lacks the N-S striking J1.

Location 1 and 3 show similar orientation data within all the different joint/fracture sets, and only foliation in location 3 differs as oriented slightly more towards S (Fig. 56). Location 2 has less steep foliation than the other locations but share the same dip direction towards SW. The joint sets/fractures of location 2 stands out with different orientations, J1 has a more westerly dip direction, J2 is steeper and J3 is oriented more towards east. Location 4 has a steeper foliation but similar dip direction and a large difference in joint sets compared to the other locations. Type of bedrock will influence both ductile and brittle deformation structures. A weaker bedrock will show less steep foliation compared to a stronger bedrock, during the same conditions.

Joint set	Dip/Dip direction	Daylight Location/Coltop3D color
J1	83/083 ±5°	Location 1 & 3/ Green-yellow
J2	29/016 ±5°	Location 1 & 3/ Not present in Coltop3D data
J3	84/027 ±15°	Location 1, 2 & 3/Turquoise
Foliation	56/211±20°	Location 1, 2, 3, 4/ Pink

Coltop3D confirms the orientation of joint sets but it is noticeable that low-angle planes are not visible and therefore, not easily to be detected. A low-angle plane would have a light color, almost white in some cases, which is not to be found, neither by searching the model nor by data exporting. The data export from Coltop3D also surprisingly often turns out to be oriented towards NE, which may be a result of the large dataset being influenced by the general slope direction. Structural orientation data from Coltop3D is therefore not used in kinematic analysis.

6 Kinematic analysis

6.1 Kinematics failure analysis

All joint sets/fractures identified during fieldwork have been analyzed using kinematic analysis for the main slope direction, to determine potential failure mechanisms. The overall slope is dipping 80° (exposed bedrock section only) to the NE (dip direction 50°). All measurements (828) from field observations has been used. Friction angle has been set to a conservative 27°, and lateral limits 20° (planar and toppling). Below is kinematic analysis for planar sliding, wedge sliding, direct toppling and flexural toppling.

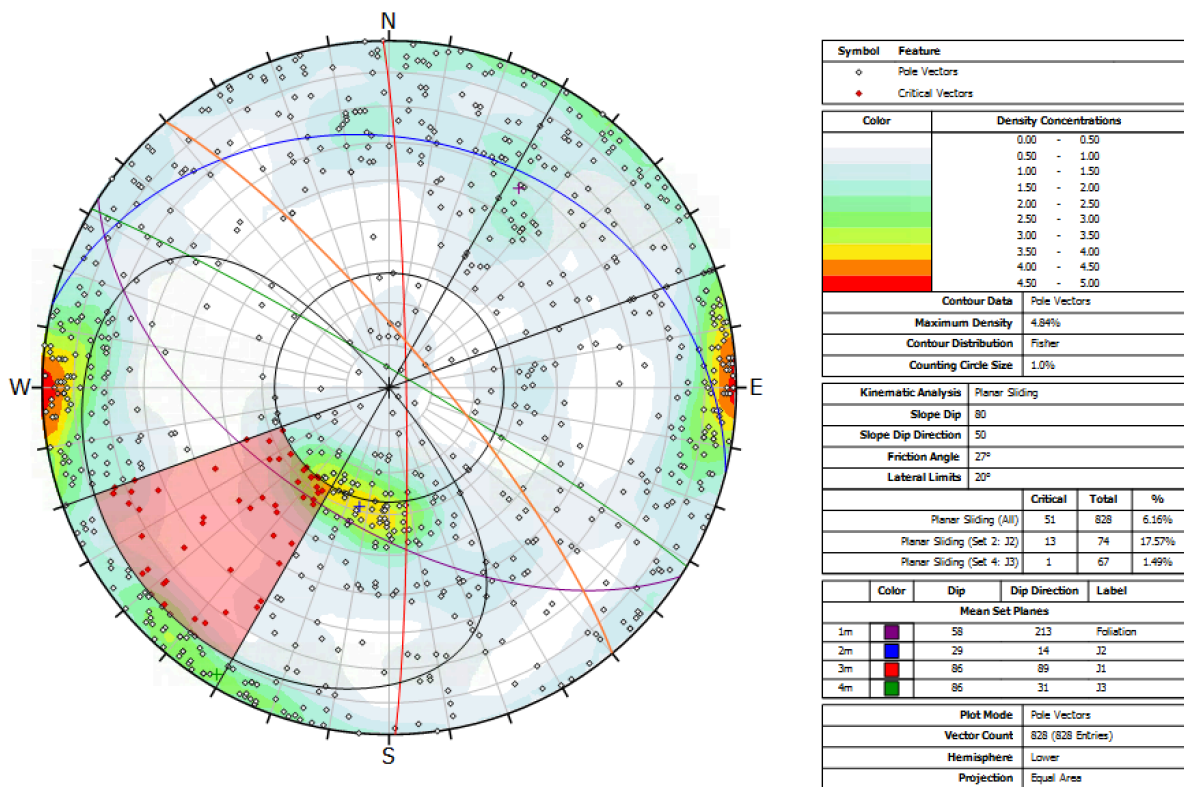


Fig. 57 Planar sliding for mean joint sets,

Planar sliding does not have critical overall percentage (6.16%) but the low-angle J2 is the most exposed joint set (17,52%), especially if slope direction changes slightly more to the east.

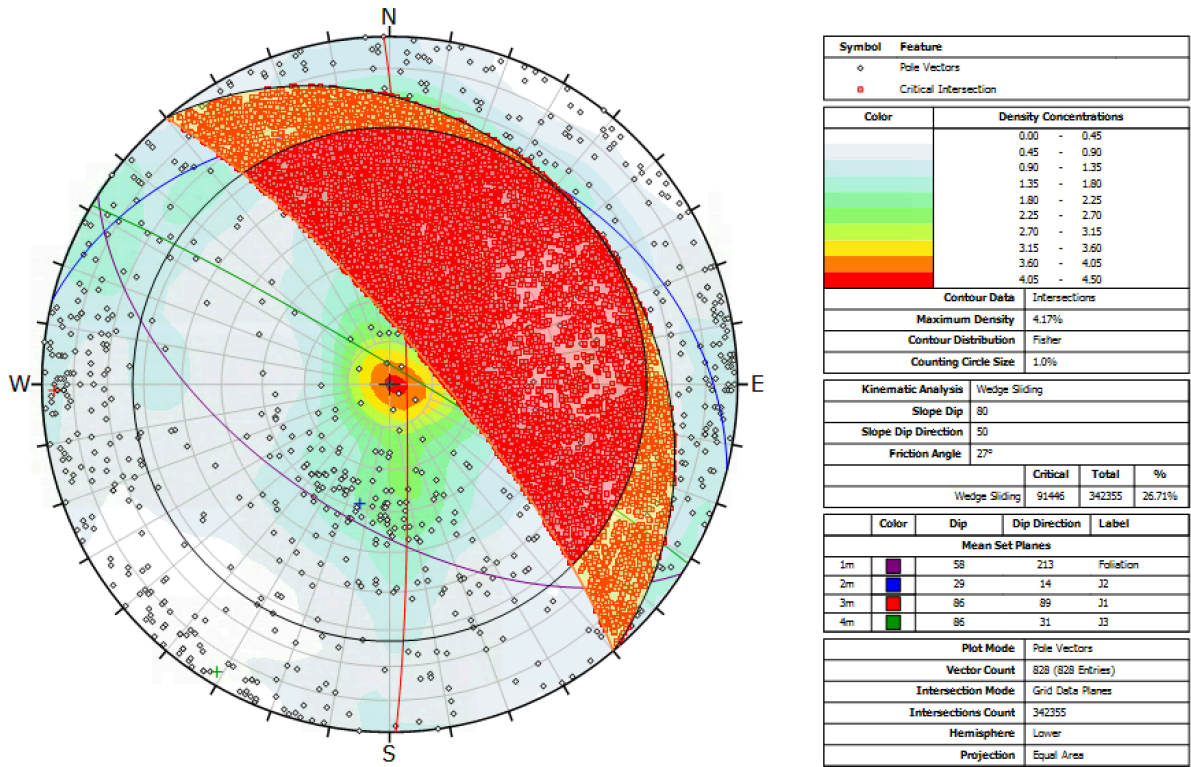


Fig. 58 Kinematic analysis for wedge sliding, contours around intersections

The critical vectors susceptible to wedge failure is at 26.71%, with the intersection of J1 and J2 as the critical one. Due to the trend line of intersection being towards N, the failure will slide along J2.

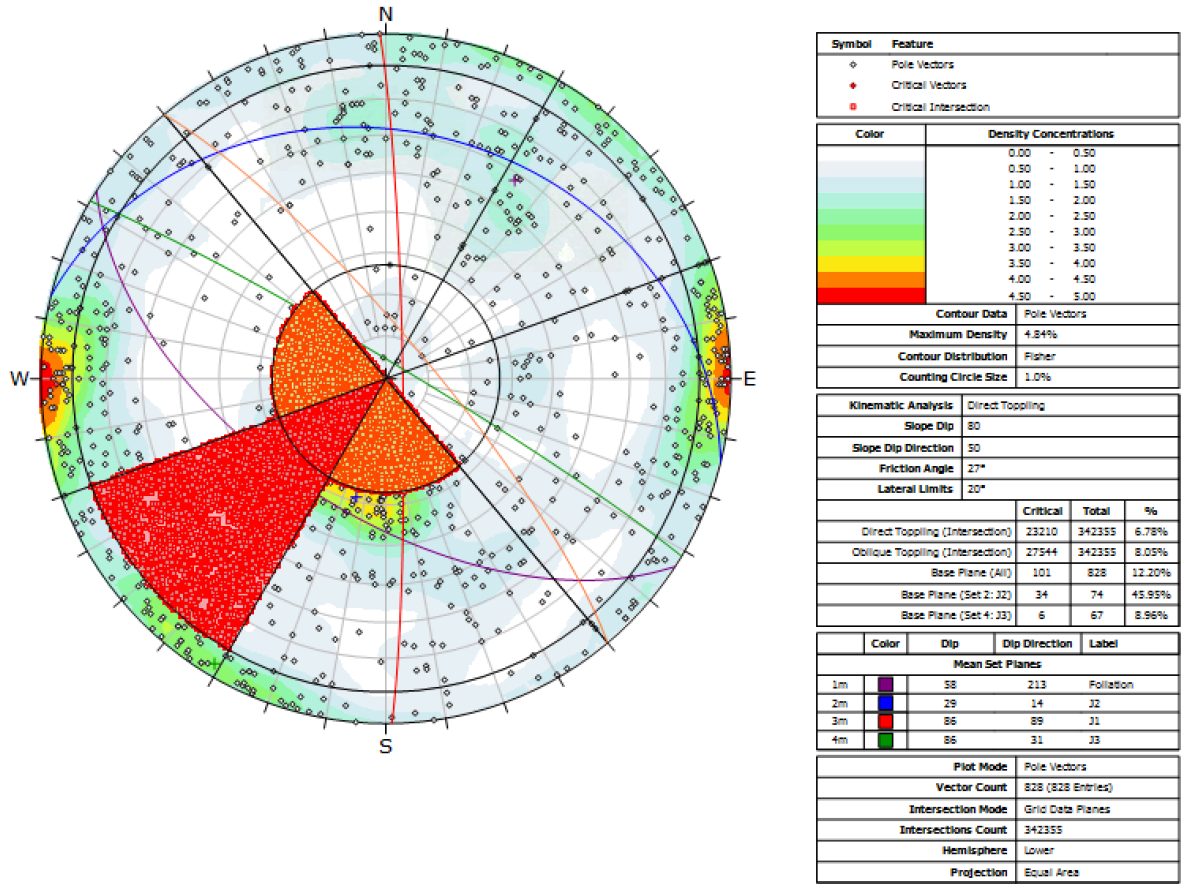


Fig. 59 Kinematic analyse for direct toppling, mean planes

Direct toppling is slightly more critical for oblique toppling (8.05%), where J2 is the most exposed joint surface (45.85%). Only a slight difference in direction (towards N), or steepness, will also rend J3 critical vectors.

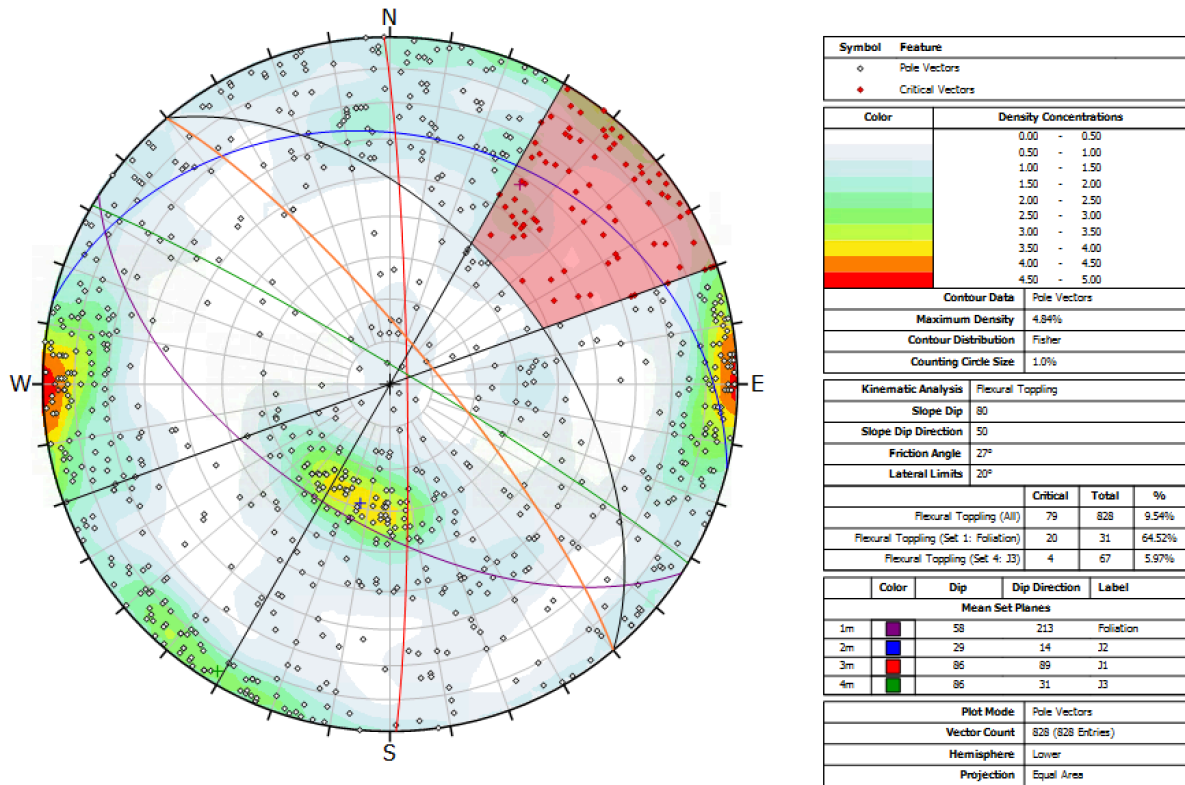


Fig. 60 Flexural toppling is critical for foliation

As for direct toppling, flexural toppling is not a very high value overall (9.54%), but for foliation critical vectors are 64.52%.

Wedge sliding is the most critical failure mechanism with a total of 26.71% critical vectors, from the intersection between J1/J2. Since the dip direction of J2 lies within the trend of the line of intersection (NWN) and dip direction of the face, the wedge will slide only on this surface. This confirms observations from the field and 3D model where interactions between the J1 and J2 forms small- and large-scale wedges over the entire slope (Fig. 32). It may be worth mentioning that only a slight change of dip direction of either J3 or foliation will cause wedge sliding.

Kinematic analysis also shows flexural toppling as a potential failure mechanism, especially critical for foliation (64.52%) (Fig. 60).

6.2 Coltop3D critical joint sets

The critical joints/fractures prone to failure identified with kinematic analysis, is based on the mean directions of joint sets/fractures found at field observations and confirmed in Coltop3D. They have been highlighted (Fig. 61) in Coltop3D for identification purposes. The main focus is to identify the intersecting joints J1/J2 where J2 will act as the main sliding plane for wedge failure.

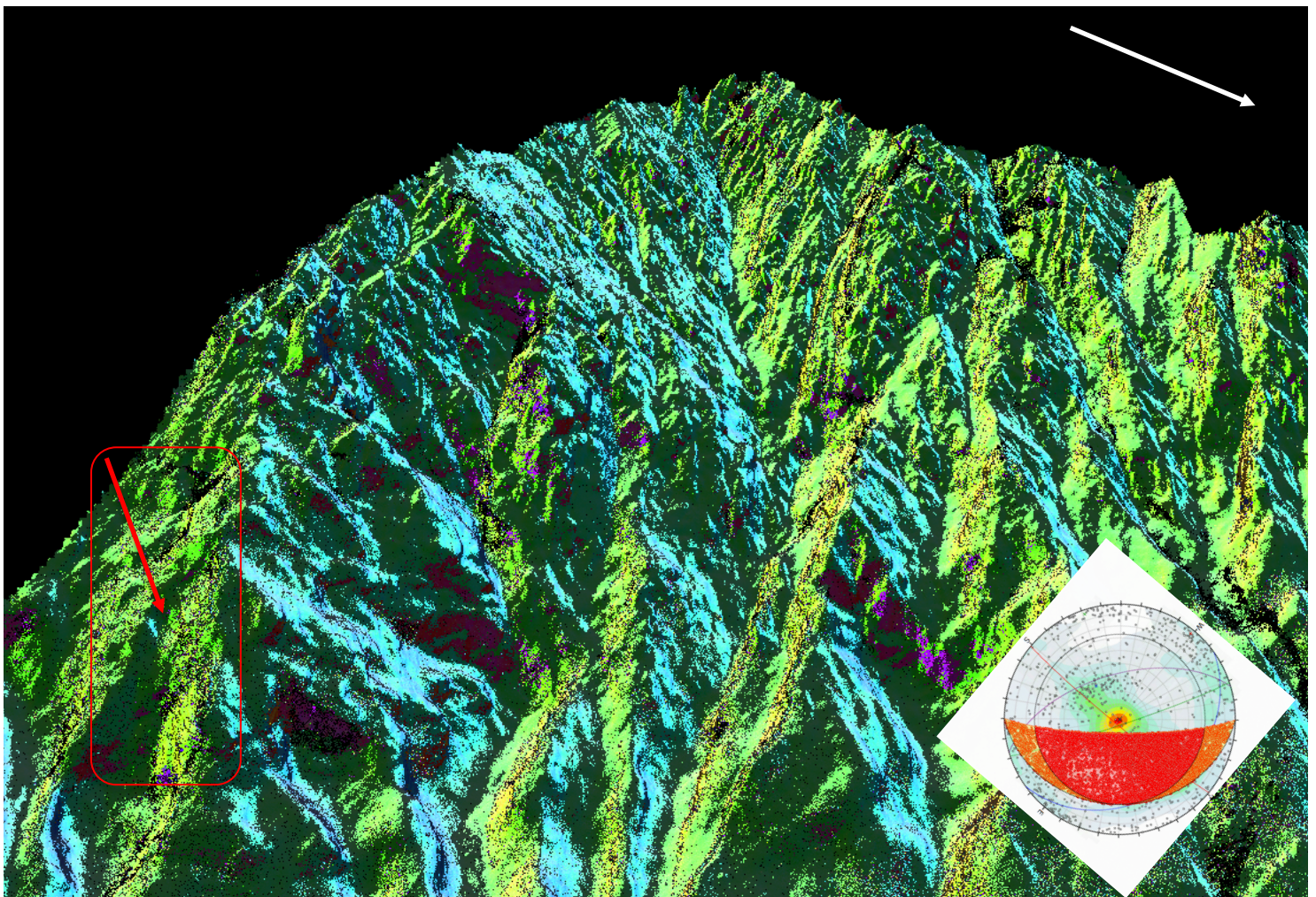


Fig. 61 Model in Coltop3D has highlighted the critical joint sets J1 and J2 for wedge failure. J1 is highlighted in a yellow/green color, J2 as light blue. Red rectangle indicates the 2011/17 release area. Red arrow indicates a dihedral that is created due to the intersecting of J1 and J3 (not highlighted). The joint sets of J2 is traced through J1 and also present in the opposing wall. Kinematic analysis rotated to fit the slope direction.

The intersecting J1/J2 (yellow/green and blue) surfaces form large low-angle dihedrals over the entire slope (Fig. 61). The J1 (yellow/green) structures seen in Coltop3D are identified as

bare, often broken rock, when compared to the 3Dmodel. The larger J2 (light-blue) shelves are grasscovered structures, with no signs of failure on them. The zones prone to failure are to be observed where J2 daylights within J1, rather than the low-angle dihedrals (Fig. 62). This is the case at the release area. The J2 joint set (light blue) (Fig. 62) is even noticeable as a consistent joint in the opposing wall.

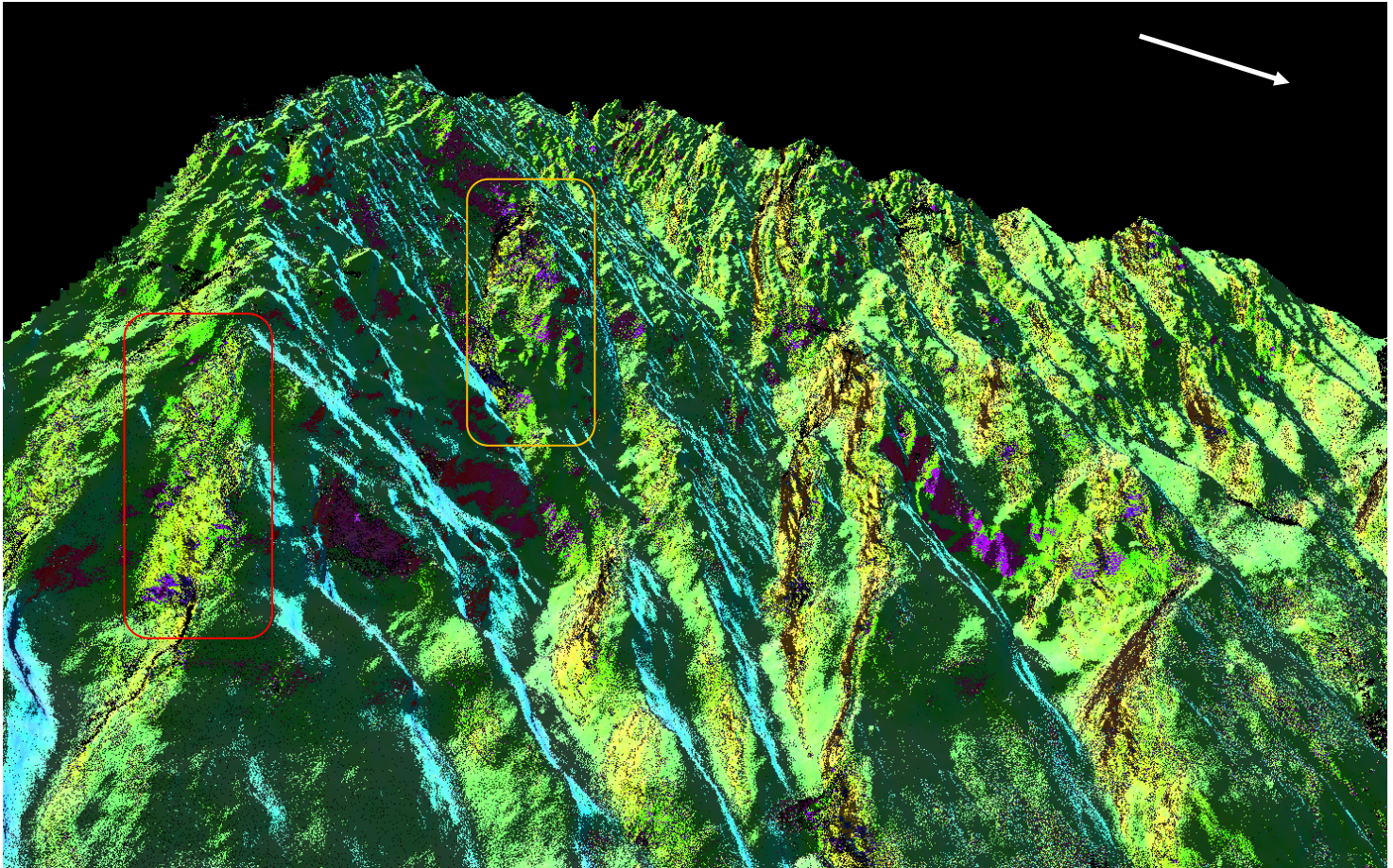


Fig. 62 The source area is within the red box. This image visualizes well how J2 (light-blue) splits J1 (green/yellow). The two joint sets interact and creates the structure of the ridge above the release area and isolates independent blocks and small pillars. The large pillar in the middle of the image (orange box) is also isolated by J2.

Finding daylighting J2 in the steep J1 will indicate sections that may be prone to wedge failure. The steep ridge with multiple pillars above the source area 2011/17, all show similar structural geology. A closer analyze of the source area was not able to identify the low-angle joint set of J1-planes, but the structure in the bedrock is visible and possible to locate by eye-view (Fig. 63).

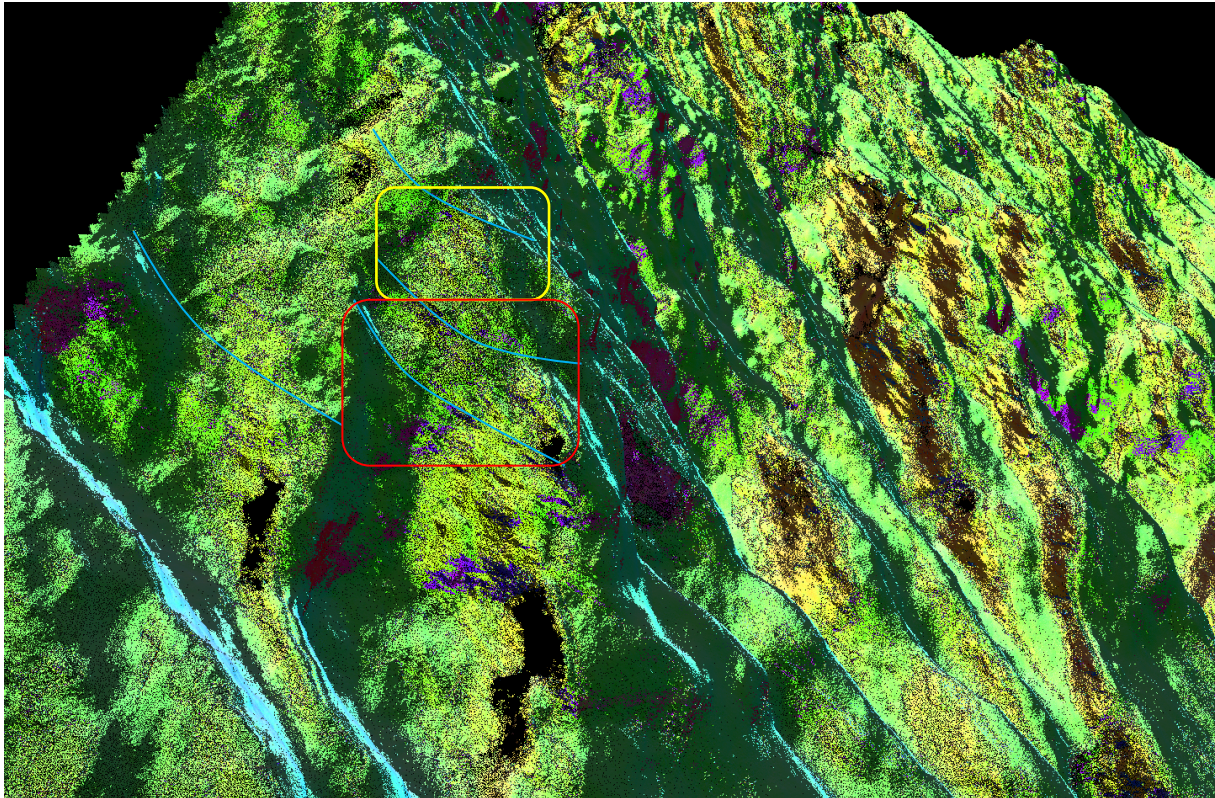


Fig. 63 View from east and a close-up of the dihedral in the release area (yellow box=2011, red box=2017). Blue lines tracing N dipping J2 joints, traceable in both opposing walls. The J2 joints intersects J1 E facing surfaces and are visible in other structures as well, as the non-highlighted N facing J3. Violet indicates a steep W facing variation (overhanging structures) of J1.

It is worth noting that outside of the UAV flight inspected area, the SE facing wall of Slettind joins the ridge of the release area. The wall is identically oriented as the J1 structures, which is seen in Fig. 56 in chapter 6 and is a large structure inflecting the narrow ridge.

7 Discussion

In this chapter the conditioning factors for rockfall, realized by the lithology and tectonic lineation's formed by ductile and brittle structures at Slettind and their influence will be discussed. The critical failure mechanisms discovered by kinematic analysis and identified potential locations on the rockslope will be accounted for, based on results from stereonet and 3D visualization. Triggering factors will also be discussed in relation to the failure mechanisms. Finally, the method using UAV-derived SfM model will be discussed and strengths, weaknesses and issues accounted for.

7.1 Conditioning factors for rock slope failure at Slettind

The glacial ice during the Last Glacial Maximum reached the continental margin and was grounded in fjords and covered the islands of Lofoten. It eroded and transported debris from the entire continent, including the mountains and slopes in Lofoten, and it was deposited as moraines at the seafloor. Since the north going marine based ice stream of LGM passed by Slettind in Nappstraumen, and probably was thick enough to reach the height of today's summit, it would have removed earlier debris and rockfall from before the glacial period. The colluvium slopes and debris from Slettind is therefore no older than 16 300 BP (Vorren et al., 2015). Following deglaciation, rock slopes became unstable due to the stress-release and large rock avalanches and rockfalls occurred (Ballantyne et al., 2014). The rise in sea-level caused by the melting of the ice sheet provoked a rise of 35-38 m above present day level (Laberg et al., 2018). Rock failure at Slettind after deglaciation have then deposited freefalling rocks directly in water. Despite the large effects the ice stream had, Slettind is little affected by exfoliation cracks following isostatic rebound, and more driven by tectonic lineations. This is seen as the alpine landscape is controlled by lineations, foliation and scarps accentuated by the glacial erosion (Redfield et al., 2005; Trulssen 2008; Hendriks et al., 2010; Eig & Bergh 2011; Bergh et al. 2018).

The apex of the colluvium fans along the NE slope of Slettind starts at 150 m.a.s.l. with an inclination at 40° and the slope doesn't ease to below 30° until the road, where the terrain flattens out to 10-20° in the matter of 30 m. Large boulders form fan shapes in the water, which is seen on the aerial photographs. The proximate parts of the slope act as a transport area for debris which have contact with the slope by rolling or bouncing. There is little deposition on the slope, mostly minor rocks or finer material and the occasional larger boulder, that are often covered by vegetation. The size of some of these large boulders, little irregularities of the slope and hardness of the colluvium slopes would indicate a long run-out trajectory. Due to the abrupt change in slope inclination and the sea, none has travelled farther than 60-80 m away from where slope turns to <30 °.



Fig. 63 Photo of Slettind (in the middle of the picture), taken from helicopter by Viggo Aronsen in 2013. Note the steep colluvial fans, short run-out zone without ease in slope, and how there is little deposition on the slope below the rockwall

The dominating processes forming the colluvial fans are decisive for slope inclination, steeper slopes are typically dominated by rockfall, compared to slopes where processes involving water such as earth/debris flows, or snow avalanches (Blikra et al., 1989, Volkwein et al., 2011). The abrupt change in inclination suggests that rockfall is the dominating process along the entire mountain. There is little interaction between falling blocks, and although quite a few boulders are larger than 100 m^3 the flowing continuous massmovement, typical for rock avalanches is lacking. Depending on type of classification used (Devoli et al., 2011; Hungr et al., 2014) the most active process at Slettind has more in common with rockfall than the flow of rock avalanches despite the volume of the events (Blikra et al., 2006). Little interaction between blocks is also typical for hard rock types, and there is a large spreadout of individual blocks. The large structures at Slettind and high fracture frequency in bedrock produces both large and small blocks that are deposited in a sorted fashion, coarsening downwards, where the largest blocks have the longest run-out distances (Dorren, 2010). The blocks are somewhat orientationally deposited. The colluvial fans show layering as a result of rockfalls in episodic events suggesting that rockfalls are, or have been, more intense in certain periods, most likely during rainfall events and snow melt.

The thin vegetation cover on the steep slopes allows larger events to reactivate the unstable debris on the slope causing a potential larger deposit on the road than the initial rockfall might have been. Vegetation also affects the loss of kinetic energy at impact, and a thin cover gives little attenuation. Some large boulders by the road or on the slope are covered by debris/fractured rock, suggesting that multiple events have happened since they were deposited. Some are even slightly rounded indicating weathering and erosion, and those close to the shore show signs of wave-erosion.

The lack of migrating debris channels, levees, and lobes confirms that waterrelated processes is not dominating on Slettind, despite that the colluvial fans might have had a more gradual slope inclination if the toe wouldn't have ended in water. The narrow summitridge and steep sides of the slope limit the potential source for either water or snow accumulation, meaning that water as a triggering factor only is related to melting of snowcover in spring, or heavy rainfall.

Slettind is dominated by tectonic lineations connected to the rifting and opening of the North Atlantic Ocean during the Permian-Jurassic to Cenozoic (Brekke, 2000; Eig & Bergh, 2011; Faleide et al., 2008; Osmundsen et al., 2002). The extension created normal faults, horsts and grabens in the Archaean to Paleoproterozoic gneisses. The following rotation of the stressaxis due to a shift in the rifting is linked to the transform fault of the Hornsund-DeGeer system near the Barents Sea margin (Eig & Bergh, 2011). This rotation created a strike-slip deformation also present in Lofoten in the late Cretaceous to Paleogene. The brittle structures such as faults and fractures, truncates ductile structures and are therefore younger.

The Precambrian foliation is preserved in the Archaean high grade gneisses at Slettind, dipping towards S in a folded manner with progressively changing dip direction to the SW in the southern parts of the mountain (location 1) and SE in the northern parts (location 2). The bedrock rotates due to ductile and weak folding in structures in the northern parts responding to the alternating layers of felsic and mafic Neoproterozoic units of gneiss. Ductile deformation in the less rigid rock of the meta-psammitic causes lower angle foliation compared to the steeper foliation in the granitic gneiss. Foliation is not prominent in the younger and massive monzonite. The weak foliation and banding means that a failure will only result in minor rockfailures.

The ductile foliation is parallel to the south dipping lineament (J1) that creates the characteristic structures at Slettind (Fig. 64; 65), which overlap partially with the brittle fractures striking ENE-WSW, found by Bergh et al. (2007) and named S2. It is parallel to the main NE-SW trend of the Lofoten islands and Vestfjorden Basin (Gabrielsen et al. 2002), and is marked by linear escarpments along the coastal cliffs to the north and south of Lofoten, such as linear valleys of the interior at Leknes, and the linear depression along Ingelsfjorden. In all these areas brittle faults/fractures produced rhombic and zigzag-shaped landscapes.

The second set of lineaments (J2), strikes NW-SE (Fig. 64) with a rotation towards WNW-ESE. This lineament is responsible for the fjords and normal faults separating the Lofoten islands. It is related to the Permo-Jurassic rifting/extension event along the Lofoten margin with extension in a W-E direction called S1 (Bergh et al. 2007; Hansen & Bergh 2012). This

lineament is parallel to Nappstraumen and similarly oriented fjords in westernmost Lofoten. At Slettind the largest structure is the southern major wall dipping towards SE at the end of the ridge (Fig 64) and seen at the release area as the steep, straight and continuous lineaments (Fig. 65). They all show a straight to right-stepping geometry, where individual fault traces die out or breach along strike.

The third lineament (J3) that trends NW-SE is parallel to the general slope direction (Fig. 64), as mentioned earlier (chapter 3.1.1) it can be explained related to the late Cretaceous to Paleogene rifting event of the Lofoten margin (Bergh et al. 2007) and the lineament was called S3. This event created extension in a NNW-SSE to NNE-SSW direction, creating normal faults and fracture sets dipping NE and SW, and subsidiary NW-SE trending strike-slip faults (Eig & Bergh, 2011). The third, NW-SE striking set is well displayed as rectilinear fault-fracture strands along steep valleys and coastal cliff sections in the westernmost Lofoten islands (Fig. 8).

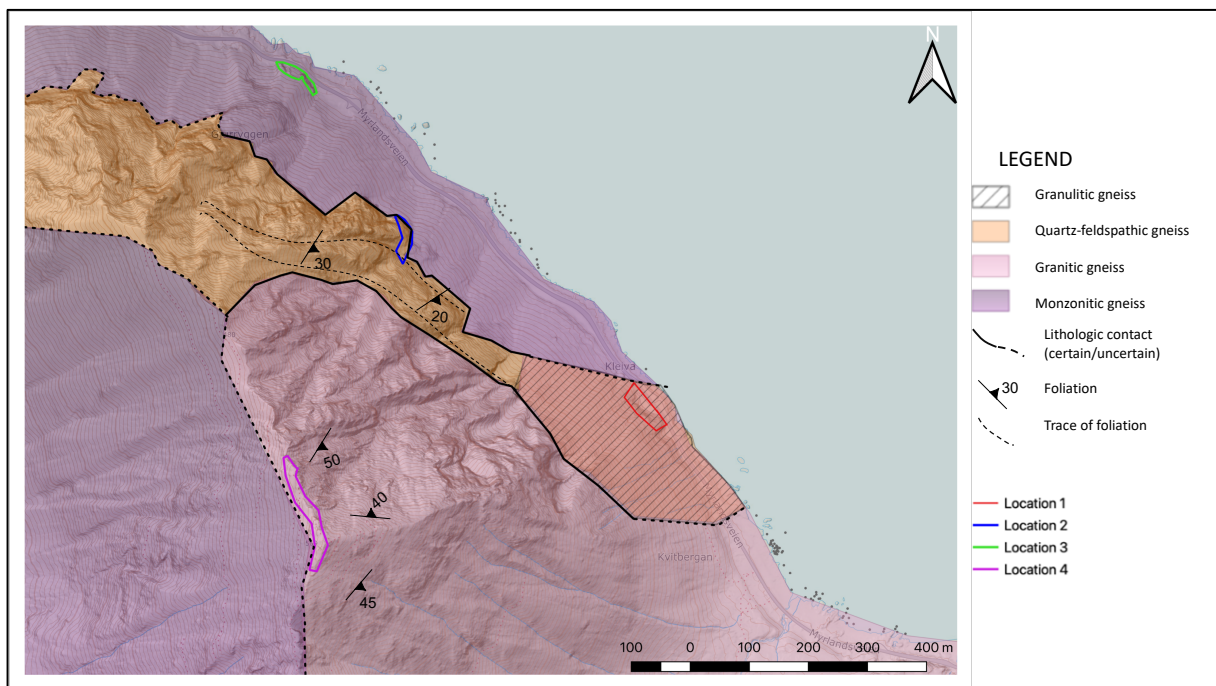


Fig. 64 Dip and dip direction of lineations in combination with lithology.

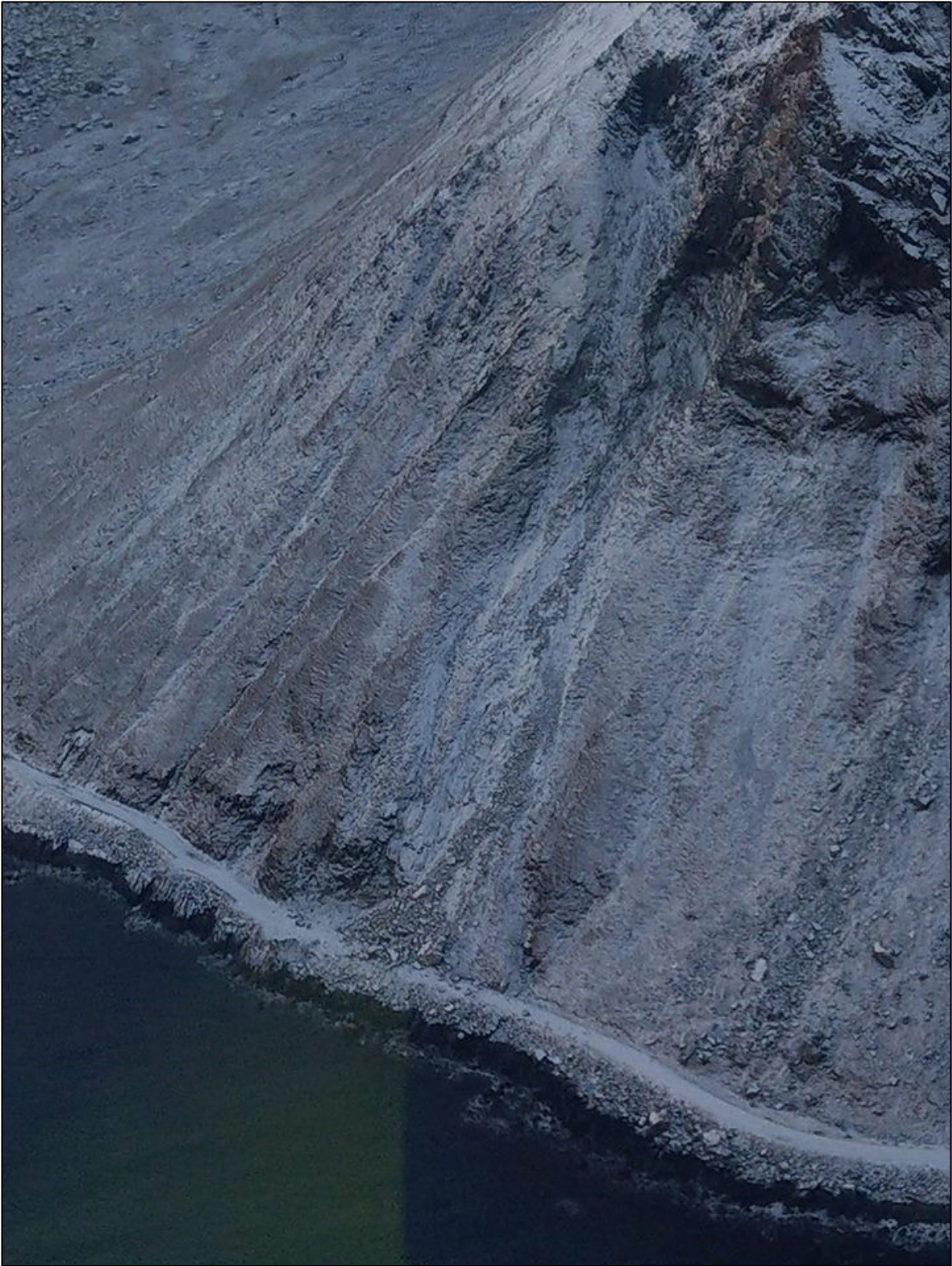


Fig. 65 Photograph from SVV, taken in helicopter of the release area 2011/17. The structures affecting the release area is really well seen from this angle and J1 and J2 is easily identified continuously through the entire rockslope. The similarity between J1 and the SE wall in the background (barely seen) is striking. Three minor surfaces of J3 is also shaping the area. Note the deposit from rockfall on the road.

The tectonic lineaments are varying in orientation at lithologic contacts. This is seen in the intrusive massive monzonite being less dominated by ductile folding and instead highly affected by the brittle fractures following S2 and S3 directions (Bergh et al. 2007). The quartz-feltpathic gneiss, on the other hand, shows more ductile deformation and a more compact bedrock structure with failure following foliation. The lineations are less steep in this bedrock along the entire contact. The release area is situated in a more rigid bedrock than the metasedimentary, resulting in lower angle foliation and more fractures.

The foliation shows a large-structure fold, that dips into the slope and seem to have little effect on the overall failure mechanism. Failure along foliation is visible as minor, successive overhangs only along slope parallel planes (J3). This is especially seen low on the rock wall (Fig. 32 & 36) immediately above the apex of colluvium fans, and at the end of channels with running water, on slope parallel surfaces. Erosion due to successive freeze/thaw processes where the combination of a snowcover on the slope and the running of water would augment the speed of weathering on the rock and removal of minor blocks. This phenomenon doesn't create large rockfalls but may act as an additional destabilizing factor.

Although the rock avalanche in 2011/17 was in the granitic gneiss (Fig. 64) there is rock failure along the entire slope of Slettind independent of lithology. Further north from this release area, rockfall is numerous but the blocks have been smaller in size. The lithology has a small effect on the structural orientation of the fractures and the foliation of the bedrock at this site but is not decisive as a failure mechanism. The failure mechanism at Slettind is rather structurally driven by favorable orientations of joints and fractures. Since the lineation's are similar to the joint sets found, the large-scale regional tectonic events have created brittle structures that have been reactivated due to erosion.

7.2 Kinematic analysis and triggering factors

Field measurements found three dominating joint sets, one N-S striking vertical set (80-90°) dipping either east or west (J1), one W-E striking dipping with a low angle (20-35°) to N (J2) and W-E striking dipping steeply (80-90°) towards NE. The joint sets correspond well with the brittle lineations found, whereas J1 is in addition partly parallel to the ductile deformation and foliation of J1. Foliation is found to be oriented WNW-ESE with a steep dip towards SW (55-60°) and is weakly banded such that failing doesn't produce large blocks. It is only sparsely present as a daylighting structure in NE facing steep walls of the granitic gneiss and causes overhanging surfaces.

As structural orientation data weren't collected directly at the release area or on bedrock on the steeper parts of the wall, it is an assumption that they correspond through the entire slope, affirmed by the structures found in Coltop3D. This assumption is however, partly weakened by the field measurements of structural orientations from the heavily weathered joint/fracture surfaces at the summit (location 4). The ridge was heavily eroded and fractured, and very sparse outcrops with in-situ rock was present and the collected data is considered not very representative. The orientation data from the outcrops close to the road was validated by the structural analysis done in Coltop3d and shows structures with similar dip and dip direction from lower to higher altitude on the slope.

Data from the software Coltop3d, based on the UAV derived point cloud, show two dominating joint set/fractures, a N facing dipping 30-35° and one E-SE facing 40-60° opposing each other in an orthogonal manner, the N facing more dominant in the southern part of the wall and the SE facing in the northern parts. The third set is slope parallel striking NW-SE dipping NE with a dip of 40-60° mostly present in more compact pillars or in shorter rock sections. It is also evident that foliation found by Coltop3D only is daylighting in these rock sections with a dip and dip direction of 62/206-210°, and almost exclusively in the southern parts of Slettind. Using the orientation data from Coltop3D for such large structures turned out problematic when the data was plotted in a third-party software for stereographic projection. The stereographic projection showed slope parallel orientations even when the

data contained surfaces dominating in other directions. The data often also showed an excessive dip. This may be a result of a statistic bias due to the large amount of data extracted, and the general orientation being overrepresented compared to smaller surfaces and joint sets/fractures. When extracting data from more detailed polygons the result also seemed to differ from the orientations highlighted (Fig. 65) in the model. One explanation may be that the point cloud was not detailed enough to show joints/fractures at cm level. The final resolution was high enough (4 cm/pixel) and within Coltop3D recommendation but the complicated merging of the point cloud in Agisoft Photoscan might have produced some obscure areas. However, when comparing the mean value of dip/dip direction of the large structures in Coltop3D the field measurements were corresponding and confirmed.

The interacting between the N facing and E/SE facing surfaces creates low angle E facing dihedrals (Fig. 65). The low angle north facing shelves (J2) are grasscovered and free from debris but expose the steeper J1 (E/SE facing), that shows a blocky and heavily jointed surface, most likely similar to the outcrops with the fracture frequency of 1 m persistent joints for $<1 m^2$.

The release area is below a narrow ridge striking WNW-ENE and consists of a triangular shaped face striking in a general direction N-S with lateral limits in the south from the smooth NE-SW striking, SE dipping face. The release area continues towards the north by the irregular slope facing NE (parallel with general slope direction). The general slope direction is heavily disintegrated by steep SE facing J1 structures and the shelves from the J2 surfaces. The face is further disintegrated by walls parallel to the northfacing vertical joint set J3.

In photographs, 3Dmodel and drone photos, the release area clearly show low-angle surfaces acting as a sliding plane and dipping towards north, connected to the low-angle large shelves of the lineations J2. They are interrupted by steep, smooth joint surfaces striking N-S, and parallel to the large continuous walls of J1, areas that fits these criteria's are marked in Fig. 66. The fracture frequency in the release area indicates medium-large blocks, with singularly larger ones. The vertical face and short, steep talus mean that even smaller blocks reach the road.

Kinematic analysis done in Dips shows that wedge failure is by far the most common failure mechanism, with 26% of critical vectors, failing between J1 and J2. The line of intersection and slope direction indicates that J2 act as sole sliding plane with failure towards N (i.e. 340° NWN), This means that failure is not along the large dihedrals that has a line of intersection towards E.

The sliding plane of J2 is low-angle and normally not usual to consider a critical sliding plane (field measurements: 20-30°) overcoming the friction angle of gneiss (27-34°). Reviewing the results in Coltop3D, it suggests that J2 is steeper than results from field measurements (29-46°). A change in lithology between the field locations and the release area, might be an explanation for this slight difference in inclination. The 3D model and photographs however clearly show a low-angle J2, well corresponding to the inclination of field measurements and observations. This indicates the presence of a triggering factor provoking failure along surfaces that normally wouldn't be suspected to slide.

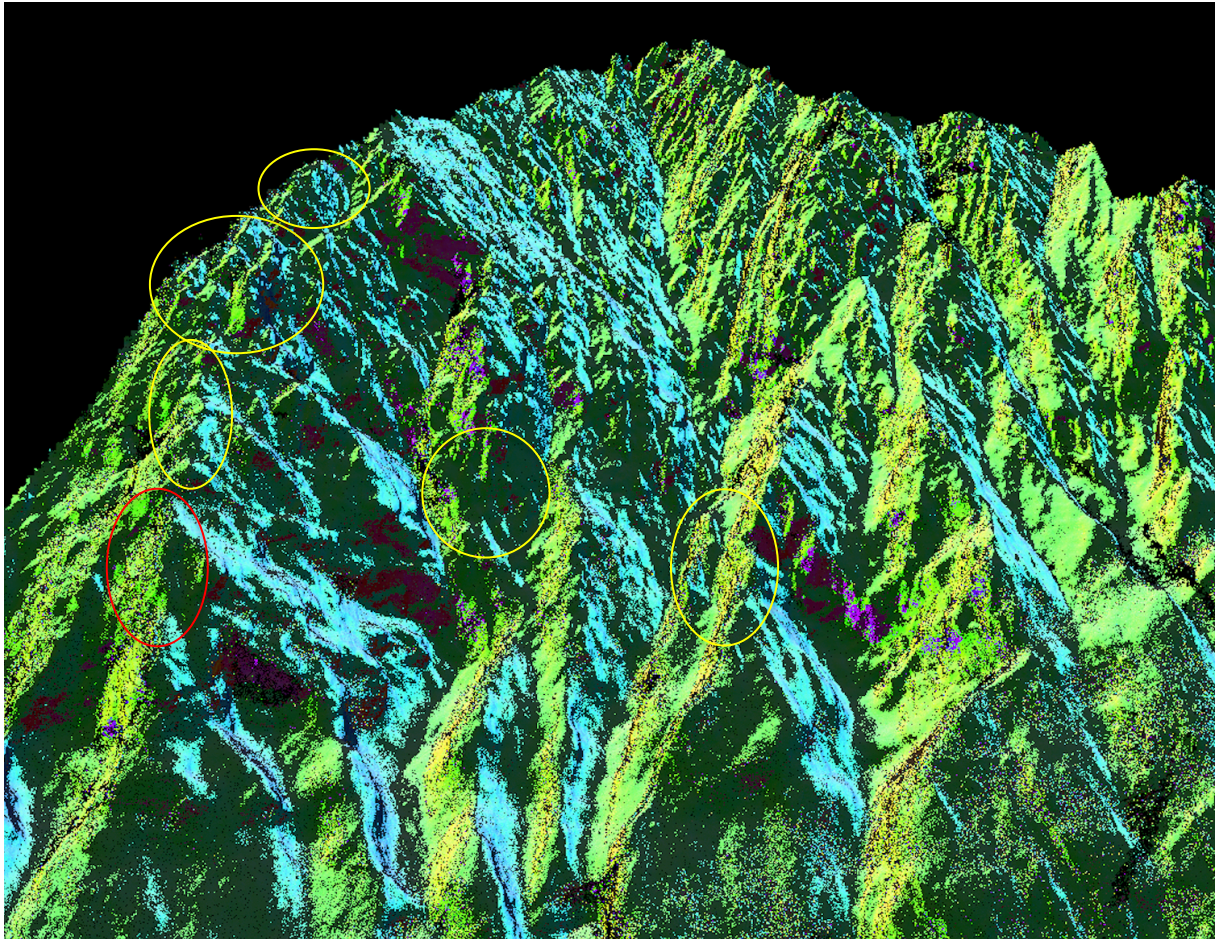


Fig. 66 Highlighted surfaces corresponding to mean surfaces of J1 (lightblue) and J2 (yellow/green). Red circle indicates release area of 2011/2017 and the area is still unstable. Yellow circles indicates areas with identical failure mechanisms.

The weather statistic and reports available indicates that the event in the summer of 2011 was related to heavy precipitation in early summer (after snowmelt), while the event of 2017 followed a period of cold weather and snow and suddenly milder temperatures with rain. A triggering factor in this case was a combination of freeze/thaw dislocations and reducing of the friction angle by water.

The thin snowcover (50 cm) at Slettind exposes the mountain to freeze and thaw related processes during the entire winter, in combination with changing and mild temperatures. Although the weather and rockfall reports are not totally liable, the general weather situation at Slettind (Xgeo, 2018) in combination with a non-existent source for either snowaccumulation or water indicates rockfall triggers as related to changes in weather rather than overall seasonal changes (snowmelt etc.).

The surfaces parallel with the general slope direction, facing N-NE, are in turn disintegrated by flexural toppling failure caused by foliation structures, confirmed by the kinematic analyze in Dips. This is also affirmed by both studying the 3D model and the highlighted fractures in Coltop3D. Failure along foliation most likely doesn't cause rockfall of large blocks because of the weak banded structure. The percentage of critical vectors for flexural toppling is so high that failure is very likely wherever foliation is daylighting within the fracture set of J3 (pillars and rockfaces similar to slope direction). Although only present in minor areas, the overhanging structure created by this mechanism will propagate further, with the potential to decrease the stability in larger areas. In combination with the weathering earlier mentioned (chapter 8.1) the overhangs become extremely steep.

The structural orientations identified in Coltop3D allowed confirmation of the measurements from the fieldwork and validated the kinematic analysis done based on these. In addition, the visualization of the orientation of joint sets and larger structures such as lineations were possible. The 3Dmodel also visualized the change in lithology and folding of the foliation, not visible from the ground or summit. To find the intersecting joint sets and critical surfaces the highlighting in Coltop3D is essential and very useful. This permitted to identify areas dominated by foliation structures exposed as overhanging patches in J3 structures, isolated in the southern part of the wall, which otherwise wouldn't have been located. This is the case also in the lower part of the release area, below the "wedge" (marked in Fig. 36), and many of the unstable blocky pillars above the release area.

7.3 UAV derived SfM models

Slettind is an exceptionally large slope to analyze with an UAV, challenging batterytime, light, weather and Norwegian flight rules. At the same time using UAV to create SfM point clouds is cheap, flexible and fast.

Airborne is the only way to collect structure orientation data to perform kinematic analysis from the release area at Slettind (Aronsen, 2017). Point clouds can be produced from TLS which can be used from helicopter but is expensive and as the site is overhanging not a full worthy alternative. TLS from the ground is not possible at Slettind as there is not enough space in front of the wall.

UAVs are sensitive to weather and wind, equally problematic to helicopter, but to make a full analyze of the mountain with UAV in a day, a huge set of batteries are required. It is risky and requires resources to fly over multiple days due to changing light, in Lofoten weather changes quickly and might delay flying as well.

Norwegian flight rules limit the use of UAV with 120 m above ground and flying in front of the wall of Slettind would ideally be at higher altitude for the 3Dmodel. Investigating a less steep mountain the slope inclination can be used to reach more height. Compared to the horizontal grids the manual flying in front of the wall came out better in light and resolution, due to less distance between the UAV and the rockslope. The manual flight had some issues at processing though, and a too large overlap of manually taken images, caused the software to crash. The large overlap was also time consuming at the stage of processing when placing GCPs manually for georeferencing. There exist apps that fly automatically in a vertical fashion which would be better for keeping a regular distance to the slope, saving battery and getting a correct overlap. Experience as a UAV pilot could have avoided flying to high in the horizontal grids as well. Processing the data, it was obvious that both the height and size of the horizontal grid could have been reduced without losing data and still return a better result.

The GCPs at the summit ridge was not visible in the images due to a too strong light, and the distance to lower parts of the wall caused inaccuracy in GCP placing. The GCPs at the shore was not identifiable and the vertical distance between the placements was too similar. New apps can fly automatic with sensor in both horizontal and vertical allowing for flights closer to the wall. The altitude difference between the horizontal grids and the manual flying in front of the wall was the largest issue with processing. Projecting a large UAV mission as Slettind

was, this is a sensitive issue to consider. The GCP placement should have involved larger difference in altitude within them, even if the one at the summit would have been visible. Ideally there should have been placed some at mid-height, and 12 points would have been appropriate. This becomes more important if the point cloud is to be analyzed at joint level and volume estimations are to be done, while a large structure analyze might be sufficient with GCP placement such as done here. The GCPs were firstly logged with GPS and then GNSS, and placing the coordinates showed a large (4 m) inaccuracy from the GPS coordinates. All these issues are immediately solved if using a Real-Time-Kinematics (RTK), Post Processing Kinematics (PPK) and Precision Point Positioning (PPP) UAV which would be the anticipated solution to this problem, resulting in accuracies of 0.5-5 m without ground control points (Gross et al., 2016).

The model had some issues that could have been devastating if they would have appeared at more critical places. During the manual flying the distance between the wall and drone varied causing an unprecise spatial resolution in certain spots. Upon merging the grids “holes” and “structures” appeared due to areas not having enough overlap, grassheight and snowpatch differences and the large difference in angle and distance between the horizontal and manual grid.

To perfectionate a large project a drone with better batterycapacity would reduce the amount of flights and facilitate merging. Recent developments in flight planning software allows to plan terrain aware auto mission flights based on loaded digital terrain models (DTM) and predefine the height of the drone above ground based on the DTM. This type of automated flight with integrated DTM should be taken in order to be able to take images from the very same height above the steep wall and to avoid too much overlap between images that increases processing time. More GCPs at varying height and closer to the release area would ameliorate the x,y,z errors.

The semi-automatic analyze in Coltop3D could have been further ameliorated by reducing noise in the point cloud, such as grassfilled shelves. In the case of Slettind however, the shelves of J2 is critical to find the joints in J1 and removing the shelves would make the task more difficult. Coltop3D fails to identify low angle joints and have been unsuccessful for using the data in third-party software for kinematic analysis. However, it is possible to

identify surfaces visually and get a mean value, which corresponds to field data. A software that can calculate volume based on identified joint sets such as Lispro3D could have been useful for the purpose of Slettind.

Large projects with over 1500 images require computer capacity with a 128 Gb RAM and double GPU (2x12Gb) when using the software Agisoft Photoscan. The model was later tested in other software (Realitycapture) only to compare processing times, and not to be used for structural analysis in this thesis. This software solved the processing issue connected to large imagery much better than Agisoft Photoscan.

Using drone photogrammetry for semi-automatic kinematic analysis for rockfall and rock avalanche evaluation is helpful for understanding large structures that is not visible from below or understandable in 2D photographs, and small joint sets at release areas which are not attainable. The quality is good enough for finding joint sets and orientations and offers a greater flexibility for focusing on certain areas. It still needs to be combined with field measurements for correct evaluation.

7.4 Applications and future tasks

Higher resolution images taken from lower height above ground using a terrain aware mission planning software will give a better result that will allow for improved georeferencing with ground control points. In our model the GCPs on Slettind ridge were not recognizable in the images. Preferably an RTK UAS should be used, in order to receive better georeferenced quality of the images without installing many GCPs. This can be done by multiple UAV 's with a planned mission for terrain aware lower altitude above ground to be able to cover the complete area. One UAV might be possible if more batteries are at hand to finish the flight mission.

A more detailed point cloud would improve the structure analysis in Coltop3D. By merging detailed photos of the release area (taken from a helicopter) to the 3D model and run new

analysis in Coltop3D, identification of the joint systems would improve and estimation of volume of potential unstable rock would be possible.

The identification of joint systems and analysis in Coltop3D to identify potential unstable rock and volume, will profit from an improved workflow for image acquisition. The semi-automatic kinematic analysis software Lis Pro 3D has been used in other projects and proved to be an excellent alternative to Coltop3D.

The entire road is suspect to rockfall, and the study has focused around the on south and middle part while the northern part is still an unknown. A flight mission with digital terrain aware flight path and image acquisition with a low altitude above ground (<40 m) over the northern parts of Slettind might identify which systems are prominent there. Rockfall is so frequent however, that mitigation should be prioritized. Since the weather and event reports are not liable, spending time on registering rockfall and weather situation would be very useful. A deeper understanding of the triggering factors such as snow melt events and extreme precipitation would be helping to determine timing of triggering factors and potentially might be used for an early warning system.

Rock fall modelling of jump height and run out distance is of little relevance as all large boulders and most smaller blocks reach the road.

8 Conclusion

The thesis has determined the failure mechanisms of rockfalls at Slettind, Lofoten, and analyzed the release areas with regard to potentially unstable rock. A point cloud and a 3D model have been built based on UAV photogrammetry and analyzed in a compatible software (Agisoft Photoscan) for structural analysis and furthermore a kinematic analysis was performed. The study compared UAV derived imagery that were used for a semi-automatic kinematic analysis on 3D point clouds and traditionally acquired structural data from fieldwork. Furthermore, the method using SfM was reviewed for a big rockface site that is covering 0.575 km^2 . The final 3D model had a ground resolution of 7,67 cm/pixel and a spatial precision at 7.73 cm, DEM and ortophoto was produced based on this model.

Fieldwork included the Quaternary geological interpretation of the area, structural analysis based on lithology, lineations and joint sets. The studies of Quaternary deposits and landforms indicate that rockfall is the dominant process at Slettind, with little water-related activity such as debris/earth flows. Snow avalanches are common and reach the road, but there is little snow accumulation on the slope and snow avalanches are not the major process to transport the debris to the foot of the slope. The slope eroded during the Last Glacial Maximum and with deglaciation around 16.3 ka the first rock fall activity most likely set in. The colluvial fans represent rock fall deposits of the last 16000 years.

The lithology is of high grade metamorphized gneiss and monzonites from the Archaean-Paleoproterozoic and with Precambrian ductile fabric. A new bedrock map is proposed based on the results from the 3D model and structural observations in the field. The bedrock has thereafter been subjected to major extension and strike slip deformation during the rifting and opening of the North Atlantic Ocean. Following this event the islands of Lofoten consists of normal faults, horsts and grabens, visible as the fjords and streams between islands (notable Nappstraumen), and many of the granite domes are uplifted as horsts. These events have produced the brittle lineation's found by Eigh & Bergh (2011) where S1 (NNE-SSW) and S3 (NW-SE) are lineaments present at Slettind. Further the deformation developed the joint sets which were found both in field and with the SfM derived 3Dmodel.

There are three dominant joint sets, present at the entire investigated site, with variation at the summit. one vertical N-S striking joint set, one low-angle W-E striking, one steep W-E striking and foliation dipping SW, inwards. The two first are similar to the lineations J1 and J2 which are responsible for the large opposing orthogonal structures on the slope, creating triangular shapes. The last one is slope parallel and are rockfaces where foliation is prominent, created overhangs. The kinematic analysis indicated wedge failure as the most dominant failure mechanism, and the percentage of flexural toppling is very high where foliation is daylighting. These failure mechanisms are identified in the 3D model and Coltop3D and identified surfaces in the 3D point cloud offered the possibility to estimate the unstable rock parts in the rockface.

The ridge above the release area is limited by the SE facing wall of Slettind, creating smooth and continuous lineations through heavily jointed rock, with the failure mechanism of wedge failure between J1 and J2 present. Multiple, jointed pillars are present above the release area, and the joints are in a favorable position for failure in a propagating manner.

The historical data are not precise enough regarding timing and weathering reports, such that the triggering mechanism due to meteorological influence are still uncertain. Climate in Lofoten suggests that heavy rainfall might reduce the friction angle enough for sliding to occur, in combination with freeze- thaw-events that are present through the winter due to mild and changing temperatures and little snowcover.

The UAV workflow turned out to be crucial for the identification of release areas, as the release areas are not accessible in the field without endangering the fieldwork party. Both data sets from fieldwork and the UAV workflow provide the basis for the identification of kinematic analysis and potential areas with unstable rock.

The release area of 2011/17 is estimated to still continue to produce rockfalls. Systematic joint sets are capable of large wedge failures and the risk of rock avalanches are estimated

high. Rockfall hazard is also present on the rest of the slope. Traffic at Fv 805 is not expected to increase with a large rate, and although rockfall reaching the road is a weekly event, the road is still within the tolerable level of risk at the SVV risk matrix. Rockfall or rock avalanches has such a high frequency that the habitants of Myrland is under constant threat travelling the road and will be constant vulnerable for closing of the road.

Works cited

- Advanced geo. (2015) *Photoscan crash course*. Retrieved from: <http://adv-geo-research.blogspot.com/2015/06/photoscan-crash-course-v1-1.html>
- Agisoft Photoscan. (2018). *User Manual, professional edition*. (Version 1.4). Retrieved from: http://www.agisoft.com/pdf/photoscan-pro_1_4_en.pdf
- Agliardi, F., & Crosta, G. (2003). High resolution three-dimensional numerical modelling of rockfalls. *International Journal of Rock Mechanics and Mining Sciences*, 40(4), 455-471.
- Aksoy, H., & Ercanoglu, M. (2007). Fuzzified kinematic analysis of discontinuity-controlled rock slope instabilities. *Engineering Geology*, 89(3-4), 206-219.
- Aronsen, V. (2001) *Vurdering av sikringstiltak mot steinsprang langs Fv805-01 NappX10-Myrland*. Unpublished report. (SVV: 8561886).
- Aronsen, V. (2008). *Ny vurdering av rassikring mot stein-sprang/ras av Fv 805 Myrlandsvegen mellom km 3.200-5.300 i Flakstad Kommune*. Unpublished report. (SVV, 8561888).
- Aronsen, V. (2017). *Skredfarevurdering steinsprang/ras etter steinskred 16-25.11.17 og forslag til håndtering av videre steinsprangfare*. Unpublished report. (SVV, 1694531).
- Ballantyne, C. K., Wilson, P., Gheorghiu, D., & Rodés, À. (2014). Enhanced rock-slope failure following ice-sheet deglaciation: timing and causes. *Earth Surface Processes and Landforms*, 39(7), 900-913. doi:10.1002/esp.3495
- Barton, N., & Bandis, S. (1990). *Review of predictive capabilities of JRC-JCS model in engineering practice*. Paper presented at the Rock Joints, Proc int symp on rock joints, Loen, Norway (eds N. Barton and O. Stephenson).
- Barton, N., & Grimstad, E. (2004). The Q system following thirty years of development and application in tunnelling projects. *EUROCK04, Salzburg*.
- Barton, N., Lien, R., & Lunde, J. (1974). Engineering classification of rock masses for the design of tunnel support. *Rock mechanics*, 6(4), 189-236.
- Bemis, S. P., Micklethwaite, S., Turner, D., James, M. R., Akciz, S., Thiele, S. T., & Bangash, H. A. (2014). Ground-based and UAV-based photogrammetry: A multi-scale, high-resolution mapping tool for structural geology and paleoseismology. *Journal of Structural Geology*, 69, 163-178.
- Bergh, S. G., Eig, K., Kløvjan, O. S., Henningsen, T., Olesen, O., & Hansen, J.-A. (2007). The Lofoten-Vesterålen continental margin: a multiphase Mesozoic-Palaeogene rifted shelf as shown by offshore-onshore brittle fault-fracture analysis. *Norwegian Journal of Geology/Norsk Geologisk Forening*, 87.
- Bergh, S. G., Kullerud, K., Myhre, P. I., Corfu, F., Armitage, P. E. B., Zwaan, K. B., & Ravna, E. J. K. (2014). Archaean elements of the basement outliers west of the Scandinavian Caledonides in Northern Norway: architecture, evolution and possible correlation with Fennoscandia. In *Evolution of Archean Crust and Early Life* (pp. 103-126). Springer, Dordrecht.
- Bjordal, H. (2011). *Sikring av veger mot steinskred, -Grunnlag for veiledning*. (Statens Vegvesen: nr 32). Retrieved from: <https://www.vegvesen.no/attachment/235017/binary/436828>

- Blikra, L. H., Anda, E., Høst, J., & Longva, O. (2006). Åknes/Tafjordprosjektet: Sannsynlighet og risiko knyttet til fjellskred og flodbølger fra Åknes og Hegguraksla. *Geological Survey of Norway, Trondheim, Norway, NGU report, 20*.
- Blikra, L. H., Hole, P. A., & Rye, N. (1989). *Skred i Norge: hurtige massebevegelser og avsetningstyper i alpine områder, Indre Nordfjord*. Norges geologiske undersøkelse.
- Bozzolo, D., & Pamini, R. (1986). Simulation of rock falls down a valley side. *Acta Mechanica, 63*(1-4), 113-130.
- Bredal, I. (2016). *A structural, geomorphological and InSAR study of the unstable rock slope in Oksfjellet, Kåfjord, Troms*. (Masterthesis). UiT, Tromsø.
- Brekke, H. (2000). The tectonic evolution of the Norwegian Sea continental margin, with emphasis on the Voring and More basins. *Special Publication-Geological Society of London, 167*, 327-378.
- Brendryen, J., Haflidason, H., Rise, L., Chand, S., Vanneste, M., Longva, O., . . . Forsberg, C. F. (2015). Ice sheet dynamics on the Lofoten–Vesterålen shelf, north Norway, from Late MIS-3 to Heinrich Stadial 1. *Quaternary Science Reviews, 119*, 136-156.
- Braathen, A., Blikra, L. H., Berg, S. S., & Karlsen, F. (2004). Rock-slope failures in Norway; type, geometry, deformation mechanisms and stability. *Norwegian Journal of Geology, 84*, 67-88.
- Böhme, M., Hermanns, R. L., Oppifkofer, T., Fischer, L., Bunkholt, H. S., Eiken, T., . . . Nilsen, B. (2013). Analyzing complex rock slope deformation at Stampa, western Norway, by integrating geomorphology, kinematics and numerical modeling. *Engineering Geology, 154*, 116-130. doi:<http://dx.doi.org/10.1016/j.enggeo.2012.11.016>
- Corfu, F. (2004). U–Pb age, setting and tectonic significance of the anorthosite–mangerite–charnockite–granite suite, Lofoten–Vesterålen, Norway. *Journal of Petrology, 45*(9), 1799-1819.
- Danzi, M., Di Crescenzo, G., Ramondini, M., & Santo, A. (2013). Use of unmanned aerial vehicles (UAVs) for photogrammetric surveys in rockfall instability studies. *Società Geologica Italiana, Roma*.
- Davies, M., Hamza, O., & Harris, C. (2001). The effect of rise in mean annual air temperature on the stability of rock slopes containing ice-filled discontinuities. *Permafrost and Periglacial Processes, 12*, 137-144.
- Derron, M.-H., Jaboyedoff, M., & Blikra, L. (2005). Preliminary assessment of rockslide and rockfall hazards using a DEM (Oppstadhornet, Norway). *Natural Hazards and Earth System Science, 5*(2), 285-292.
- Derron, M.-H., Jaboyedoff, M., Pedrazzini, A., Michoud, C., & Villemin, T. (2013). Remote Sensing and Monitoring Techniques for the Characterization of Rock Mass Deformation and Change Detection *Rockfall Engineering* (pp. 39-65): John Wiley & Sons, Inc.
- Devoli, G., Eikenæs, O., Taurisano, A., Hermanns, R., Fischer, L., Oppikofer, T., & Bunkholt, H. (2011). *Plan for skredfarekartlegging - Delrapport steinsprang, steinskred og fjellskred*. Retrieved from
- Dewez, T. J., Girardeau-Montaut, D., Allanic, C., & Rohmer, J. (2016). Facets: A Cloudcompare plugin to extract geological planes from unstructured 3D point clouds. *International Archives of the Photogrammetry, Remote Sensing & Spatial Information Sciences, 41*.

- Dietze, M., Turowski, J. M., Cook, K. L., & Hovius, N. (2017). Spatiotemporal patterns, triggers and anatomies of seismically detected rockfalls. *Earth Surface Dynamics*, 5(4), 757.
- Dinosaur palaeo. (2015). *Photogrammetry tutorial 11: how to handle a project in Agisoft Photoscan*. Retrieved from: <https://dinosaurpalaeo.wordpress.com/2015/10/11/photogrammetry-tutorial-11-how-to-handle-a-project-in-agisoft-photoscan/>
- Domaas, U., & Grimstad, E. (2014). Fjell-og steinskred. HØEG, K., K., K. & LIED, K.(eds.) *Skred: skredfare og sikringstiltak: praktiske erfaringer og teoretiske prinsipper*. Oslo: Universitetsforlaget.
- Dorren, L. K. (2003). A review of rockfall mechanics and modelling approaches. *Progress in Physical Geography*, 27(1), 69-87.
- Dorren, L. (2010). Rocky for 3D revealed—Description of the complete 3D rockfall model. *Association ecorisQ*.
- Drone business directory. (2014). *Harris Aerial Images Limited*. Retrieved from: <http://www.dronestagr.am/drone-business-directory/business/united-kingdom/south-west/bristol/aerial-shooting/harris-aerial-images-limited/>
- Eidsvig, U. M. K. (2014). *Sammenligning av risikoaksept-kriterier for skred og flom*. (NGI: 26/2014) Retrieved from: http://publikasjoner.nve.no/rapport/2014/rapport2014_26.pdf
- Eig, K., & Bergh, S. G. (2011). Late Cretaceous–Cenozoic fracturing in Lofoten, North Norway: Tectonic significance, fracture mechanisms and controlling factors. *Tectonophysics*, 499(1-4), 190-205.
- Eig, K., Bergh, S. G., Henningsen, T., Kløvjan, O. S., & Olesen, O. (2008). Kinematics and Relative Timing of Brittle Faults and Fractures in Lofoten, North Norway: Constraint s on the Structural Development of the Lofoten Margin. *Unpublished PhD-thesis, University of Tromsø*
- Evans, S., & Hungr, O. (1993). The assessment of rockfall hazard at the base of talus slopes. *Canadian Geotechnical Journal*, 30(4), 620-636.
- Faleide, J. I., Tsikalas, F., Breivik, A. J., Mjelde, R., Ritzmann, O., Engen, O., . . . Eldholm, O. (2008). Structure and evolution of the continental margin off Norway and the Barents Sea. *Episodes*, 31(1), 82-91.
- Ferrero, A. M., Forlani, G., Roncella, R., & Voyat, H. I. (2009). Advanced geostructural survey methods applied to rock mass characterization. *Rock Mechanics and Rock Engineering*, 42(4), 631-665.
- Frattini, P., Crosta, G., & Sosio, R. (2009). Approaches for defining thresholds and return periods for rainfall-triggered shallow landslides. *Hydrological Processes*, 23(10), 1444-1460.
- Gabrielsen, R. H., Faerseth, R. B., & Jensen, L. N. (1990). *Structural elements of the Norwegian continental shelf. Pt. 1. The Barents Sea region*. Norwegian Petroleum Directorate.
- Gabrielsen, R. H., Braathen, A., Dehls, J., & Roberts, D. (2002). Tectonic lineaments of Norway. *Norsk Geologisk Tidsskrift*, 82(3), 153-174.

- Gigli, G., Morelli, S., Fornera, S., & Casagli, N. (2014). Terrestrial laser scanner and geomechanical surveys for the rapid evaluation of rock fall susceptibility scenarios. *Landslides*, 11(1), 1-14.
- Giordan, D., Manconi, A., Tannant, D. D., & Allasia, P. (2015). *UAV: Low-cost remote sensing for high-resolution investigation of landslides*. Paper presented at the Geoscience and Remote Sensing Symposium (IGARSS), 2015 IEEE International.
- Goodman, R. E. (1989). *Introduction to rock mechanics* (Vol. 2): Wiley New York.
- Griffin, W., Taylor, P., Hakkinen, J., Heier, K., Iden, I., Krogh, E., . . . Tveten, E. (1978). Archaean and proterozoic crustal evolution in Lofoten–Vesterålen, N Norway. *Journal of the Geological Society*, 135(6), 629-647.
- Grimstad, E. (1978). *Fylkesvei Napp-Myrland Flaktstadøy, Skred og steinsprangfare*. Unpublished report. (SVV: 8561885).
- Gross, J. N., Watson, R. M., D'Urso, S., & Gu, Y. (2016). Flight-test evaluation of kinematic precise point positioning of small uavs. *International Journal of Aerospace Engineering*, 2016.
- Grumstad, A. (2017). *Geomorfologisk og strukturgeologisk undersøkelse av ustabile skråninger og skredavsetninger i fjellområdet mellom Tromsøysundet og Ullsfjorden i Troms*. (Masterthesis). UiT, Tromsø.
- Guzzetti, F., Crosta, G., Detti, R., & Agliardi, F. (2002). STONE: a computer program for the three-dimensional simulation of rock-falls. *Computers & Geosciences*, 28(9), 1079-1093.
- Hansen, J. (2009). Onshore–offshore tectonic relations on the Lofoten and Vesterålen Margin—Mesozoic to early Cenozoic structural evolution and morphological implications. *University of Tromsø, Norway, Faculty of Science, Dept. of Geology*, 229.
- Hanssen-Bauer, I., Førland, E.J., Haddeland, I., Hisdal, H., Mayer, S., Nesje, A., Nilsen, J. E. Ø., Sandven, S., Sandø, AB., Sorteberg A., and Ådlandsvik B., (2015). *Klima i Norge 2100. Bakgrunnsmateriale til NOU Klimatilpassing*. (NCCS report: 2/2015). Oslo: Miljødirektoratet.
- Hansen, J. A., & Bergh, S. G. (2012). Origin and reactivation of fracture systems adjacent to the Mid-Norwegian continental margin on Hamarøya, North Norway: use of digital geological mapping and morphotectonic lineament analysis. *Norwegian Journal of Geology/Norsk Geologisk Forening*, 92(4).
- Haukenes, Lytskjold H. (2018). *Steinsprang -Simulering, bevegelsesanalyse, struktur- og geomorfologisk undersøkelse av steinsprangområdet over Holmen ved Oksfjellet, Kåffjord, Troms*. (Masterthesis). UiT, Tromsø.
- Hellman, A. (2018). *Geohazard assessments of rock climbing sites*. (Masterthesis). University of Gothenburg, Göteborg.
- Hendriks, B. W. H., Osmundsen, P. T., & Redfield, T. F. (2010). Normal faulting and block tilting in Lofoten and Vesterålen constrained by apatite fission track data. *Tectonophysics*, 485(1-4), 154-163.
- Hermanns, R. L., Blikra, L. H., Anda, E., Saintot, A., Dahle, H., Oppikofer, T., . . . Dehls, J. F. (2013). Systematic mapping of large unstable rock slopes in Norway *Landslide science and practice* (pp. 29-34): Springer.
- Hermansson, T., Stephens, M. B., Corfu, F., Andersson, J., & Page, L. (2007). Penetrative ductile deformation and amphibolite-facies metamorphism prior to 1851 Ma in the western part of the Svecofennian orogen, Fennoscandian Shield. *Precambrian Research*, 153(1-2), 29-45.

- Hoek, E. (1994). Strength of rock and rock masses. *ISRM News Journal*, 2(2), 4-16.
- Hoek, E., & Brown, E. T. (1980). *Underground excavations in rock*: CRC Press.
- Hoek, E., & Brown, E. T. (1997). Practical estimates of rock mass strength. *International Journal of Rock Mechanics and Mining Sciences.*, 34(8), 1165-1186.
- Hoek, E., Carranza-Torres, C., & Corkum, B. (2002). Hoek-Brown failure criterion-2002 edition. *Proceedings of NARMS-Tac*, 1, 267-273.
- Hoek, E., Kaiser, P. K., & Bawden, W. F. (2000). *Support of underground excavations in hard rock*: CRC Press.
- Hoek, E., Wood, D., & Shah, S. (1992). *A modified Hoek–Brown failure criterion for jointed rock masses*. Paper presented at the Rock Characterization: ISRM Symposium, Eurock'92, Chester, UK, 14–17 September 1992.
- Hughes, A. L., Gyllencreutz, R., Lohne, Ø. S., Mangerud, J., & Svendsen, J. I. (2016). The last Eurasian ice sheets—a chronological database and time-slice reconstruction, DATED-1. *Boreas*, 45(1), 1-45.
- Hungr, O. (1988). Engineering evaluation of fragmental rockfall hazard. *Proc. of 5th Int. Sympo. on Landslide, Lausanne, 1988*, 685-690.
- Hungr, O., Leroueil, S., & Picarelli, L. (2014). The Varnes classification of landslide types, an update. *Landslides*, 11(2), 167-194. doi:10.1007/s10346-013-0436-y
- Høeg, K., Lied, K., Karlsrud, K., Gregory, T., & NORGES GEOTEKNISKE, I. (2014). Skred: skredfare og sikringstiltak: praktiske erfaringer og teoretiske prinsipper: Oslo, NGI Universitetsforl.
- Jaboyedoff, M., & Labiouse, V. (2003). *Preliminary assessment of rockfall hazard based on GIS data*. Paper presented at the 10th ISRM Congress.
- Jaboyedoff, M., Metzger, R., Oppikofer, T., Couture, R., Derron, M., Locat, J., & Turmel, D. (2007). *New insight techniques to analyze rock-slope relief using DEM and 3D-imaging cloud points: COLTOP-3D software*. Paper presented at the Rock mechanics: Meeting Society's Challenges and demands.
- Jaboyedoff, M., Oppikofer, T., Abellan, A., Derron, M.-H., Loye, A., Metzger, R., & Pedrazzini, A. (2012). Use of LIDAR in landslide investigations: a review. *Natural hazards*, 61, 5-28.
- Kvalvågnes, J. (2011). *Erfaringsnotat: Vannspyling av ur/jordmasser fra helikopter i fjellskråning etter steinskredet 19. og 25 juli 2011 ved Fv 805-01 Myrlandsfjellet i Flakstad Kommune*. Unpublished report. (SVV, Midtre Hålogaland, Notat -1)
- Koehl, J. B., Bergh, S. G., Henningsen, T., & Faleide, J. I. (2018). Middle to Late Devonian–Carboniferous collapse basins on the Finnmark Platform and in the southwesternmost Nordkapp basin, SW Barents Sea.
- Laberg, J. S., Eilertsen, R. S., & Salomonsen, G. R. (2018). Deglacial dynamics of the Vestfjorden–Trænadjupet palaeo-ice stream, northern Norway. *Boreas*, 47(1), 225-237
- Laberg, J., Eilertsen, R., & Vorren, T. (2009). The paleo–ice stream in Vestfjorden, north Norway, over the last 35 ky: Glacial erosion and sediment yield. *Geological Society of America Bulletin*, 121(3-4), 434-447.
- Lambert, S., & Nicot, F. (2013). *Rockfall engineering*: John Wiley & Sons.
- Lee, S., Suh, J., & Choi, Y. (2018). Review of smartphone applications for geoscience: current status, limitations, and future perspectives. *Earth Science Informatics*, 1-24.
- Lied, K. (1984). Skredfarevurdering. Unpublished report. (NGI, 83903-02)

- Manousakis, J., Zekkos, D., Saroglou, F., & Clark, M. (2016). Comparison of UAV-enabled photogrammetry-based 3D point clouds and interpolated DSMs of sloping terrain for rockfall hazard analysis. *The International Archives of Photogrammetry, Remote Sensing and Spatial Information Sciences*, 42, 71.
- Marinos, V. I. I., Marinos, P., & Hoek, E. (2005). The geological strength index: applications and limitations. *Bulletin of Engineering Geology and the Environment*, 64(1), 55-65.
- Matasci, B., Stock, G., Jaboyedoff, M., Carrea, D., Collins, B., Guérin, A., . . . Ravelin, L. (2017). Assessing rockfall susceptibility in steep and overhanging slopes using three-dimensional analysis of failure mechanisms. *Landslides*, 1-20.
- Metzger, R., Jaboyedoff, M., Oppikofer, T., Viero, A., & Galgano, A. (2009). *Coltop3D: A new software for structural analysis with high resolution 3D point clouds and DEM*. Paper presented at the Frontiers + Innovation, Calgary, Alberta, Canada.
- Meteorologisk institutt. (2018). *Været som var, Leknes*. Retrieved 05.08.18 from: <https://www.yr.no/sted/Norge/Nordland/Vestvågøy/Leknes/statistikk.html>
- Müller, J., Gärtner-Roer, I., Thee, P., & Ginzler, C. (2014). Accuracy assessment of airborne photogrammetrically derived high-resolution digital elevation models in a high mountain environment. *ISPRS Journal of Photogrammetry and Remote Sensing*, 98, 58-69.
- Nilsen, B., & Ozdemir, L. (1999). *Recent developments in site investigation and testing for hard rock TBM projects*. Paper presented at the PROCEEDINGS OF THE RAPID EXCAVATION AND TUNNELING CONFERENCE.
- Norges geologiske institutt. (2015). *Engineering geology and rock mechanics – Q-system*. Retrieved from: <https://www.ngi.no/eng/Services/Technical-expertise-A-Z/Engineering-geology-and-rock-mechanics/Q-system>
- Norsk Klimaservicesenter. (2018). Klimaframskrivinger Nordland. Retrieved 01.12.18 from: <https://klimaservicesenter.no/faces/desktop/scenarios.xhtml>
- Norges vassdrag og energi direktorat. (2018). *NVE Skredhendelser*. Retrieved 11.07.18 from: <https://gis3.nve.no/link/?link=SkredHendelser>
- Oppikofer, T., Jaboyedoff, M., Blikra, L., Derron, M.-H., & Metzger, R. (2009). Characterization and monitoring of the Åknes rockslide using terrestrial laser scanning. *Natural Hazards and Earth System Sciences*, 9(3), 1003-1019.
- Osmundsen, P. T., Sommaruga, A., Skilbrei, J. R., & Olesen, O. (2002). Deep structure of the Mid Norway rifted margin. *Norwegian Journal of Geology/Norsk Geologisk Forening*, 82(4).
- Palmstrom, A., & Broch, E. (2006). Use and misuse of rock mass classification systems with particular reference to the Q-system. *Tunnelling and underground space technology*, 21(6), 575-593.
- Pavlis, T. L., & Mason, K. A. (2017). The New World of 3D Geologic Mapping. *GSA Today*, 27(9).
- Persson, A. (2011). *Fv 805-01 km 3,500 ved Myrland i Flakstad Kommune Rasfarevurdering i løpsneområde og underliggende utløpsområde etter steinras i juli 2011*. Unpublished report. (SVV, 16970292).
- Schanche, S. (2014). Sikkerhet mot skred i bratt terreng. *NVEs veileder*, 8, 2014
- Schermer, E. R., Redfield, T. F., Indrevær, K., & Bergh, S. G. (2017). Geomorphology and topography of relict surfaces: the influence of inherited crustal structure in the northern Scandinavian Mountains. *Journal of the Geological Society*, 174(1), 93-109.

- Skrede, I. (2013). *Jettan, Nordnesfjellet, Kåfjord, Troms – indre geometri og struktur, kinematikk og styrende faktorer av eit ustabilt fjellparti, basert på strukturellanalyse, geomorfologi og overvakingsdata*. (Masterthesis). UiT, Tromsø.
- Statens Vegvesen Region Nord. (2015). *Skredsikringsbehov for riks- og fylkesveg: Nordland-Troms- Finmark*. Bodø: Statens vegvesen
- Statens Vegvesen. (2018). *Vegkart*. Retrieved from 20.07.18:
[https://www.vegvesen.no/vegkart/vegkart/#kartlag:geodata/hva:\(~\(id:540,filter:\(~\),farge:'0 0'\)\)/@434246,7559729,11/vegobjekt:88710882:58b02c:540](https://www.vegvesen.no/vegkart/vegkart/#kartlag:geodata/hva:(~(id:540,filter:(~),farge:'0 0'))/@434246,7559729,11/vegobjekt:88710882:58b02c:540)
- Stead, D., & Wolter, A. (2015). A critical review of rock slope failure mechanisms: the importance of structural geology. *Journal of Structural Geology*, 74, 1-23.
- Store norske leksikon. (2009). *Nordland -klima*. Retrieved from: <https://snl.no/Nordland - klima>
- Rocscience. (2018). *Dips 7.0 Graphical & Statistical Analysis of orientation data*. Retrieved from:
https://www.rocscience.com/help/dips/pdf_files/tutorials/Tutorial_04_Toppling_Planar_and_Wedge_Sliding.pdf
- Trafikverket. (2015). *Projektering av bergkonstruksjoner 2014:144*. Sundbyberg. Retrieved from https://trafikverket.ineko.se/Files/sv-SE/11641/Ineko.Product.RelatedFiles/2014_144_Projektering_av_bergkonstruksjoner_handbok.pdf
- Trulssen, M. (2008). *Sammenhengen mellom landskap og tektonikk på Flakstadøya og Moskenesøya i Lofoten*. (Masterthesis). UiT, Tromsø.
- Tveten, E. (1978). *Geologisk kart over Norge, berggrunnskart Svolvær 1:250 000* (NGU). Retrieved from:<https://kartkatalog.geonorge.no/metadata/norges-geologiske-undersokelse/berggrunnwms/3a3eda68-f6ae-4a44-a934-c91a1e8fb562?text=&Facets%5B0%5D.name=organization&Facets%5B0%5D.value=Geological%20Survey%20of%20Norway>
- Varnes, D. J. (1978). Slope movement types and processes. *Special report*, 176, 11-33.
- Volkwein, A., Schellenberg, K., Labiouse, V., Agliardi, F., Berger, F., Bourrier, F., . . . Jaboyedoff, M. (2011). Rockfall characterisation and structural protection-a review. *Natural Hazards and Earth System Sciences*, 11, p. 2617-p. 2651.
- Vorren, T. O., Rydningen, T. A., Baeten, N. J., & Laberg, J. S. (2015). Chronology and extent of the Lofoten–Vesterålen sector of the Scandinavian Ice Sheet from 26 to 16 cal. ka BP. *Boreas*, 44(3), 445-458.
- Westoby, M., Brasington, J., Glasser, N., Hambrey, M., & Reynolds, J. (2012). 'Structure-from-Motion' photogrammetry: A low-cost, effective tool for geoscience applications. *Geomorphology*, 179, 300-314.
- Wyllie, D. C. (2014). *Rock fall engineering*: CRC Press.
- Wyllie, D. C., & Mah, C. (2004). *Rock slope engineering* 4th Edition: London, Spon Press.
- Xgeo. (2018). *Snødybde og temperatur, -Skjelfjord*. Retrieved 01.12.18 from:
<http://www.xgeo.no>

Appendix 1: Weather graphs

Following data shows precipitation for Leknes Airport and Leknes citye (Meteorologisk Institutt, 2018) for the last six years. The precipitation is given as maximum mm/24 hrs, from 07-07. Temperature is middle temperature registered for the month. The graph from xgeo.net shows snowdepth at sealevel in cm.

Elementer		
Kode	Navn	Enhet
RR	Nedbør	mm
TAM	Middeltemperatur	°C

*** MELDING ***

Dataverdi merket **x** betyr manglende tilgang eller at kvaliteten er 'Svært usikker, mod

85560 LEKNES LUFTHAVN												
Maksimale TAM verdier												
År	jan	feb	mar	apr	mai	jun	jul	aug	sep	okt	nov	des
2012	4,8	5,4	5,5	6,2	9,0	13,4	16,2	15,4	12,7	x	6,8	2,7
2013	4,6	5,6	0,9	5,9	19,0	21,5	18,3	19,0	16,5	11,4	5,7	6,8
2014	5,7	5,5	5,9	5,9	11,2	20,1	23,5	17,7	13,3	15,9	7,5	6,9
2015	6,1	5,2	6,1	6,0	11,8	11,1	14,5	19,5	14,9	9,7	8,3	6,5
2016	5,8	3,3	7,8	10,5	14,0	19,1	19,9	16,9	13,3	x	6,8	7,6
2017	6,3	6,5	4,3	6,0	9,4	19,4	18,0	15,7	15,3	12,5	7,5	6,0
Maks	6,3	6,5	7,8	10,5	19,0	21,5	23,5	19,5	16,5	15,9	8,3	7,6
År	2017	2017	2016	2016	2013	2013	2014	2015	2013	2014	2015	2016

85560 LEKNES LUFTHAVN												
Maksimale RR verdier												
År	jan	feb	mar	apr	mai	jun	jul	aug	sep	okt	nov	des
2016												25,7
2017	23,8	18,2	13,0	36,4	10,0	7,8	8,7	26,5	4,2	27,9	23,3	21,9
Maks	23,8	18,2	13,0	36,4	10,0	7,8	8,7	26,5	4,2	27,9	23,3	25,7
År	2017	2017	2017	2017	2017	2017	2017	2017	2017	2017	2017	2016

85540 LEKNES I LOFOTEN												
Maksimale RR verdier												
År	jan	feb	mar	apr	mai	jun	jul	aug	sep	okt	nov	des
2012	16,8	32,0	24,5	12,2	24,5	10,2	19,5	12,3	28,0	16,5	18,7	10,8
2013	18,6	18,3	13,6	11,6	10,2	18,7	13,0	12,4	13,5	22,2	44,0	34,0
2014	3,7	30,1	32,5	36,0	11,5	18,7	14,0	14,0	50,0	19,4	17,5	17,0
2015	31,1	14,5	19,5	17,0	10,3	18,2	20,5	7,4	18,4	23,2	30,5	21,5
2016	11,0	22,8	41,0	15,0	6,5	13,3	29,2	6,3	30,0	28,2	26,5	34,0
2017	32,0	14,1	19,1	34,5	16,0	9,2	8,4	32,0	2,5	28,5	23,0	20,1
Maks	32,0	32,0	41,0	36,0	24,5	18,7	29,2	32,0	50,0	28,5	44,0	34,0
År	2017	2012	2016	2014	2012	2014	2016	2017	2014	2017	2013	2016

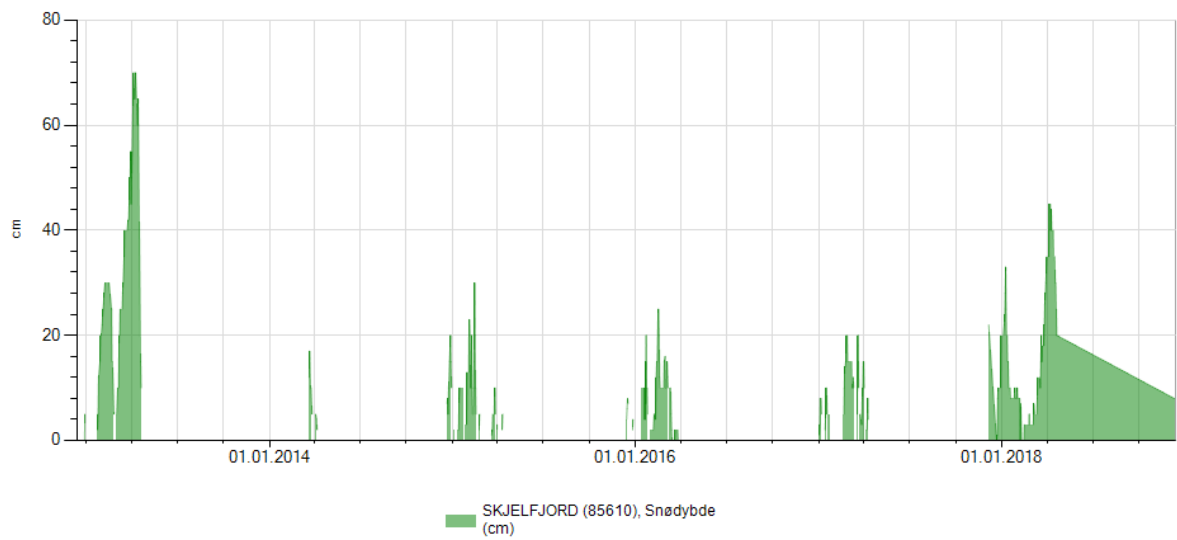


Fig. 67 Snowdepth in Skjelsjord last 6 years

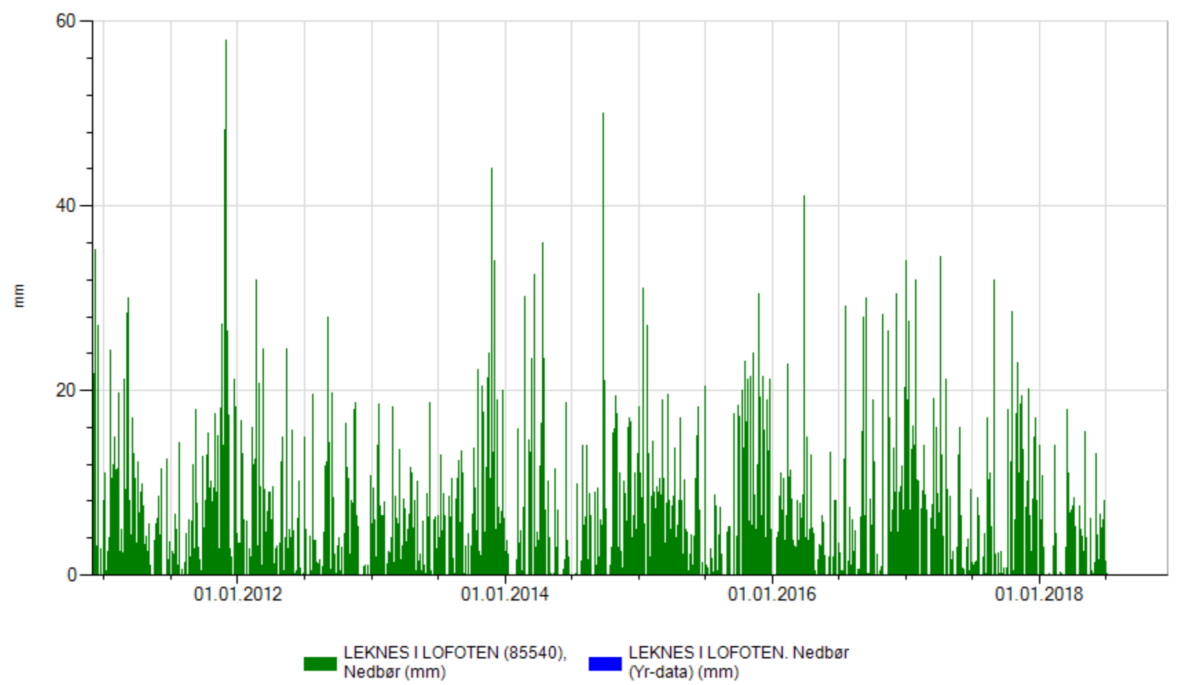
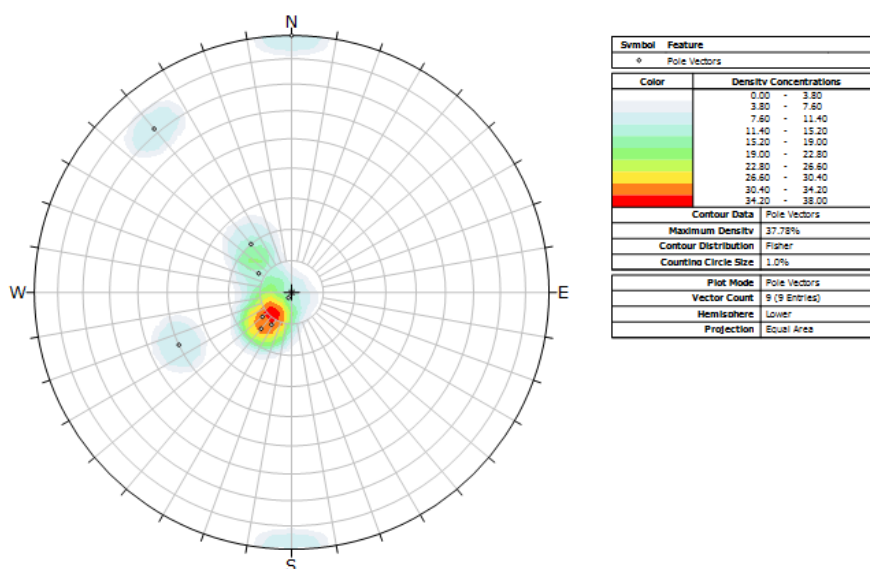


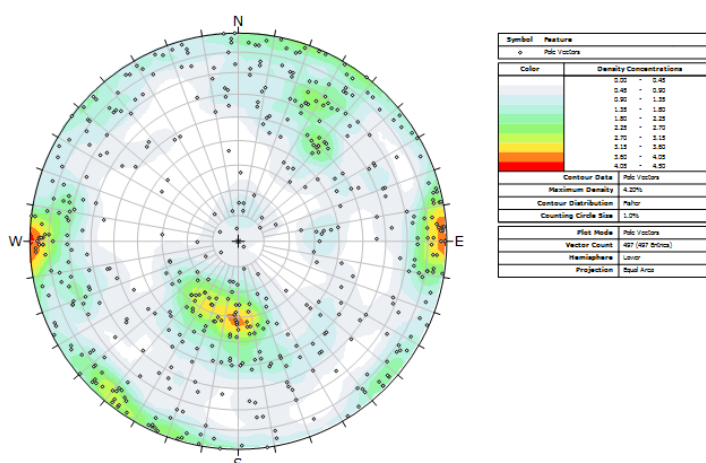
Fig. 68 Precipitation in mm last 7 years

Appendix 2: Structural measurements with different methods

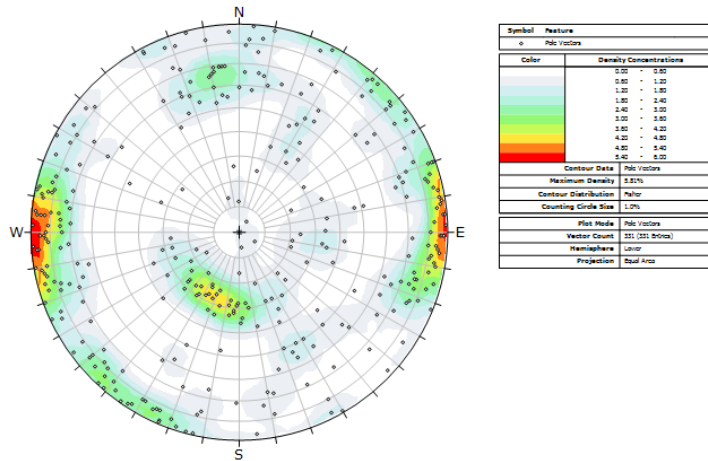
The different methods used, handhold compass, Fieldmove Clino and GeoID is here presented in separate stereographic projections, all measurements combined.



Structural orientation data from handheld compass used to calibrate the apps GeoID and Clino Fieldmove. Measurements done at location 1 and 1.2 (Figure).



Stereoplot of in total 497 structural orientation data made with Geo ID in the field locations (location 1, 2, north and 4). The steep north-south striking planes is dominating along with the low angle north facing plane. This stereoplot has quite a bit of scatter of poles.



Stereonet showing results from all locations at Myrland done with Clino Fieldmove, in total 331 measurements. Measurements made with this app shows less scatter, and the steep N-S striking plane along with the low angle north facing is well defined here as well. The poles in the north are more towards west compared to GeoID but this may be due to different amount of measurements at the locations.

Appendix 3: Agisoft report

Survey Data

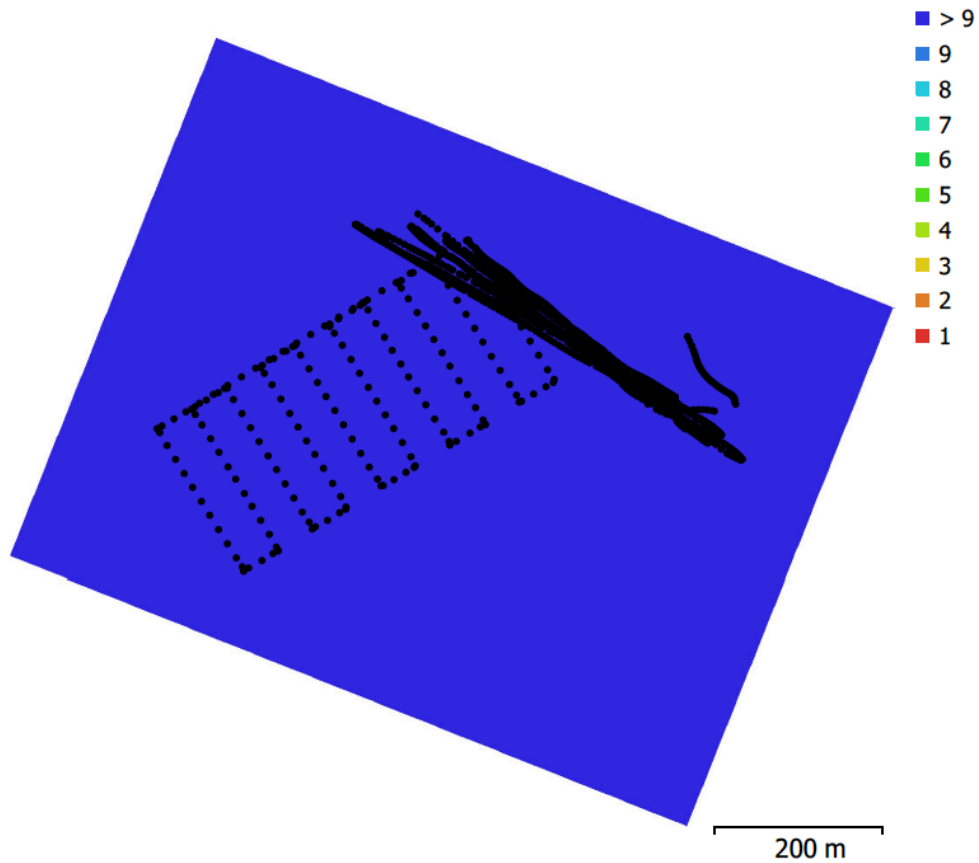


Fig. 1. Camera locations and image overlap.

Number of images:	1,206	Camera stations:	1,206
Flying altitude:	184 m	Tie points:	2,708,276
Ground resolution:	7.67 cm/pix	Projections:	22,059,977
Coverage area:	0.575 km ²	Reprojection error:	0.461 pix

Ground Control Points

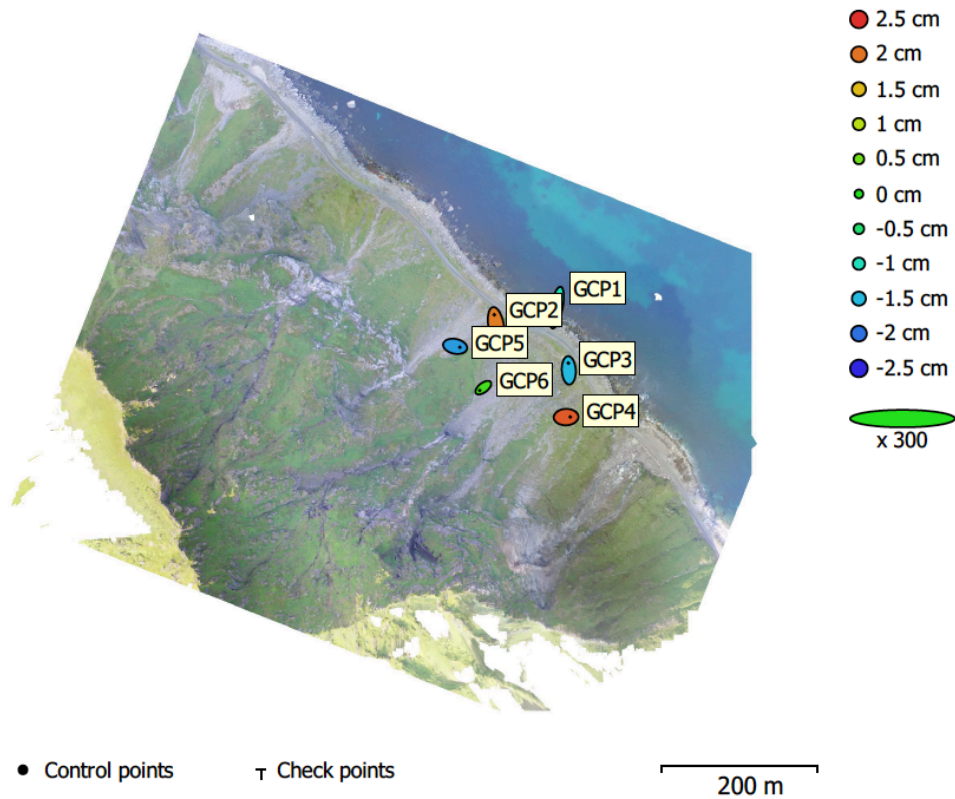


Fig. 12. GCP locations and error estimates.

Z error is represented by ellipse color. X,Y errors are represented by ellipse shape.
 Estimated GCP locations are marked with a dot or crossing.

Label	X error (cm)	Y error (cm)	Z error (cm)	Total (cm)	Image (pix)
GCP1	-2.50037	-12.6755	-0.963293	12.9556	0.968 (197)
GCP2	-1.61353	9.55863	1.95345	9.88872	0.987 (191)
GCP3	-0.32874	6.17745	-1.49183	6.36353	0.897 (199)
GCP4	3.54711	0.120078	2.19141	4.17117	1.514 (262)
GCP5	4.00464	-0.819502	-1.74017	4.44263	0.913 (268)
GCP6	-3.10649	-2.38776	0.198808	3.92316	1.399 (457)
Total	2.80573	7.03069	1.57265	7.73149	1.195

Table 13. Control points.

X - Longitude, Y - Latitude, Z - Altitude.

Digital Elevation Model

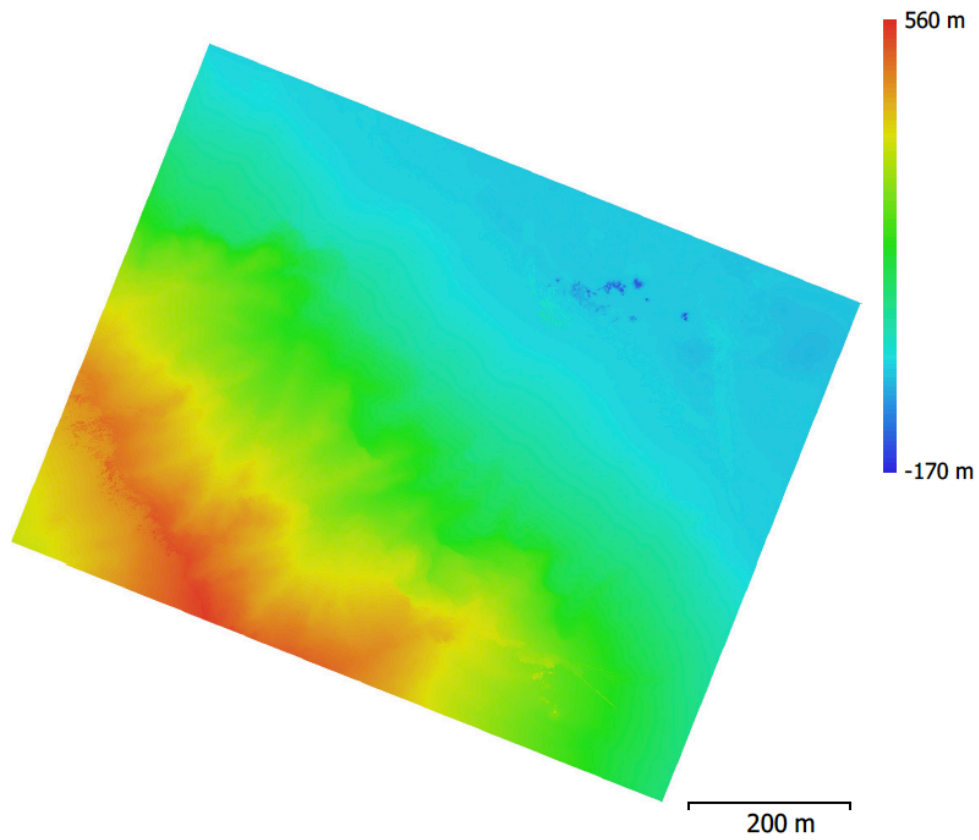


Fig. 13. Reconstructed digital elevation model.

Resolution: 15.3 cm/pix
Point density: 42.5 points/m²

General	
Cameras	1206
Aligned cameras	1206
Markers	6
Coordinate system	WGS 84 (EPSG::4326)
Rotation angles	Yaw, Pitch, Roll
Point Cloud	
Points	2,708,276 of 3,650,119
RMS reprojection error	0.154086 (0.460649 pix)
Max reprojection error	4.32935 (10.5364 pix)
Mean key point size	2.88192 pix
Point colors	3 bands, uint8
Key points	No
Average tie point multiplicity	12.9056
Dense Point Cloud	
Points	82,240,096
Point colors	3 bands, uint8
Reconstruction parameters	
Quality	High
Depth filtering	Aggressive
Model	
Faces	71,558,023
Vertices	35,795,954
Vertex colors	3 bands, uint8
Texture	10,000 x 10,000, 4 bands, uint8
Reconstruction parameters	
Surface type	Arbitrary
Source data	Dense
Interpolation	Enabled
Quality	High
Depth filtering	Aggressive
Face count	0
Processing time	46 minutes 23 seconds
Texturing parameters	
Mapping mode	Generic
Blending mode	Mosaic
Texture size	10,000 x 10,000
Enable hole filling	Yes
Enable ghosting filter	Yes
UV mapping time	24 minutes 10 seconds
Blending time	14 hours 43 minutes
DEM	
Size	6,857 x 6,114
Coordinate system	WGS 84 (EPSG::4326)
Reconstruction parameters	
Source data	Dense cloud
Interpolation	Enabled
Processing time	53 seconds
Orthomosaic	
Size	13,714 x 12,229
Coordinate system	WGS 84 (EPSG::4326)
Colors	3 bands, uint8
Reconstruction parameters	
Blending mode	Mosaic
Surface	Mesh